FACULTY OF
NUCLEAR SCIENCES
AND PHYSICAL
ENGINEERING
CTU IN PRAGUE

HABILITATION THESIS

# SIMULATION STUDIES OF LASER-DRIVEN ION ACCELERATION BY ULTRASHORT LASER PULSES

Prague, 2018

JAN PŠIKAL

## Bibliographic Entry

| | |
|---|---|
| Author | Ing. Jan Pšikal, Ph.D.<br>Faculty of Nuclear Sciences and Physical Engineering<br>Czech Technical University in Prague<br>Department of Physical Electronics |
| Title of Thesis | SIMULATION STUDIES OF LASER-DRIVEN ION ACCELERATION BY ULTRASHORT LASER PULSES |
| Field of Habilitation | Applied Physics |
| Year | 2018 |
| Number of Pages | 132 |
| Keywords | ion acceleration; laser pulse; numerical simulation; plasma physics |

# Bibliografický záznam

| | |
|---|---|
| Autor | Ing. Jan Pšikal, Ph.D.<br>Fakulta jaderná a fyzikálně inženýrská<br>České vysoké učení technické v Praze<br>Katedra fyzikální elektroniky |
| Název práce | Simulace laserově řízeného urychlování iontů pomocí ultrakrátkých laserových impulzů |
| Obor habilitace | Aplikovaná fyzika |
| Rok vydání | 2018 |
| Počet stran | 132 |
| Klíčová slova | urychlování iontů; laserový impulz; numerická simulace; fyzika plazmatu |

## Abstract

Particle-in-cell simulations are an efficient tool in the research of laser-plasma interactions. They enable to study physical phenomena with a high temporal and spatial resolution and, thus, help with the interpretation of experimental results and/or with theoretical predictions. This habilitation thesis summarizes the contribution of the author in the field of ion acceleration by ultrashort laser pulses mostly based on the simulations. After a brief description of the simulation method and various ion acceleration mechanisms, it focuses on authors' main results in this field in the form of his commented articles published in impacted journals. Finally, research topics possibly investigated in the future and related to previous author's work are briefly discussed.

## Abstrakt

Částicové simulace jsou efektivním nástrojem ve výzkumu fyziky laserového plazmatu. Umožňují detailní studium fyzikálních jevů s vysokým časovým i prostorovým rozlišením a tím pomáhají s interpretací výsledků experimentu i s teoretickými předpověďmi. Tato habilitační práce shrnuje autorovy výsledky v oblasti urychlování iontů velmi krátkými laserovými svazky založenými převážně na simulacích. Po stručném popisu použité simulační metody a různých mechanismech urychlování iontů se soustředí zejména na autorovy výsledky publikované v článcích v impaktovaných časopisech, zde dále okomentované. Závěrem jsou stručně diskutována související nedořešená témata, kterými by se autor mohl v budoucnu zabývat.

# Contents

**1 Introduction** **1**

**2 Particle-in-cell (PIC) simulations** **3**
- 2.1 Basics of the PIC simulation technique . . . . . . . . . . . . 5
  - 2.1.1 Field solver . . . . . . . . . . . . . . . . . . . . . . . . 6
  - 2.1.2 Particle pusher . . . . . . . . . . . . . . . . . . . . . . 6
  - 2.1.3 Shape functions representing macroparticles . . . . . . 7
- 2.2 Numerical stability and accuracy, boundary conditions . . . 8
  - 2.2.1 Setting of numerical parameters . . . . . . . . . . . . 9
  - 2.2.2 Choice of appropriate boundary conditions . . . . . . 10
- 2.3 PIC simulations on large computer clusters . . . . . . . . . 11

**3 Laser-driven ion acceleration mechanisms** **13**
- 3.1 Target Normal Sheath Acceleration . . . . . . . . . . . . . . 14
- 3.2 Radiation Pressure Acceleration . . . . . . . . . . . . . . . . 16
  - 3.2.1 Hole Boring regime . . . . . . . . . . . . . . . . . . . . 17
  - 3.2.2 Light Sale regime . . . . . . . . . . . . . . . . . . . . . 18
- 3.3 Breakout Afterburner . . . . . . . . . . . . . . . . . . . . . . 19
- 3.4 Magnetic Vortex Acceleration . . . . . . . . . . . . . . . . . 20
- 3.5 Coulomb Explosion . . . . . . . . . . . . . . . . . . . . . . . 21

**4 Comments on selected publications** **23**
- 4.1 Paper 1: Dominance of hole-boring radiation pressure acceleration regime with thin ribbon of ionized solid hydrogen . . 23

4.2 Paper 2: Hollow target for efficient generation of fast ions by ultrashort laser pulses . . . . . . . . . . . . . . . . . . . . . 25
4.3 Paper 3: Increased efficiency of ion acceleration by using femtosecond laser pulses at higher harmonic frequency . . . 27
4.4 Paper 4: Simulations of femtosecond laser pulse interaction with spray target . . . . . . . . . . . . . . . . . . . . . . . . . 28
4.5 Paper 5: Laser-induced ion acceleration at ultra-high laser intensities . . . . . . . . . . . . . . . . . . . . . . . . . . . . 30
4.6 Paper 6: Manipulation of laser-accelerated proton beam profiles by nanostructured and microstructured targets . . . . . 31
4.7 Paper 7: Laser-driven high-energy proton beam with homogeneous spatial profile from a nanosphere target . . . . . . . 32
4.8 Paper 8: Proton acceleration driven by a nanosecond laser from a cryogenic thin solid-hydrogen ribbon . . . . . . . . . 34
4.9 Main contributions of the listed publications . . . . . . . . . 35

**5 Conclusions** **37**
5.1 Future Work . . . . . . . . . . . . . . . . . . . . . . . . . 38
5.2 Collaboration with students . . . . . . . . . . . . . . . . . . 39

**Bibliography** **41**

**A Paper 1** **53**

**B Paper 2** **55**

**C Paper 3** **63**

**D Paper 4** **71**

**E Paper 5** **73**

**F Paper 6** **75**

**G Paper 7** **85**

**H Paper 8** **93**

## Chapter 1

# Introduction

Laser-driven particle acceleration has been intensively studied in the last two decades when generated laser pulses achieved intensities which accelerate electrons to kinetic energies higher than their rest energy . Such intense very short laser pulses can irradiate matter which is immediately ionized at intensities of several orders of magnitude lower than their peak intensity [1]. Thus, ionized matter called plasma interacts with the main (most intense) part of the pulse. Electrostatic fields created in the plasma under the action of laser field can reach 10000 times higher peak values compared with the fields generated by conventional particle accelerators [2]. That means that particles can be accelerated to the same energy on a distance about $0.1\ \mathrm{mm}$ in plasma instead of $1\ \mathrm{m}$ using the standard acceleration technology.

Unfortunately, the acceleration of charged particles in plasma is not so straightforward and a lot of effort has been made to demonstrate and optimize this laser-driven particle acceleration [3, 4]. Since the interaction of laser pulses with plasma takes very short time given by the duration of the pulse, it is indispensable to study this interaction by numerical simulations showing the evolution of plasma and acceleration of charged particles with very high temporal resolution. It was shown experimentally and numerically that underdense plasma (created in gas jets or in capillaries) where laser beam propagates is favorable for the acceleration of electrons to energies up to several GeVs [5]. On the other hand, overdense plasma (created by ionized solid or liquid targets), where the laser beam can be reflected and partially absorbed, is mostly suitable for the acceleration of ions to energies about up to 100 MeV per nucleon in nowadays experiments [6].

This thesis shows the contribution of the author to the research of laser-driven ion acceleration. The author has dealt with numerical simulations and theoretical studies of various ion acceleration mechanisms as well as the interpretation and/or the prediction of various experiments. The thesis is arranged as a commented collection of authors' publications both theoretical and experimental ones with substantial contribution of the author.

Chapter 2 describes numerical method used for our studies and difficulties which has to be solved in order to successfully applied numerical codes based on this method. In Chapter 3 mechanisms of laser-driven ion acceleration are described and their relevance in real experiments is assessed. Chapter 4 contains comments on selected publications of the author relevant to ion acceleration by the interaction of ionized overdense targets with ultrashort very intense laser pulses. Each of these papers is included as a separate appendix at the end of the thesis, its content is reviewed, and the contributions of the author are summarized. The thesis is concluded in Chapter 5.

Chapter **2**

# Particle-in-cell (PIC) simulations

There are three basic approaches for numerical calculations of plasma evolution [7]: particle approach, kinetic theory, and hydrodynamics.

- **Particle description** is based on the equations of motion of individual particles in electromagnetic fields. The plasma is described by electrons and ions moving under the influence of the electric and magnetic fields due to their own charge and of the laser fields. For practical reasons, computer simulation of plasma using particle codes is limited to $N \approx 10^{10}$ particles in the most demanding calculations, whereas the number of particles in typical laboratory laser-plasma system is much higher ($\sim 10^{15}$ particles). Therefore, each particle has to represent a large number of real electrons or ions in this type of simulation. However, the decreasing number of particles means increasing noise, which indicates that this approach has limitations and some specific phenomena have to be studied by kinetic approach.

- **Kinetic description** is based on a set of equations for (macroscopic) distribution function $f_s(\vec{x}, \vec{p})$ of each plasma particle species $s$ together with Maxwell equations. The distribution function is a statistical description of a very large number of interacting particles. Each particle has its own position in the phase space $(\vec{x}, \vec{p})$, where $\vec{x}$ are the coordinates for all the degrees of freedom and $\vec{p}$ are the corresponding momentum components. In this approach, $f_s(\vec{x}, \vec{p})\mathrm{d}^3\vec{x}\mathrm{d}^3\vec{p}$ is equal to the number of particles of species $s$ in the domain $[(\vec{x}, \vec{x} + \mathrm{d}\vec{x}), (\vec{p}, \vec{p} + \mathrm{d}\vec{p})]$.

Vlasov equation describing the evolution of the distribution function $f_s(\vec{x}, \vec{p}, t)$ for each species of particles is given as follows:

$$\frac{\partial f_s}{\partial t} + \frac{\vec{p}}{m_s \gamma} \frac{\partial f_s}{\partial \vec{x}} + q_s \left( \vec{E} + \left( \frac{\vec{p}}{m_s \gamma} \right) \times \vec{B} \right) \frac{\partial f_s}{\partial \vec{p}} = 0, \qquad (2.1)$$

where $m_s$ is the rest mass of particle species $s$, $q_s$ its charge, $\vec{E}$ and $\vec{B}$ electric and magnetic fields in the position $\vec{x}$ and time $t$. The statistical content of the Vlasov equation is expressed by assuming that $f_s$ is a smooth function (i.e., differentiable) describing an average quantity over a phase space volume $\mathrm{d}^3\vec{x}\mathrm{d}^3\vec{p}$ containing a large number of particles. The electromagnetic fields, $\vec{E}$ and $\vec{B}$ are also smooth averaged quantities. The force acting on any plasma particle, describing the effect of all the other particles, is assumed to be a continuous and slowly varying function of space. This is a good approximation only if the collective effect is larger than direct collisions with nearby particles; therefore, the Vlasov equation is considered to be collisionless. If the short-range collisions are important, the collision term is added on the right hand side of Eq. (2.1).

- **Hydrodynamic description** uses conservation laws of mass, momentum, and energy which are coupled to Maxwell equations. In addition, for a fluid model, a local thermodynamic equilibrium (LTE) is assumed and the knowledge of the equations of state (relations between pressure, temperature, energy, entropy, etc.) is mandatory for solving the problem. The fluid theory is a good approximation for many phenomena in the interaction of plasma with relatively low laser intensities ($\approx 10^{15}$ $\mathrm{W/cm^2}$) and relatively long laser pulses (ns). However, the model is not always adequate, because there is an assumption of LTE. All the variables in the fluid equations are functions of time and position, and each species in an LTE plasma has a Maxwellian distribution of the velocities everywhere. Physical quantities such as temperature and pressure can be defined only in LTE. Systems that are not in LTE (such as plasma interacting with relativistically intense femtosecond laser pulse) cannot be described by fluid equations. Hydrodynamic model can describe a target globally including nonionized solid part of the target.

For the study of ultrashort laser pulse interaction with ionized targets, particle approach is mostly used, namely particle-in-cell (PIC) simulation method. This method can study the interaction of ionized matter with very high intensity pulses in the so-called relativistic regime when the kinetic energy of electrons oscillating in the laser field exceeds its rest energy (at intensities $I > 10^{18}\ \mathrm{W/cm^2}$). In this case, the electrons with high relativistic velocities do not heat the plasma by collisional effects since the collisional frequency of those electrons with background plasma is indirectly proportional to the velocity of electrons cubed [1, 8]. Thus, the plasma is out of LTE and only kinetic or particle description of plasma can be applied in the calculations of the interaction and subsequent plasma evolution.

The potential advantage of kinetic Vlasov codes is a possibility of producing smooth results as the Vlasov codes handle the distribution function which is a smoothly changing real number already giving a probability of finding the plasma particles at the corresponding point of the phase space. Therefore, this approach is useful in the studies of some specific phenomena, for example stimulated Raman (back-)scattering [9, 10]. On the other hand, Vlasov codes are very expensive from the computational point of view. The kinetic Vlasov equation (2.1) on the single-particle distribution function has to be generally solved in the six-dimensional phase space and even one-dimensional problem may demand the use of parallel supercomputers [11]. Even though PIC codes are also relatively demanding on computational resources, Eulerian grid in the configuration space has half of the dimensions (i.e., spatial coordinates) compared with Vlasov codes (i.e., spatial plus corresponding momentum coordinates). Therefore PIC codes are usually the best option for the calculations.

## 2.1 Basics of the PIC simulation technique

The core algorithm of PIC code consists of two coupled solvers: one that moves charged particles freely in space under the influence of electromagnetic fields and calculates the currents due to the particle motions (the particle pusher) and another that solves Maxwell equations on a fixed spatial grid subject to the currents calculated from the particle motions (the field solver) [12].

In fact, the PIC method replaces the distribution function $f_s$ used in (2.1) with macroparticles [11]. Each macroparticle represents a large number of real particles, with the number of real particles represented by each simulation particle (i.e., by each macroparticle) called the weight. When simulations contain changes in density there is the option to either represent this by changing the weight of each macroparticle to reproduce the density structure or by keeping the weight of the macroparticles constant and changing the number density of macroparticles to match the real density.

The relationship between the distribution function and the macroparticles can be described using the following relation:

$$f_s(\vec{x}, \vec{p}, t) = \sum_{k=1}^{N} N_k S_x(\vec{x} - \vec{x_k}) S_p(\vec{p} - \vec{p_k})). \tag{2.2}$$

Each macroparticle represents $N_k$ real particles (which is numerical weight of macroparticle) and has its own position $\vec{x_k}$ and momentum $\vec{p_k}$. The functions $S_x$ and $S_p$ represent how a macroparticle "looks" in the position and momentum phase space, respectively, and are usually referred to as shape functions. Choice of the shape functions has an important impact on the numerical properties of the algorithm [12].

### 2.1.1 Field solver

The finite-difference time-domain method (FDTD) is implemented in most PIC codes as a standard technique for solving Maxwell equations numerically. Electric $\vec{E}$ and magnetic $\vec{B}$ field are calculated on a Yee staggered grid. An example of this staggered grid is shown in Fig. 1. Here, the electric fields are calculated in the middle of the faces of a cubical cell while magnetic fields are calculated in the middle of the edges of the cube. This special distribution of gridpoints allows to use central differences which in turn leads to the second order accuracy. Moreover, in most PIC codes, modified or standard leapfrog method is used which means that $\vec{E}$ and $\vec{B}$ are fully or partially updated at both the full time step and the half time step.

### 2.1.2 Particle pusher

The particle pusher solves the relativistic equation of motion under the Lorentz force for each macroparticle in the simulation. Various numerical schemes for

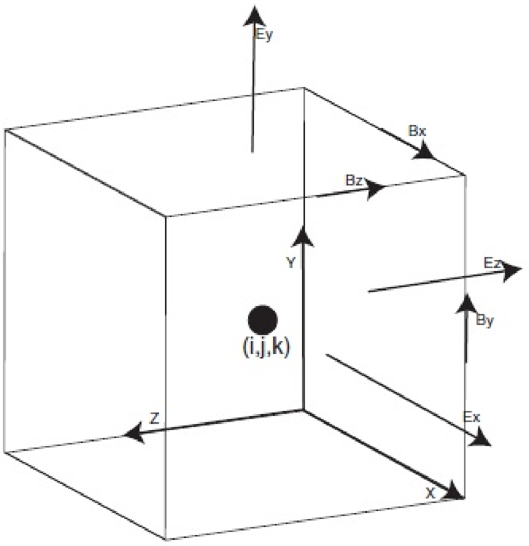

Figure 1: Yee staggered grid in 3D PIC code EPOCH [12]. Electric field components ($E_x$, $E_y$, $E_z$) are calculated in the middle of the faces of a cubical cell while magnetic field components ($B_x$, $B_y$, $B_z$) are calculated in the middle of the edges of the cube.

the calculation of the motion of particles are used. The standard leapfrog method is often used where particle momentum components are calculated one half-step after the calculation of particle positions. Most PIC codes use the Boris rotation algorithm [13] which splits the equation of motion into separate parts responsible for the acceleration of the particle in the $\vec{E}$ field and the rotation of the particle in the $\vec{B}$ field.

Based on the motion of particles (updated velocities and positions of macroparticles) the currents needed for the Maxwell solver can be calculated using several methods [14, 15, 16]. These charge conserving methods ensure that divergence equation $\nabla \cdot \vec{E} = \rho/\epsilon_0$ (where $\rho$ is the charge density) is always satisfied without solving it.

### 2.1.3 Shape functions representing macroparticles

To calculate the force acting on a macroparticle, the $\vec{E}$ and $\vec{B}$ fields must be known at the particle position rather than on the fixed spatial grid. Similarly the current has to be deposited at the grid locations to update the $\vec{E}$ field. Since each macroparticle contains many real particles it is necessary to choose a distribution of macroparticle weighting throughout the volume in phase space occupied by a macroparticle (see $S_x$ and $S_p$ in Eq. (2.2)).

In practice, the only momentum shape function $S_p$ used is the Dirac delta function. Using any other function would result in change of the spatial shape function $S_x$ in time, which is undesirable. Due to the fact that the momentum shape function is always the same, the term shape function will further indicate only the spatial shape function $S_x = S$.

(Spatial) shape functions have to be non-negative symmetric functions with compact support satisfying $\int S(\vec{x})d\vec{x} = 1$. The shape function should also allow for computationally inexpensive interpolation of fields and currents. These requirements are all satisfied by a class of functions called b-splines which have the support comparable to the cell size of the Eulerian grid and are piecewise low order polynomials [17].

The zero-th order b-spline (sometimes called top-hat function) is defined as

$$S_0(x) = \begin{cases} 1, & \text{if } x \le \frac{\Delta x}{2} \\ 0, & \text{otherwise} \end{cases} \tag{2.3}$$

The definition of b-splines of higher ($n$-th) order is recursive using convolutions:

$$S_n = S_{n-1} * S_0. \tag{2.4}$$

Since the shape functions defined above refer to the physical shape of macroparticles, interpolation from these shapes to find grid quantities, and the inverse of finding field quantities at macroparticle centers, requires weight functions which are the convolution of the shape function with top-hat function [18].

## 2.2 Numerical stability and accuracy, boundary conditions

Knowledge of stability conditions is crucial for all numerical methods. In PIC codes, numerical instability mostly manifests itself as a dramatic increase in the energy of the simulated system. However, numerical stability itself does not guarantee physically sound results. Even if the simulation is stable its results may be affected by various numerical artifacts. In order to reach numerical stability and satisfying accuracy of physical phenomena numerically investigated, simulation parameters have to be setup properly and appropriate boundary conditions, shape functions and possible smoothing algorithms have to be applied.

### 2.2.1 Setting of numerical parameters

PIC algorithm has a few general parameters important for accuracy, stability and computational demands of any simulation. Two most important numerical parameters are the time step $\Delta t$ and the spatial step $\Delta x$ also refereed to as cell width or as cell size. In multidimensional simulations, spatial steps in other directions $\Delta y$ and $\Delta z$ should be also taken into account. In most cases the spatial steps are all equal, but they can sometimes differ especially in highly computationally demanding PIC simulations where cell sizes are usually larger in transverse direction owing to laser beam propagation direction (e.g. [19]).

Time step is limited by Courant-Friedrichs-Lewy (CFL) condition required for stable propagation of electromagnetic waves. This condition also prohibits macroparticles from moving further than one cell per time step, otherwise the calculation of currents would be inaccurate. In the case of 3D PIC code, this condition sets the time step as follows:

$$\Delta t = \frac{K}{c} \cdot \frac{\Delta x \cdot \Delta y \cdot \Delta z}{\sqrt{\Delta x^2 + \Delta y^2 + \Delta z^2}}, \text{where } 0 < K < 1. \tag{2.5}$$

Usually constant $K$ is set close to 1.

The second condition for $\Delta t$ (2.6) stems from the requirement to ensure the propagation of electron plasma waves which have to be able to undergo oscillations with the electron plasma frequency $\omega_{pe}$.

$$\omega_{pe} \Delta t \leq 2 \tag{2.6}$$

Even if this condition is met, the simulated waves have slightly deformed frequency which is undesirable. It is therefore recommended to have even smaller time step than the condition requires.

The spatial step $\Delta x$ ($\Delta y$, $\Delta z$) has to be adjusted in order to resolve physical phenomena investigated and/or to reduce numerical heating [13, 20]. In order to resolve physical phenomena at plasma-vacuum boundary, the spatial step in the direction of large density gradient should be less then the plasma skin depth:

$$\Delta x \leq c/\omega_{pe}. \tag{2.7}$$

Numerical heating can emerge in PIC simulations due to the effects of aliasing of plasma waves [13]. The aliasing occurs when the waves of higher frequencies cannot be represented on a discrete grid, thus they are merged with the waves of lower frequencies. If the condition (2.8) is not satisfied, modes that are affected by Landau damping are aliased with those that aren't, which leads to nonphysical instability (called numerical heating) since the energy of plasma wave loses is not the same as the energy which macroparticles receive.

$$\Delta x \leq \pi \lambda_{De} \tag{2.8}$$

Here, $\lambda_{De}$ is the plasma Debye length. However, higher order shape functions [12] and current smoothing [17] used in modern PIC codes strongly reduce the effect of aliasing and the condition (2.8) is therefore not so relevant for the stability of PIC codes with higher order shape functions than top-hat function (2.3).

Finally, PIC simulation should initialize the number of numerical macroparticles per cells $N_{ppc}$ occupied by plasma. This parameter can be hardly defined explicitly and depends on many factors such as the phenomenon in plasma studied, range of plasma densities included in simulation or order of the shape functions used [21]. The setting of this parameter is mostly based on the user's experience with the PIC code.

### 2.2.2 Choice of appropriate boundary conditions

Boundary conditions have strong impact on the stability and numerical accuracy of the simulations. In fact, boundary conditions are artificial conditions which enables to keep a finite size of simulation domain. There are various boundary conditions for field and particles. Their choice mostly depends on the phenomenon studied together with user's experience. *Periodic* boundaries simply mean that field and/or particles reaching one edge of the domain are wrapped round to the opposite boundary. *Open* boundaries mean that electromagnetic (EM) waves outflowing characteristics propagate through the boundary, whereas particles are simply removed from the simulation when they reach the boundary. EM waves impinging on the boundary should be transmitted with as little reflection as possible. In order to further reduce the amount of reflected EM waves from the boundary, the so-called perfectly matched layer boundary conditions can be used, alternatively called *absorbing* boundaries (e.g., [22]). In PIC simulations with plasma layer reaching the boundary of simulation domain, *reflecting* or *thermal* boundary conditions can be applied. The latter means the using of "thermal bath" of particles at the boundary. When a (macro)particle leaves the simulation domain it is replaced with an incoming particle sampled from a Maxwellian velocity distribution given by a temperature corresponding to that of the initial conditions.

## 2.3 PIC simulations on large computer clusters

Large PIC simulations involve calculations with $10^9 - 10^{10}$ particles and similar number of cells. This huge amount of particles and cells has high demands on computational time and computer and storage memory. For example, each of our last 3D simulations (see Appendix A) used more than 1 TB of computer memory and spent more than $10^5$ CPU core hours per run. Each simulation run also produced several terabytes of data which should be archived. Since these simulations can run only on large computer clusters, modern PIC codes have to treat with simulation domain decomposition, distributed memory and parallel input/output.

Large computer clusters are usually composed of plenty of nodes, each of them has typically several tens of CPU cores. PIC code has to divide the simulation domain into pieces (subdomains) distributed to each node. Efficient algorithm of PIC code should ensure uniformly distributed workload between all nodes as much as possible. Also the amount of required computer memory per node should be balanced during the whole simulation run. Otherwise the simulation can crash in the overloaded node.

The decomposition of the whole simulation domain should be based on the equal number of macroparticles and cells per cluster node. However, this is mostly impossible, especially in the case of small very dense plasma regions surrounded by large vacuum region (e.g. ionized thin solid foils). Therefore, massively parallel PIC codes define internal rules for domain decomposition taking into account the number of macroparticles and cells with certain weights. Larger weight is usually attributed to the number of macroparticles per node since the calculation of particle motion is usually the most demanding on computational time.

When large data files are produced in PIC simulation run, they can be processed into smaller files with selected data or analyzed directly on a cluster node. Since the amount of stored data is usually limited on computer clusters, they can be transmitted to and archived in data storage centers, some of them are freely accessible for academic purposes.

## CHAPTER 3

# Laser-driven ion acceleration mechanisms

Apart from electrons, which can be accelerated directly by oscillating laser waves to relativistic energies, any energetic ions observed in laser-matter interaction experiments till now have not been accelerated directly by the laser field. A common feature of laser-driven ion acceleration mechanisms is that ions are accelerated by intense electric fields which arise from strong charge separations in plasma directly or indirectly induced by the laser-target interaction. Various ion acceleration mechanisms have been described depending on the interaction conditions (i.e., on the laser and target parameters).

In most of experiments, ions are accelerated when thin solid foils are irradiated by intense ($I > 10^{18}\ \mathrm{W/cm^2}$) laser pulses of duration of several tens or several hundreds of femtoseconds. In this case, mostly *target normal sheath acceleration* (TNSA) mechanism has been reported and some features attributed to *radiation pressure acceleration* (RPA) mechanism have been observed for the most intense pulses. When the foil expands during the interaction with laser pulse of duration of several hundreds of femtoseconds and of a high intensity, the target may become transparent for laser radiation and the so-called *break-out afterburner* (BOA) occurs. Partially expanded foils to lower densities due to laser prepulses may also result in the propagation of the main laser pulse through the so-called near-critical density plasma where *magnetic vortex acceleration* (MVA) is expected. Alternative targets such as gas clusters or liquid submicron droplets can lead to the acceleration of protons by *Coulomb explosion*.

Some of the mechanisms can work simultaneously or subsequently. For example, part of the ions can be accelerated in the target interior by RPA in the so-called hole boring regime and subsequently post-accelerated by TNSA when they reach the rear side of the target as discussed in detail in Appendix A. In the following sections of this chapter, each of the mechanisms mentioned above will be briefly discussed.

## 3.1 Target Normal Sheath Acceleration

When solid density targets and a high laser pulse contrast (preventing target's preheating and expansion before the main pulse arrives) are used, the energy of laser pulse can be absorbed by electrons in a thin surface layer of the target irradiated by the laser. These hot electrons can be generated by various complex mechanisms which are still discussed [23, 24]. Since hot electrons represent a population of electrons to which we can attribute velocities much higher than would correspond to the temperature of bulk electrons, they can transport absorbed laser energy through the target with only weak losses given by collisions [8]. Also the current of hot electrons can be easily neutralized in plasma by return currents in the opposite direction [25, 26], thus they can relatively freely travel through the targets and escape from them. However, when they start to escape the target, quasineutrality of plasma is violated and the electrons are decelerated by induced electrostatic field behind the surface of the target. The escaping electrons can be reversed back and they can subsequently oscillate back and forth through the target which would even enhance generated electrostatic field at plasma-vacuum boundary [27, 28].

This electrostatic field is sustained during and a short time after the interaction of laser pulse with ionized dense target. Its strength is close to the laser pulse amplitudes, but it remains for much longer time compared with laser wave period. Therefore this quasistatic field accelerates ions located on the target surface at the same time. The most energetic ions (in terms of kinetic energy per nucleon) are usually protons as they have the largest charge to mass ratio and they are present in a sufficient amount on the surface of targets at least in the layer with hydrocarbon impurities. Heavy ions can be also efficiently accelerated from cleaned targets. Such cleaning techniques like target heating

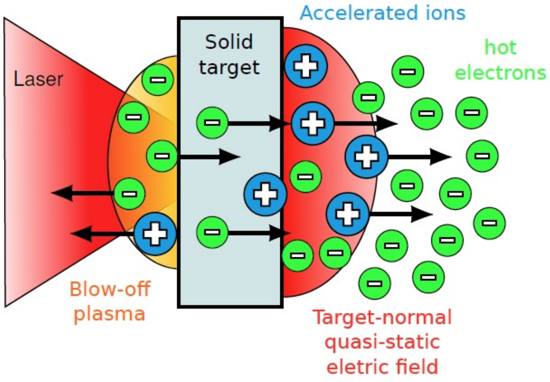

Figure 2: Scheme of TNSA mechanism [29]. Electrons are heated on the front (laser-irradiated) side of the target and they cross the target. Electrostatic fields are generated at plasma-vacuum boundaries when electrons leave the target. Subsequently, the electrons are slowed down, reversed back, and the ions from the surface layer are accelerated in the target normal direction by the generated quasi-static electric field.

and laser ablation permit to remove almost all protons and other contaminants from the target [30, 31].

Energy spectrum of ions accelerated by this mechanism has mostly exponentially decreasing form theoretically given by [32]

$$\mathrm{dN/d\varepsilon_i \approx K_1/\sqrt{\varepsilon_i T_h} \times \exp\left(-\sqrt{K_2\varepsilon_i/T_h}\right), \quad \varepsilon_i \leq \varepsilon_{imax},} \tag{3.1}$$

where $K_1$ and $K_2$ are constants and $\varepsilon_i$ is the kinetic energy of accelerated ions. This shape of the spectrum has been derived assuming isothermal expansion of plasma into vacuum [33] driven by hot electrons with constant temperature $T_h$ (defined in energy units, usually electronvolts) and single ion species. When more ion species and limited transverse size of the targets is assumed, this shape can be strongly modulated [34].

In the isothermal model, the maximum energy of accelerated ions $\varepsilon_{imax}$ depends on $T_h$ and normalized dimensionless acceleration time $\tau = \omega_{pi}t_{acc}/\sqrt{2\exp(1)}$, where the frequency $\omega_{pi} = \sqrt{(Ze^2n_h)/(m_i\epsilon_0)}$ is proportional to the square root of hot electron density $n_h$ (here, $Z$ is the ion charge, $m_i$ ion mass, $\epsilon_0$ vacuum permittivity) and ion acceleration time $t_{acc}$ is comparable to the laser pulse duration [35].

$$\varepsilon_{imax} = 2ZT_h \ln^2\left(\tau + \sqrt{\tau^2+1}\right) \tag{3.2}$$

Alternatively, the maximum energy $\varepsilon_{imax}$ can be estimated knowing the normalized maximum energy of the laser produced hot electrons $\varepsilon_{emax}/T_h$ trapped in the electrostatic potential created by the targets ions and by themselves, using empirical formula or numerical simulations [36].

## 3.2 Radiation Pressure Acceleration

The nonlinear force acting on particles by laser field can be expressed as

$$\vec{F_{NL}} = -\frac{e^2}{2m_e\omega^2}\nabla(\vec{E}^2), \tag{3.3}$$

where $\vec{E}(\vec{x}, t)$ is the electric field of laser wave and $\omega$ is the laser angular frequency. Generally this force has an oscillatory part with frequency $2\omega$ and a steady part proportional to $\sim < \vec{E}^2 > (\vec{x})$ called the ponderomotive force [2]. Radiation pressure is related to the total steady ponderomotive force acting on an overdense plasma.

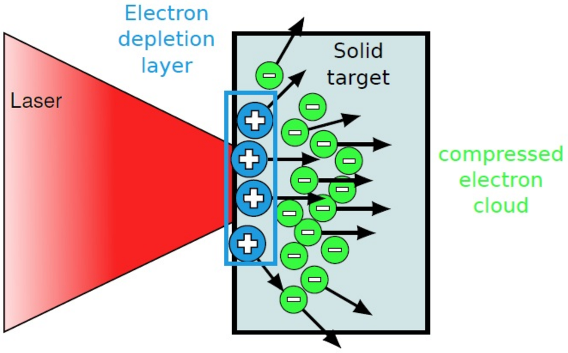

Figure 3: Scheme of RPA mechanism [29]. Radiation pressure created by incident laser pulse compresses the electron cloud towards target interior. Then, the ions are accelerated from the electron depletion layer by generated quasi-static electric field due to charge separation.

When an ionized target is irradiated by laser pulse, electrons from the front layer are pushed inside the target by the ponderomotive force forming compressed cloud in the skin layer till equilibrium between electrostatic potential arising from the charge separation and ponderomotive potential is established. Electrostatic field in turn acts on the ions and leads to their acceleration. When the first layer of ions is accelerated, electrostatic potential at the position of the compressed electrons is decreasing, equilibrium between electrostatic and ponderomotive potentials breaks and compressed electrons are again pushed inside the target. In the case of a thick target, this process known as *hole-boring*, is repeated until the laser pulse penetrates through the foil. On the contrary, if the target is thin enough and has a low mass, it can be accelerated as a whole in the so-called *light sail* regime.

### 3.2.1 Hole Boring regime

By assuming only the steady component of (3.3), the velocity of the motion of the compressed electron cloud (thus, the recession velocity of the plasma surface), also named the hole boring velocity $v_{HB}$, may be simply estimated by balancing the electromagnetic and mass momentum flows in a planar geometry [37]. This theoretical analysis predicts

$$\frac{v_{HB}}{c} = \frac{\sqrt{\Xi}}{1+\sqrt{\Xi}}, \quad \Xi = \frac{I}{m_i n_i c^3} = \frac{n_c}{n_i}\frac{m_e}{m_i}a_0^2 \tag{3.4}$$

where $m_i$ ($m_e$) and $n_i$ are ion (electron) mass and density, respectively, $n_c$ denotes critical electron density, and $a_0 = eE_0/(m_e\omega c)$ is dimensionless laser pulse amplitude.

The ion energy can be calculated by assuming moving frame where the plasma surface is at rest and incoming ions with velocity $-v_{HB}$ are reflected back with the opposite velocity $+v_{HB}$ [38]. Using Lorentz transformations and switching back into laboratory frame, the energy of accelerated ions can be estimated as

$$\varepsilon = m_i c^2 \frac{2\Xi}{1+2\sqrt{\Xi}}. \tag{3.5}$$

This mechanism works only if the plasma is non-transparent for laser radiation. The threshold for plasma transparency neglecting relativistic effects is given by well known critical density of electrons in plasma $n_c$ defined in all classical books related to plasma physics, e.g. [39]. When electrons oscillate in laser wave with relativistic velocities, relativistically induced transparency (RIT) threshold has to be taken into account. As we have discussed above, the laser pulse strongly compress the electron fluid, raising the electron density at the pulse front considerably, which further complicates the situation. Taking into account these effects, the threshold for RIT should reach $a_0 \approx 0.65(n_e/n_c)^2$ for $n_e/n_c >> 1$ and thick targets (their thickness $l > 1\ \mu\mathrm{m}$) [40]. This relatively high RIT threshold ensures that HB RPA may produce high-energy proton bunches, especially when using light ions [41] (see also Appendix A).

### 3.2.2 Light Sale regime

When the target is thin enough that all the ions are accelerated before the end of the laser pulse, the laser is able to further accelerate ions to higher energies since the ions are not screened by a background plasma anymore. This thin target regime of RPA is called light sail (LS) meaning that a thin object of finite inertia receives a significant boost from radiation pressure. LS RPA has a fundamental limit on the maximum attainable ion energy which is determined by the group velocity of the laser. However, there are other limiting factors, more restrictive in practice. Due to the finite spot size, the target expands depending on the transverse intensity profile of the laser. During this expansion, the areal density of the target decreases, making the target transparent for radiation and effectively terminating the acceleration [42]. Rayleigh-Taylor like instability occuring in LS RPA strongly affects the quality of accelerated ion beams [43]. The final spot size and the instability also lead to the generation of hot electrons which further expand the target.

The optimal condition for LS RPA is given by laser amplitude and target density [44]

$$l_{opt} \approx \frac{a_0 \lambda}{\pi} \frac{n_c}{n_e}, \tag{3.6}$$

where $l_{opt}$ is the optimal target thickness ($\lambda$ is the laser wavelength). When the foil thickness $l < l_{opt}$, all electrons should be pushed away from the foil and the ions in the foil undergo a Coulomb explosion producing a broad ion spectrum. In the case of LS RPA regime, a narrow ion energy spectrum can be observed. The foil is accelerated as a whole, thus, all ion species have the same velocities [45]. In reality, there is a gaussian spatial profile of the laser beam and hot electron heating which broaden the energy spectrum [46]. Using flat top laser beam profile and circularly polarized beams should improve the characteristics of ion energy spectra [47, 48].

## 3.3 Breakout Afterburner

The acceleration mechanisms mentioned above occur when targets are non-transparent for laser radiation. Breakout afterburner (BOA) regime occurs when the initially opaque target becomes transparent to the laser pulse during the irradiation. This regime can be enabled both by the expanding target reducing the target density and by the relativistic motion of electrons leading to RIT. Theoretical and experimental studies of this regime [49, 50] have demonstrated that a strong acceleration occurs close to the onset of transparency in the target.

Generally, this mechanism works efficiently for laser pulses of the length of several hundreds of femtoseconds, where ionized foil has enough time to expand partially to reach RIT phase during the irradiation and ions can be preliminary accelerated. Latest theoretical analysis with the help of numerical PIC simulations [51] describes this mechanism in detail. It reveals that ions gain energy through a resonant interaction with a low-frequency high-amplitude electrostatic wave exited in the target. To fall into resonance with the wave, the ions have to be preliminary accelerated in the expanding sheath at the back of the target (by TNSA) even at early times when the phase velocity of the wave is relatively low. After the laser pulse breaks through the target, the evolution of the Buneman-like instability [52] can drive the wave to higher phase velocities, and this can facilitate continued acceleration to higher energies by the resonant particles.

This acceleration mechanism has been discussed with scepticism by most of our scientific community, therefore the origin of the fastest ions under interaction conditions reaching RIT during laser pulse interaction with the target has been investigated for more than a decade (e.g., [51, 52]). On the other hand, it is widely accepted that enhanced TNSA phase occurs when the laser start to propagate through "classically" overdense plasma. During the TNSA enhanced phase, the attenuated but finite oscillating laser field within the target rapidly heats the electrons in the target volume, not just on the target surface or in underdense preplasma. This results in an increased conversion efficiency of the laser into hot electrons and subsequently to the enhanced longitudinal field at the rear side of the target accelerating ions.

## 3.4 Magnetic Vortex Acceleration

This mechanism has been reported for interaction conditions when the plasma density is near critical density and an ultrashort laser pulse is sufficiently intense to penetrate through the target forming a density channel. Such interaction conditions can be reached by solid target preexpansion before the interaction with the main pulse [53]. Then, the thickness of created near-critical plasma can be much larger than the length of the laser pulse.

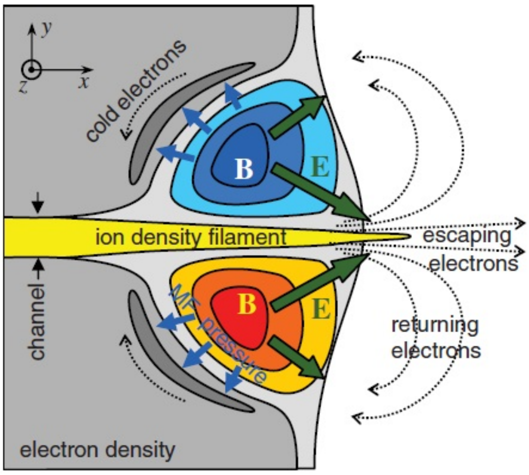

Figure 4: Scheme of the final phase of MVA mechanism [54] showing expanding magnetic field $B$ which generates longitudinal accelerating electric field $E$ and collimates the accelerated ions.

In the scenario of magnetic vortex acceleration (MVA), a tightly focused laser pulse interacts with the target and the ponderomotive force of the laser drives electron cavitation. Plasma electrons become trapped and accelerated behind the laser front, forming an axial fast current. Return current of electrons is generated to balance the fast current to maintain the plasma quasi-neutrality. The axial fast current generates the strong azimuthal magnetic field. When the density of the plasma is rapidly decreasing at the end of the channel formed by the laser pulse, the magnetic field expands into vacuum and the electron current is dissipated. This field has the form of a dipole in 2D and a toroidal vortex in 3D. As the magnetic vortex expands, a strong quasi-static electric field is generated at the rear side of plasma target which accelerates and collimates the ion beam to achieve higher energies [19, 55] (see also the sketch in Fig. 4).

## 3.5 Coulomb Explosion

When intense laser pulse irradiates small targets of subwavelength diameter (usually called clusters), all of electrons can be expelled from the target and the cloud of ions is accelerated due to its own charge. The laser pulse amplitude required for expelling all of electrons is [56]

$$a_0 > 34\sqrt{\frac{Zn_i}{5\times 10^{22}\ \mathrm{cm}^{-3}}}\left(\frac{R_0}{1\ \mu\mathrm{m}}\right), \tag{3.7}$$

where $Z$ is the ion charge, $n_i$ is the ion density in the ionized small target (cluster) of initial size (diameter) $R_0$. The ion energy spectrum (energy distribution) is proportional to the square root of energy [57]

$$\mathrm{dN/d}\varepsilon_\mathrm{i} = \frac{2\pi(3\epsilon_0)^{3/2}}{\mathrm{Z}^3\mathrm{e}^3}\sqrt{\frac{\varepsilon_\mathrm{i}}{\mathrm{n_i}}}, \quad \varepsilon_\mathrm{i} < \varepsilon_\mathrm{imax}. \tag{3.8}$$

This distribution is limited by maximum ion energy

$$\varepsilon_{imax} = \frac{Z^2e^2}{3\epsilon_0}n_iR_0^2 \approx 300Z^2\left(\frac{n_i}{5\times 10^{22}\ \mathrm{cm}^{-3}}\right)\left(\frac{R_0}{1\ \mu\mathrm{m}}\right)^2\ \mathrm{MeV}. \tag{3.9}$$

For example, assuming the droplet of solid hydrogen of the diameter of 100 nm which has the density close to $n_i \approx 5\times 10^{22}\ \mathrm{cm}^{-3}$, the laser pulse amplitude should exceed $a_0 > 3.4$ in order to reach Coulomb explosion of hydrogen ions to maximum energy $\varepsilon_{imax} \approx 3\ \mathrm{MeV}$.

The potential advantage of Coulomb explosion (CE) lies in the fact that the number of accelerated ions is increasing with their energy up to the maximum energy. On the other hand, the ions are emitted quasi-isotropically which reduces their applicability. (Nevertheless, some applications were successfully demonstrated, e.g., nuclear fusion from explosions of femtosecond laser-heated deuterium clusters [58].)

When the clusters are too large and/or the laser pulse intensity is too week, intermediate regimes between pure thermal expansion (TNSA) and CE can be studied [59, 60]. The parameter determining which type of acceleration prevails is defined as the ratio of cluster size to the Debye length of heated plasma composed of hot electrons $\Lambda = R_0/\lambda_D$ [61]. When $\Lambda >> 1$ the acceleration is driven mainly by hot electrons, whereas for $\Lambda < 1$ the acceleration is mostly driven by CE. The situation gets even more complicated when the interaction of laser pulse with a cloud of clusters is assumed which is more realistic situation in experiments. In this case, the final ion spectrum can be calculated by averaging the energy distribution of accelerated ions over the laser intensity distribution in the confocal area [62]. However, when the number of clusters per unit volume is relatively large collective effects becomes important, i.e., the expansion of each cluster is affected by neighboring clusters, see Appendix D.

CHAPTER 4

# Comments on selected publications

In the appendices of this thesis, several representative publications of the author are included, all of them related to the topic of laser-driven ion acceleration. In this chapter, we briefly summarize the main results of each paper and the contributions of the author to the topic.

Generally, we can divide these published papers into two main subcategories:

- ○ theoretical papers based on numerical particle-in-cell simulations (papers Nos. 1 - 5)
- ○ papers reporting experimental results accompanied with their theoretical explanation mostly based on numerical simulations (Nos. 6 - 8)

The author substantially contributed to all of those papers and he was the main and corresponding author in the first four papers introduced here. In the rest of the papers (Nos. 5 - 8), the author contributed by his results of numerical simulations and/or by the theoretical interpretation in the case of experiments.

## 4.1 Paper 1: Dominance of hole-boring radiation pressure acceleration regime with thin ribbon of ionized solid hydrogen

**Reference:**

**J. Psikal** and M. Matys. Dominance of hole-boring radiation pressure acceleration regime with thin ribbon of ionized solid hydrogen. *Plasma Physics and*

*Controlled Fusion*, **60**:044003, 2018.
Attached as Appendix A.

**Topic and Content:**

In real experiments, one can expect that various ion acceleration mechanisms can occur simultaneously. Most of theoretical papers is based on the detail study of a single acceleration mechanism which works well for strongly optimized conditions heavily achievable in laboratory. Therefore, it is highly desirable to asses the occurrence of various acceleration mechanisms under real interaction conditions.

In this paper, we demonstrated by multidimensional particle-in-cell simulations using the code EPOCH that HB RPA mechanism hugely dominates over TNSA both in numbers and maximum energy of accelerated protons for laser power of several PWs and pulse duration of several hundred femtoseconds by using ionized hydrogen ribbon of realistic thickness [63]. Such laser beam parameters should be available in near future in the frame of ELI-Beamlines project (laser L4) [64].

Detailed analysis have shown that most of protons is initially accelerated in the target interior by HB RPA mechanism and they can be further accelerated behind the target by electrostatic field generated by hot electrons. Since the HB velocity increases with decreasing ion density and ion mass (see Eq. (3.4)), hydrogen ribbon is the best candidate to demonstrate efficient HB RPA compared with other solid targets such as plastic or metal foils. Even if a part of hydrogen target is evaporated and slightly expands before the arrival of the main laser pulse, thus the preplasma is formed, the effect of such preplasma is rather negligible on the final proton acceleration. Also the polarization of laser wave does not affect significantly the final results for the assumed laser pulse length.

**Contribution of the Author:**

- Development of the theory.
- Running highly computational demanding 3D particle-in-cell simulations.

- Analysis of the results, comparison of 2D and 3D simulations (with the second author).
- Main and corresponding author.

## 4.2 Paper 2: Hollow target for efficient generation of fast ions by ultrashort laser pulses

### Reference:

**J. Psikal**, J. Grym, L. Stolcova, J. Proska. Hollow target for efficient generation of fast ions by ultrashort laser pulses. *Physics of Plasmas*, **23**:123121, 2016. Attached as Appendix B.

### Topic and Content:

The efficiency of ion acceleration driven by high-power femtosecond laser pulses (in TNSA regime) strongly depends on the target thickness and on the absorption of laser pulse energy into the ionized solid target [4]. Several papers were published on the strongly enhanced absorption of ultrashort intense laser pulses up to 90% at the nanostructured front (laser-irradiated) surface (e.g., [65]). However, the thickness of designed targets mostly presents a severe limitation in the efficiency of proton acceleration in TNSA configuration.

In this paper, we proposed hollow target which can combine nanostructured surface with small target thickness, both favorable for efficient TNSA. We demonstrated by means of full 3D particle-in-cell simulations that the maximum energy of accelerated protons can be increased by about 30% compared with ultrathin flat foil and with the so-called nanospheres targets [66]. Moreover, the number of the accelerated high-energy protons from the hollow target is increased approximately by a factor of two compared with a flat foil of the same thickness. The enhanced proton acceleration is maintained with a larger incidence angle of the laser beam on the hollow target in contrast to the nanosphere target.

The procedure of the fabrication of hollow target was described in the second part of this paper. A prototype of the hollow target was successfully fabricated by focused ion beam (FIB) milling of a thin silicon nitride (SiN) membrane.

**Contribution of the Author:**

- Development of the theory.
- Running and analysis of highly computational demanding 3D particle-in-cell simulations.
- Coordination of fabrication of prototypes of hollow target by FIB milling (co-authors were involved in the fabrication of such targets, its design and diagnostics of first prototypes by electron microscopy).
- Main and corresponding author.

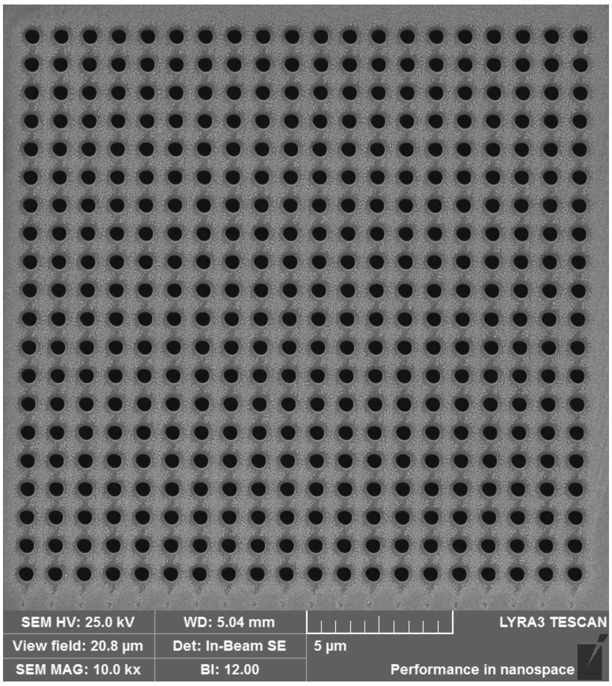
SEM HV: 25.0 kV
WD: 5.04 mm
LYRA3 TESCAN
View field: 20.8 μm
Det: In-Beam SE
5 μm
SEM MAG: 10.0 kx
BI: 12.00
Performance in nanospace

Figure 5: Scanning electron microscopy image of the hollow target shows a twenty-by-twenty array of holes with diameter of 500 nm in a silicon nitride membrane of the thickness of 200 nm fabricated by FIB milling. These targets were used in the first experimental tests at Institute of Plasma Physics and Laser Microfusion in Warsaw, Poland, made one year after the publication of the paper introduced above.

## 4.3 Paper 3: Increased efficiency of ion acceleration by using femtosecond laser pulses at higher harmonic frequency

**Reference:**

**J. Psikal**, O. Klimo, S. Weber, D. Margarone. Increased efficiency of ion acceleration by using femtosecond laser pulses at higher harmonic frequency. *Physics of Plasmas*, **21**:073108, 2014.
Attached as Appendix C.

**Topic and Content:**

When relativistically induced transparency (RIT) is achieved during laser-target interaction, the energy of accelerated ions is the highest in comparison with all other experimentally investigated regimes. This RIT acceleration regime, sometimes called BOA (laser break-out afterburner) [50], relies on the fact that the laser pulse can burn through the target. In the experiments with longer and relatively high energy pulses, this is achieved naturally due to rapid expansion of the target heated by the first part of the laser pulse [49]. With shorter pulses this can be however hardly achieved since extremely high laser intensity is required to reach RIT [40].

In this paper, we proposed another approach how to make the target relativistically transparent than increasing the laser pulse power (i.e., the intensity). Since the laser intensity required for RIT is directly proportional to $\lambda^2 \sim 1/\omega^2$ (where $\lambda$ is the laser wavelength and $\omega$ is the frequency), RIT is achievable more easily with higher (harmonic) laser frequency than the fundamental one. In our numerical simulations , we demonstrated the increase in maximum proton energy as well as the increase in the number of high-energy protons suitable for proton therapy [67] by factor 2 using the third harmonic frequency compared with fundamental frequency at optimal thickness of ionized plastic foil. Higher energies and numbers of accelerated ions are explained by a more efficient electron heating and acceleration in the whole target volume (given by the target thickness) when the target is relativistically transparent.

Such strong enhancement of laser-driven ion acceleration can surpass other enhancements which propose to use special targets like the ones with microstructures, foam, or grating on the surface. Moreover, flat foil targets can be more easily produced than other special targets, which is important from the point of view of future applications of high repetition rate femtosecond lasers.

**Contribution of the Author:**

- Development of the theory in collaboration with other co-authors.
- Running and analysis of particle-in-cell simulations.
- Main and corresponding author.

## 4.4 Paper 4: Simulations of femtosecond laser pulse interaction with spray target

**Reference:**

**J. Psikal**, O. Klimo, J. Limpouch. Simulations of femtosecond laser pulse interaction with spray target. *Laser and Particle Beams*, **32**:145-156, 2014.
Attached as Appendix D.

**Topic and Content:**

For the studies of femtosecond laser pulse interaction with matter and related particle acceleration, two types of targets are typically used. Gas-jets are usually used for the creation of underdense plasma, which permits electromagnetic waves to propagate and generate a wakefield accelerating electrons [68]. Thin solid foils are usually employed as a source of overdense plasma that transforms the laser pulse energy into accelerated ions efficiently [4]. However, alternative targets were also proposed. For example, experiments on proton acceleration [62, 69] and negative ion generation [70] were carried out with the so-called water spray target that consists of many submicron water droplets [71].

Motivated by the experimental results with the spray target that was proposed as a good candidate for efficient laser energy transfer to the target and thereby for particle acceleration, we investigated the interaction of femtosecond laser pulse with a cloud of multiple droplets of submicron diameter in this paper. We demonstrated by 2D PIC simulations that laser pulse energy can be efficiently absorbed in the cloud of the droplets. Strong laser absorption (up to 90%) and strong inhomogeneity of the target lead to relatively efficient ion acceleration, although the ions are accelerated in all directions with a relatively low anisotropy. The anisotropy of the acceleration is increased with decreasing inter-droplet distance, with increasing cloud thickness, and with growing laser pulse intensity. The advantage of the spray target is a relatively high number of ions accelerated near maximum (cut-off) energy and also ease of its use for high-repetition rate femtosecond lasers. However, laser absorption and the efficiency of proton acceleration are reduced at ultrahigh laser intensities ($I > 10^{21}$ W/cm$^2$). At such high laser amplitudes, electrons are almost completely removed from submicron droplets and the acceleration is driven mainly by Coulomb explosion contrary to the thin foils up to the moment when the foil becomes relativistically transparent.

In experiment, the droplets can be strongly pre-evaporated due to the laser pulse pedestal (insufficient laser pulse contrast) which has significant influence on the proton energy spectra. As demonstrated by our simulations, plasma composed of pre-evaporated droplets before the arrival of the main laser pulse can behave similarly to the foil section (limited in transverse dimensions owing to laser propagation direction) and the peak in proton energy spectra near the cut-off energy can be formed due to the interaction between multiple ion species and their different charge-to-mass ratio [34].

**Contribution of the Author:**

- Development of the theory.

- Running and analysis of particle-in-cell simulations.

- Main and corresponding author.

## 4.5 Paper 5: Laser-induced ion acceleration at ultra-high laser intensities

**Reference:**

J. Limpouch, **J. Psikal**, T. Mocek. Laser-induced ion acceleration at ultra-high laser intensities. *Radiation Effects and Defects in Solids*, **170**(4):271-277, 2015. Attached as Appendix E.

**Topic and Content:**

In this paper, ion acceleration by ultrashort laser pulses ($\sim 30$ fs) of very high intensities of the order $10^{22}\ \mathrm{W/cm^2}$ is investigated by two-dimensional PIC simulations. Such laser intensities should be achievable in near future, therefore it is highly desirable to provide rough estimates of expected energies of accelerated particles as well as dominant acceleration mechanisms under real experimental conditions. We studied the interaction of tighly focused ultrashort laser pulse at 1 PW power level with plastic targets.

Our results demonstrated that normal laser incidence is preferable to oblique incidence for such high intensities partly due to relatively efficient $\vec{j} \times \vec{B}$ heating. When pure hydrogen target was assumed with the same electron density as it is in solid plastic target, the energies of accelerated protons are higher. Thus, substituting plastic targets by pure hydrogen target of the same electron density in simulations leads to a significant error. Maximum proton and carbon ion energies for linear polarization are higher than for circular one due to enhanced electron heating in the case of linear polarization.

While the TNSA mechanism dominates in thick targets (the targets thicker than hole boring distance), RPA dominates for thin foils (the targets thinner than the hole boring distance). Both protons and carbon ions are accelerated to significantly higher energies for the thin foils. Protons at the front side of the thin foil are efficiently accelerated by an intense narrow peak of the longitudinal electric field and they overtake protons accelerated by the TNSA mechanism at the foil rear side at the laser pulse end, when nearly all protons from whole target thickness are ahead of the carbon ions.

**Contribution of the Author:**

- Development of the theory in collaboration with other co-authors.
- Running and analysis of particle-in-cell simulations.
- Preparation of figures and corrections in the manuscript.

## 4.6 Paper 6: Manipulation of laser-accelerated proton beam profiles by nanostructured and microstructured targets

**Reference:**

L. Giuffrida, K. Svensson, **J. Psikal**, M. Dalui, H. Ekerfelt, I. Gallardo Gonzalez, O. Lundh, A. Persson, P. Lutoslawski, V. Scuderi, J. Kaufman, T. Wiste, T. Lastovicka, A. Picciotto, A. Bagolini, M. Crivellari, P. Bellutti, G. Milluzzo, G.A.P. Cirrone, J. Magnusson, A. Gonoskov, G. Kon, C-G. Wahlstrom, D. Margarone. Manipulation of laser-accelerated proton beam profiles by nanostructured and microstructured targets. *Physical Review Accelerators and Beams*, **20**:081301, 2017.
Attached as Appendix F.

**Topic and Content:**

This paper deals with laser-driven proton acceleration from nano-/micro-structured thin foils experimentally investigated in TNSA regime. The experiment was conducted at Lund University using their Ti:sapphire laser system with plasma mirror [72] delivering laser pulses of duration 35 fs with ultrahigh contrast ($10^9$) and peak intensity $6 \times 10^{19}$ W/cm$^2$. Experimental results were interpreted with the help of 3D PIC simulations.

Monolayers of polystyrene nanospheres were placed on the rear surfaces of thin plastic targets to improve the spatial homogeneity of the accelerated proton beams. The final proton beam spatial profile had a larger divergence and a more homogeneous spatial distribution compared to a proton beam emerging from a flat plastic foil of equivalent total thickness. This effect was explained through a larger transverse emittance of the generated proton beam due to the microcurved surface, which smoothes down beam inhomogeneity compared to flat targets [73].

Grating structures of $\mu\mathrm{m}$ size covering the rear of silicon nitride targets were also used to modify the proton beam spatial distribution, reducing its divergence in the direction parallel to the grating orientation and stretching it in the perpendicular direction due to transverse electric fields generated inside the target grooves.

### Contribution of the Author:

- Participation in the proposal for experiment.
- Theoretical interpretation of experimental results with other co-authors.
- Running and analysis of 3D particle-in-cell simulations.
- Preparation of the figures related to PIC simulations included in the manuscript.
- Preparation of the response to referees related to theoretical interpretation of the experiment during the revision of the manuscript.

## 4.7 Paper 7: Laser-driven high-energy proton beam with homogeneous spatial profile from a nanosphere target

### Reference:

D. Margarone, I.J. Kim, **J. Psikal**, J. Kaufman, T. Mocek, I.W. Choi, L. Stolcova, J. Proska, A. Choukourov, I. Melnichuk, O. Klimo, J. Limpouch, J.H. Sung, S.K. Lee, G. Korn, T.M. Jeong. Laser-driven high-energy proton beam with homogeneous spatial profile from a nanosphere target. *Physical Review Special Topics - Accelerators and Beams*, **18**:071304, 2015.
Attached as Appendix G.

### Topic and Content:

Insulator targets have been widely investigated by research groups working in the field of laser-driven ion acceleration since they allow to reduce shot-to-shot fluctuations in the accelerated proton beam number compared to metallic foils where the protons are accelerated from hydrocarbon impurities on the target rear side [74]. On the other hand, dielectric targets typically show an inhomogeneous spatial profile of accelerated protons due to filamentation effects of the hot electrons which develop during their propagation through the insulator foil [75, 76]. This is a clear drawback which typically limits the use of such targets, especially when ultrahigh intensities, and hence large hot electron current densities, are used.

In this paper, we have shown experimentally that nanosphere dielectric target (composed of monolayer of polystyrene nanospheres deposited on the front, i.e., laser-irradiated, surface of thin plastic foil) can produce a homogeneous beam profile with a constant divergence angle. The experiment was performed with petawatt laser facility operating at the Center for Relativistic Laser Science (CoReLS), Institute for Basic Science (IBS) in Korea providing 30 fs laser pulses with peak intensity about $7 \times 10^{20}\ \mathrm{W/cm^2}$ [77]. The homogeneous proton beam profile can be explained by the mitigation of hot electron instabilities (filamentation) due to an increased transverse momentum component of heated electrons compared with flat foils observed in our PIC simulations. From a practical point of view, the improved spatial features obtained with a micron-thick nanosphere dielectric target offer additional benefits in delivering proton beams to a potential user station for applications through a beam transport system using magnetic optics.

**Contribution of the Author:**

- Theoretical interpretation of experimental results with other co-authors.
- Running and analysis of particle-in-cell simulations.
- Preparation of the figures related to PIC simulations included in the manuscript.
- Preparation of the response to referees related to theoretical interpretation of the experiment during the revision of the manuscript.

## 4.8 Paper 8: Proton acceleration driven by a nanosecond laser from a cryogenic thin solid-hydrogen ribbon

**Reference:**

D. Margarone, A. Velyhan, J. Dostal, J. Ullschmied, J.P. Perin, D. Chatain, S. Garcia, P. Bonnay, T. Pisarczyk, R. Dudzak, M. Rosinski, J. Krasa, L. Giuffrida, J. Prokupek, V. Scuderi, **J. Psikal**, M. Kucharik, M. De Marco, J. Cikhardt, E. Krousky, Z. Kalinowska, T. Chodukowski, G.A.P. Cirrone, G. Korn. Proton Acceleration Driven by a Nanosecond Laser from a Cryogenic Thin Solid-Hydrogen Ribbon. *Physical Review X*, **6**:041030, 2016.
Attached as Appendix H.

**Topic and Content:**

The using of solid hydrogen target irradiated by a high-power laser pulse for the generation of accelerated proton beam was experimentally demonstrated and reported in this paper. Here, we observed a collimated stream of protons in the range 0.1-1 MeV carrying a very high energy of about 30 J ($\sim 5\%$ laser-ion conversion efficiency) generated by a subnanosecond laser (PALS kJ-class laser facility) with an intensity of $\sim 3 \times 10^{16}\ \mathrm{W/cm^2}$ from $60\ \mu\mathrm{m}$ thick hydrogen ribbon [63]. This conversion efficiency is twice or three times higher than observed for standard plastic foils in the same irradiation conditions. Such efficient proton acceleration is ascribable to volumetric effects in the near critical density hydrogen plasma along the entire target thickness.

Although higher proton acceleration conversion efficiency (about 15% in 5-30 MeV energy range) was experimentally achieved for shorter pulses (using two temporally separated 800 fs laser beams and $5\ \mu\mathrm{m}$ thick Au foil) [78], our experimental achievement has never been reached with ns-class lasers operating at moderate laser intensities. Based on our PIC simulations assuming femtosecond laser pulses at higher intensities, the ion acceleration efficiency with a low density solid hydrogen target can reach values of about 25% compared with 10% calculated for plastic target. Lower density and lower ion mass in the generated plasma from hydrogen target compared with other solid targets can lead to different regimes of laser-target interaction and to substantial enhancement of laser-to-proton conversion efficiency, which is discussed in detail in this paper.

**Contribution of the Author:**

- Theoretical interpretation of experimental results with other co-authors.
- Running and analysis of particle-in-cell simulations.
- Collaboration in the preparation of the response to referees related to theoretical interpretation of the experiment during manuscript revision.

## 4.9 Main contributions of the listed publications

The main scientific contributions of the selected papers are related to the optimization of laser-driven proton acceleration source, here mostly based on various target design and composition. There are many free parameters in the studies of laser-target interaction, such as laser pulse duration, energy, focal spot size, pulse contrast, incidence angle of laser beam on target, laser polarization, wavelength, target thickness and its composition, shape, etc. Moreover, requirements on laser-driven proton beam characteristics may differ depending on application. It is expected that most of the requirements will be satisfied in the future with further development of laser technology (lasers will reach even higher intensities, repetition rate, reliability). However, we have demonstrated in our research papers that design and composition of the targets can be extremely important in order to reach more efficient acceleration regime or improved quality of accelerated ion beams. We have also shown that interaction regime can be modified by using larger laser frequency or higher laser intensity.

Chapter 5

# Conclusions

This thesis summarizes the work of the author in last five years in the field of laser-driven ion acceleration. This work has been based on the numerical simulations serving as a basis for the development of theory and interpretation of experimental results. The main results were published in 8 selected papers introduced in Chapter 4. Here, the content of those papers was briefly described and contribution of the author was specified for each of the paper. These papers are also included as appendices of the thesis.

The presented results are accompanied by a relatively short description of particle-in-cell simulation method in Chapter 2. The author briefly described various numerical algorithms used in PIC codes and was also concentrated on practical issues related to the using of PIC method (stability, accuracy, parallelization, data storage, ...). Laser-driven ion acceleration mechanisms mostly studied in current research papers are summarized in Chapter 3. Note that there is much more references related to each of the acceleration mechanism and there exists various terminology of the mechanisms. The author attempted to use mostly accepted terminology and acceleration mechanisms throughout this thesis as well as the most representative references.

Most of the author's work in last years was devoted to the study of the interaction of ultrashort laser pulses with specially designed targets. The using of those targets can improve the efficiency of laser-driven ion acceleration by improved laser pulse absorption and enhanced heating of hot electrons, or by increasing importance of an alternative acceleration mechanisms. It can also modify the properties of accelerated ion beams in terms of their homogeneity, divergence in various directions, etc. These studies were done with the help of very demanding numerical simulations and they contributed to the successful completion of two Czech Science Foundation projects (postdoctoral research project No. P205/12/P366 Advanced simulation studies of ion acceleration by ultrashort intense laser pulses and standard research project No. 15-02964S Ultra-intense laser interaction with specially-designed targets as a source of energetic particles and radiation, both running for three years) where the author played the role of principal investigator.

## 5.1 Future Work

Although the topic of laser-driven ion acceleration has been intensively studied by many experimental and theoretical groups in last two decades as can be seen in review papers [4, 79], there is enough open questions and unresolved problems. Some researchers compare the development of laser-driven particle acceleration with the history of conventional acceleration technology. The first (conventional) particle accelerator was constructed in 1930 and the subsequent development of this technology took many decades. Therefore, it is expected that laser-driven particle acceleration may be developed further over the next several decades, especially with increasing laser power, reliability of laser technology and higher repetition rate of lasers producing ultrashort pulses.

One of the main problems related to laser-driven ion acceleration is the role of finite pulse contrast. Increasing laser power does not require only larger pulse energy, but also enhanced contrast of the main pulse to laser pedestal [80]. The main femtosecond pulse is typically accompanied by a relatively low energy nanosecond prepulse which is a combination of subpicosecond pulses, a picosecond ramp and nanosecond amplified spontaneous emission. The nanosecond prepulse creates a preplasma at the front of irradiated target, but it can also completely destroy the target. In order to investigate the impact of the prepulses on the subsequent ion acceleration, a combination of hydrodynamics and particle-in-cell simulations has been usually applied [53, 81]. Nevertheless, the validity of various models have to be tested in the future.

In the studies of the occurrence or the combination of various acceleration mechanisms, three-dimensional and less dimensional PIC simulations may substantially differ [51]. That is also the case of quantitative numerical results in terms of maximum energies of accelerated ions or hot electron temperatures which are important for comparison with experiments [82, 83]. Therefore, the future research should also concentrate on the effects of dimensionality on the results of PIC simulations and on the efficiency of very demanding 3D simulations. Especially, the sensitivity of PIC simulations on numerical parameters (e.q. number of particles per cell, cell size) is not fully understood yet, even though the setting of those parameters strongly affects the accuracy of these simulations on the one hand and computational demands on the other hand.

Finally, phenomena such as relativistic induced transparency or even radiation friction may become crucial for the laser interaction with plasma and ion acceleration with increasing laser power (thus, laser intensity). Some studies of those effects were already published (e.g., [84, 85] or Appendix Appendix C), however, it is clear that more detailed investigation will be necessary in the future.

## 5.2 Collaboration with students

Scientific work at university is naturally connected with the education of students and a joint scientific collaboration. Many topics mentioned in this thesis have been investigated in collaboration with the students at Faculty of Nuclear Sciences and Physical Engineering CTU in Prague.

Martina Žáková investigated angular spread of ions accelerated from targets of various shapes irradiated by ultrashort laser pulses and subsequent reduction of divergence of accelerated ions in solenoid by numerical simulations in her Master thesis. She continues by the study of laser pulse interaction with near critical density plasma and magnetic vortex acceleration of ions in the frame of her Ph.D. thesis. Martin Matys collaborated in the research on the dominance of hole-boring radiation pressure acceleration regime with thin hydrogen ribbon (see Appendix A) during his Master thesis and in the beginning of his Ph.D. study. Viktor Kocur investigated how various setting of numerical parameters and the choice of shape function representing macroparticles affects the results of PIC simulations in his Bachelor and Master thesis. Robert Babjak has investigated the generation of hot electrons in detail by revealing particle trajectories in his PIC simulations.

The supervision of students can also enhance the overview of the author in other scientific topics related to laser plasma physics. For example, Tomáš Kerepecký has been studied betatron radiation and inverse Compton scattering by laser accelerated electrons.

# Bibliography

[1] P. Gibbon, *Short pulse laser interactions with matter: an introduction*. Imperial College Press, 2005.

[2] A. Seryi, *Unifying physics of accelerators, lasers, and plasma*. CRC Press, 2016.

[3] E. Esarey, C. B. Schroeder, and W. P. Leemans, "Physics of laser-driven plasma-based electron accelerators," *REVIEWS OF MODERN PHYSICS*, vol. 81, no. 3, pp. 1229–1285, 2009.

[4] A. Macchi, M. Borghesi, and M. Passoni, "Ion acceleration by superintense laser-plasma interaction," *REVIEWS OF MODERN PHYSICS*, vol. 85, no. 2, pp. 751–793, 2013.

[5] W. P. Leemans, A. J. Gonsalves, H. S. Mao, K. Nakamura, C. Benedetti, C. B. Schroeder, C. Toth, J. Daniels, D. E. Mittelberger, S. S. Bulanov, J. L. Vay, C. G. R. Geddes, and E. Esarey, "Multi-GeV Electron Beams from Capillary-Discharge-Guided Subpetawatt Laser Pulses in the Self-Trapping Regime," *PHYSICAL REVIEW LETTERS*, vol. 113, no. 24, p. 245002, 2014.

[6] F. Wagner, O. Deppert, C. Brabetz, P. Fiala, A. Kleinschmidt, P. Poth, V. A. Schanz, A. Tebartz, B. Zielbauer, M. Roth, T. Stoehlker, and V. Bagnoud, "Maximum Proton Energy above 85 MeV from the Relativistic Interaction of Laser Pulses with Micrometer Thick CH2 Targets," *PHYSICAL REVIEW LETTERS*, vol. 116, no. 20, p. 205002, 2016.

[7] S. Eliezer, *The interaction of high-power lasers with plasmas.* Institute of Physics Publishing, 2002.

[8] P. M. Bellan, *Fundamentals of plasma physics.* Cambridge University Press, 2006.

[9] T. W. Johnston, P. Bertrand, A. Ghizzo, M. Shoucri, E. Fijalkow, and M. R. Feix, “Stimulated Raman-scattering - Action evolution and particle trapping via Euler-Vlasov fluid simulation,” *PHYSICS OF FLUIDS B-PLASMA PHYSICS*, vol. 4, no. 8, pp. 2523–2537, 1992.

[10] M. Masek and K. Rohlena, “Intensity dependence of non-linear kinetic behaviour of stimulated Raman scattering in fusion relevant plasmas,” *EUROPEAN PHYSICAL JOURNAL D*, vol. 69, no. 4, p. 109, 2015.

[11] A. Pukhov, “Strong field interaction of laser radiation,” *REPORTS ON PROGRESS IN PHYSICS*, vol. 66, no. 1, pp. 47–101, 2003.

[12] T. D. Arber, K. Bennett, C. S. Brady, A. Lawrence-Douglas, M. G. Ramsay, N. J. Sircombe, P. Gillies, R. G. Evans, H. Schmitz, A. R. Bell, and C. P. Ridgers, “Contemporary particle-in-cell approach to laser-plasma modelling,” *PLASMA PHYSICS AND CONTROLLED FUSION*, vol. 57, no. 11, p. 113001, 2015.

[13] C. K. Birdsall and A. B. Langdon, *Plasma physics via computer simulation.* Taylor & Francis, 2005.

[14] T. Esirkepov, “Exact charge conservation scheme for Particle-in-Cell simulation with an arbitrary form-factor,” *COMPUTER PHYSICS COMMUNICATIONS*, vol. 135, no. 2, pp. 144–153, 2001.

[15] J. Villasenor and O. Buneman, “Rigorous charge conservation for local electromagnetic-field solvers,” *COMPUTER PHYSICS COMMUNICATIONS*, vol. 69, no. 2-3, pp. 306–316, 1992.

[16] T. Umeda, Y. Omura, T. Tominaga, and H. Matsumoto, “A new charge conservation method in electromagnetic particle-in-cell simulations,” *COMPUTER PHYSICS COMMUNICATIONS*, vol. 156, no. 1, pp. 73–85, 2003.

[17] E. Cormier-Michel, B. A. Shadwick, C. G. R. Geddes, E. Esarey, C. B. Schroeder, and W. P. Leemans, "Unphysical kinetic effects in particle-in-cell modeling of laser wakefield accelerators," *PHYSICAL REVIEW E*, vol. 78, no. 1, 2, p. 016404, 2008.

[18] S. Bennett, C. Brady, H. Schmitz, and C. Ridgers, *Developers Manual for the EPOCH PIC codes*. University of Warwick, 2013.

[19] A. Sharma, "High Energy electron and proton acceleration by circularly polarized laser pulse from near critical density hydrogen gas target," *SCIENTIFIC REPORTS*, vol. 8, p. 2191, 2018.

[20] H. Ueda, Y. Omura, H. Matsumoto, and T. Okuzawa, "A study of the numerical heating in electrostatic particle simulations," *COMPUTER PHYSICS COMMUNICATIONS*, vol. 79, no. 2, pp. 249–259, 1994.

[21] V. Kocur, "The effect of macroparticle number on particle-in-cell simulation results and computational demands in laser plasma physics," Master's thesis, Czech Technical University in Prague, Faculty of Nuclear Sciences and Physical Engineering, 2017.

[22] T. Umeda, Y. Omura, and H. Matsumoto, "An improved masking method for absorbing boundaries in electromagnetic particle simulations," *COMPUTER PHYSICS COMMUNICATIONS*, vol. 137, pp. 286–299, JUN 15 2001.

[23] Y.-Q. Cui, W.-M. Wang, Z.-M. Sheng, Y.-T. Li, and J. Zhang, "Laser absorption and hot electron temperature scalings in laser-plasma interactions," *PLASMA PHYSICS AND CONTROLLED FUSION*, vol. 55, no. 8, p. 085008, 2013.

[24] T. Liseykina, P. Mulser, and M. Murakami, "Collisionless absorption, hot electron generation, and energy scaling in intense laser-target interaction," *PHYSICS OF PLASMAS*, vol. 22, no. 3, p. 033302, 2015.

[25] Y. Sentoku, K. Mima, Z. Sheng, P. Kaw, K. Nishihara, and K. Nishikawa, "Three-dimensional particle-in-cell simulations of energetic electron generation and transport with relativistic laser pulses in overdense plasmas," *PHYSICAL REVIEW E*, vol. 65, no. 4, 2B, p. 046408, 2002.

[26] L. Gremillet, G. Bonnaud, and F. Amiranoff, “Filamented transport of laser-generated relativistic electrons penetrating a solid target,” *PHYSICS OF PLASMAS*, vol. 9, no. 3, pp. 941–948, 2002.

[27] Y. Sentoku, T. Cowan, A. Kemp, and H. Ruhl, “High energy proton acceleration in interaction of short laser pulse with dense plasma target,” *PHYSICS OF PLASMAS*, vol. 10, no. 5, 2, pp. 2009–2015, 2003.

[28] T. Ceccotti, A. Levy, H. Popescu, F. Reau, P. D’Oliveira, P. Monot, J. P. Geindre, E. Lefebvre, and P. Martin, “Proton acceleration with high-intensity ultrahigh-contrast laser pulses,” *PHYSICAL REVIEW LETTERS*, vol. 99, no. 18, p. 185002, 2007.

[29] M. Matys, “Ion acceleration driven by 10 PW laser,” Master’s thesis, Czech Technical University in Prague, Faculty of Nuclear Sciences and Physical Engineering, 2017.

[30] B. Hegelich, B. Albright, J. Cobble, K. Flippo, S. Letzring, M. Paffett, H. Ruhl, J. Schreiber, R. Schulze, and J. Fernandez, “Laser acceleration of quasi-monoenergetic MeV ion beams,” *NATURE*, vol. 439, no. 7075, pp. 441–444, 2006.

[31] K. Flippo, B. M. Hegelich, B. J. Albright, L. Yin, D. C. Gautier, S. Letzring, M. Schollmeier, J. Schreiber, R. Schulze, and J. C. Fernandez, “Laser-driven ion accelerators: Spectral control, monoenergetic ions and new acceleration mechanisms,” *LASER AND PARTICLE BEAMS*, vol. 25, no. 1, pp. 3–8, 2007.

[32] J. Psikal, *Ion acceleration in small-size targets by ultra-intense short laser pulses (simulation and theory)*. PhD thesis, Czech Technical University in Prague & University Bordeaux 1, 2009.

[33] P. Mora, “Plasma expansion into a vacuum,” *PHYSICAL REVIEW LETTERS*, vol. 90, no. 18, p. 185002, 2003.

[34] J. Psikal, V. T. Tikhonchuk, J. Limpouch, A. A. Andreev, and A. V. Brantov, “Ion acceleration by femtosecond laser pulses in small multispecies targets,” *PHYSICS OF PLASMAS*, vol. 15, no. 5, p. 053102, 2008.

[35] J. Fuchs, P. Antici, E. D'Humieres, E. Lefebvre, M. Borghesi, E. Brambrink, C. Cecchetti, M. Kaluza, V. Malka, M. Manclossi, S. Meyroneinc, P. Mora, J. Schreiber, T. Toncian, H. Pepin, and R. Audebert, "Laser-driven proton scaling laws and new paths towards energy increase," *NATURE PHYSICS*, vol. 2, no. 1, pp. 48–54, 2006.

[36] M. Passoni and M. Lontano, "Theory of light-ion acceleration driven by a strong charge separation," *PHYSICAL REVIEW LETTERS*, vol. 101, no. 11, p. 115001, 2008.

[37] A. P. L. Robinson, P. Gibbon, M. Zepf, S. Kar, R. G. Evans, and C. Bellei, "Relativistically correct hole-boring and ion acceleration by circularly polarized laser pulses," *PLASMA PHYSICS AND CONTROLLED FUSION*, vol. 51, no. 2, p. 024004, 2009.

[38] S. V. Bulanov, T. Z. Esirkepov, M. Kando, F. Pegoraro, S. S. Bulanov, C. G. R. Geddes, C. B. Schroeder, E. Esarey, and W. P. Leemans, "Ion acceleration from thin foil and extended plasma targets by slow electromagnetic wave and related ion-ion beam instability," *PHYSICS OF PLASMAS*, vol. 19, no. 10, p. 103105, 2012.

[39] F. F. Chen, *Introduction to plasma physics and controlled fusion*. Springer International Publishing, 2016.

[40] F. Cattani, A. Kim, D. Anderson, and M. Lisak, "Threshold of induced transparency in the relativistic interaction of an electromagnetic wave with overdense plasmas," *PHYSICAL REVIEW E*, vol. 62, no. 1, B, pp. 1234–1237, 2000.

[41] A. P. L. Robinson, R. M. G. M. Trines, N. P. Dover, and Z. Najmudin, "Hole-boring radiation pressure acceleration as a basis for producing high-energy proton bunches," *PLASMA PHYSICS AND CONTROLLED FUSION*, vol. 54, no. 11, p. 115001, 2012.

[42] S. S. Bulanov, E. Esarey, C. B. Schroeder, S. V. Bulanov, T. Z. Esirkepov, M. Kando, F. Pegoraro, and W. P. Leemans, "Radiation pressure acceleration: The factors limiting maximum attainable ion energy," *PHYSICS OF PLASMAS*, vol. 23, no. 5, p. 056703, 2016.

[43] C. A. J. Palmer, J. Schreiber, S. R. Nagel, N. P. Dover, C. Bellei, F. N. Beg, S. Bott, R. J. Clarke, A. E. Dangor, S. M. Hassan, P. Hilz, D. Jung, S. Kneip, S. P. D. Mangles, K. L. Lancaster, A. Rehman, A. P. L. Robinson, C. Spindloe, J. Szerypo, M. Tatarakis, M. Yeung, M. Zepf, and Z. Najmudin, "Rayleigh-Taylor Instability of an Ultrathin Foil Accelerated by the Radiation Pressure of an Intense Laser," *PHYSICAL REVIEW LETTERS*, vol. 108, no. 21, p. 225002, 2012.

[44] A. Macchi, S. Veghini, and F. Pegoraro, ""Light Sail" Acceleration Reexamined," *PHYSICAL REVIEW LETTERS*, vol. 103, no. 8, p. 085003, 2009.

[45] X. Zhang, B. Shen, X. Li, Z. Jin, and F. Wang, "Multistaged acceleration of ions by circularly polarized laser pulse: Monoenergetic ion beam generation," *PHYSICS OF PLASMAS*, vol. 14, no. 7, p. 073101, 2007.

[46] A. P. L. Robinson, M. Zepf, S. Kar, R. G. Evans, and C. Bellei, "Radiation pressure acceleration of thin foils with circularly polarized laser pulses," *NEW JOURNAL OF PHYSICS*, vol. 10, p. 013021, 2008.

[47] O. Klimo, J. Psikal, J. Limpouch, and V. T. Tikhonchuk, "Monoenergetic ion beams from ultrathin foils irradiated by ultrahigh-contrast circularly polarized laser pulses," *PHYSICAL REVIEW SPECIAL TOPICS-ACCELERATORS AND BEAMS*, vol. 11, no. 3, p. 031301, 2008.

[48] T. V. Liseykina, M. Borghesi, A. Macchi, and S. Tuveri, "Radiation pressure acceleration by ultraintense laser pulses," *PLASMA PHYSICS AND CONTROLLED FUSION*, vol. 50, no. 12, p. 124033, 2008.

[49] D. Jung, L. Yin, B. J. Albright, D. C. Gautier, S. Letzring, B. Dromey, M. Yeung, R. Hoerlein, R. Shah, S. Palaniyappan, K. Allinger, J. Schreiber, K. J. Bowers, H.-C. Wu, J. C. Fernandez, D. Habs, and B. M. Hegelich, "Efficient carbon ion beam generation from laser-driven volume acceleration," *NEW JOURNAL OF PHYSICS*, vol. 15, p. 023007, 2013.

[50] L. Yin, B. J. Albright, K. J. Bowers, D. Jung, J. C. Fernandez, and B. M. Hegelich, "Three-Dimensional Dynamics of Breakout Afterburner Ion Ac-

celeration Using High-Contrast Short-Pulse Laser and Nanoscale Targets," *PHYSICAL REVIEW LETTERS*, vol. 107, no. 4, p. 045003, 2011.

[51] D. J. Stark, L. Yin, B. J. Albright, W. Nystrom, and R. Bird, "A detailed examination of laser-ion acceleration mechanisms in the relativistic transparency regime using tracers," *PHYSICS OF PLASMAS*, vol. 25, no. 4, p. 043114, 2018.

[52] L. Yin, B. J. Albright, B. M. Hegelich, and J. C. Fernandez, "GeV laser ion acceleration from ultrathin targets: The laser break-out afterburner," *LASER AND PARTICLE BEAMS*, vol. 24, no. 2, pp. 291–298, 2006.

[53] A. Yogo, H. Daido, S. V. Bulanov, K. Nemoto, Y. Oishi, T. Nayuki, T. Fujii, K. Ogura, S. Orimo, A. Sagisaka, J. L. Ma, T. Z. Esirkepov, M. Mori, M. Nishiuchi, A. S. Pirozhkov, S. Nakamura, A. Noda, H. Nagatomo, T. Kimura, and T. Tajima, "Laser ion acceleration via control of the near-critical density target," *PHYSICAL REVIEW E*, vol. 77, no. 1, 2, p. 016401, 2008.

[54] S. V. Bulanov and T. Z. Esirkepov, "Comment on "Collimated multi-MeV ion beams from high-intensity laser interactions with underdense plasma"," *PHYSICAL REVIEW LETTERS*, vol. 98, no. 4, p. 049503, 2007.

[55] T. Nakamura, S. V. Bulanov, T. Z. Esirkepov, and M. Kando, "High-Energy Ions from Near-Critical Density Plasmas via Magnetic Vortex Acceleration," *PHYSICAL REVIEW LETTERS*, vol. 105, no. 13, p. 135002, 2010.

[56] S. Sakabe, S. Shimizu, M. Hashida, F. Sato, T. Tsuyukushi, K. Nishihara, S. Okihara, T. Kagawa, Y. Izawa, K. Imasaki, and T. Iida, "Generation of high-energy protons from the Coulomb explosion of hydrogen clusters by intense femtosecond laser pulses," *PHYSICAL REVIEW A*, vol. 69, no. 2, p. 023203, 2004.

[57] P. Parks, T. Cowan, R. Stephens, and E. Campbell, "Model of neutron-production rates from femtosecond-laser-cluster interactions," *PHYSICAL REVIEW A*, vol. 63, no. 6, p. 063203, 2001.

[58] T. Ditmire, J. Zweiback, V. Yanovsky, T. Cowan, G. Hays, and K. Wharton, "Nuclear fusion from explosions of femtosecond laser-heated deuterium clusters," *NATURE*, vol. 398, no. 6727, pp. 489–492, 1999.

[59] J. Psikal, O. Klimo, and J. Limpouch, "2D particle-in-cell simulations of ion acceleration in laser irradiated submicron clusters including field ionization," *PHYSICS OF PLASMAS*, vol. 19, no. 4, p. 043107, 2012.

[60] L. Di Lucchio, A. A. Andreev, and P. Gibbon, "Ion acceleration by intense, few-cycle laser pulses with nanodroplets," *PHYSICS OF PLASMAS*, vol. 22, no. 5, p. 053114, 2015.

[61] M. Murakami and M. Basko, "Self-similar expansion of finite-size non-quasi-neutral plasmas into vacuum: Relation to the problem of ion acceleration," *PHYSICS OF PLASMAS*, vol. 13, no. 1, p. 012105, 2006.

[62] S. Ter-Avetisyan, M. Schnuerer, P. V. Nickles, M. B. Smirnov, W. Sandner, A. Andreev, K. Platonov, J. Psikal, and V. Tikhonchuk, "Laser proton acceleration in a water spray target," *PHYSICS OF PLASMAS*, vol. 15, no. 8, p. 083106, 2008.

[63] S. Garcia, D. Chatain, and J. P. Perin, "Continuous production of a thin ribbon of solid hydrogen," *LASER AND PARTICLE BEAMS*, vol. 32, no. 4, pp. 569–575, 2014.

[64] B. Rus, P. Bakule, D. Kramer, J. Naylon, J. Thoma, J. T. Green, R. Antipenkov, M. Fibrich, J. Novak, F. Batysta, T. Mazanec, M. A. Drouin, K. Kasl, R. Base, D. Peceli, L. Koubikova, P. Trojek, R. Boge, J. C. Lagron, S. Vyhlidka, J. Weiss, J. Cupal, J. Hrebicek, P. Hribek, M. Durak, J. Polan, M. Koselja, G. Korn, M. Horacek, J. Horacek, B. Himmel, T. Havlicek, A. Honsa, P. Korous, M. Laub, C. Haefner, A. Bayramian, T. Spinka, C. Marshall, G. Johnson, S. Telford, J. Horner, B. Deri, T. Metzger, M. Schultze, P. Mason, K. Ertel, A. Lintern, J. Greenhalgh, C. Edwards, C. Hernandez-Gomez, J. Collier, T. Ditmire, E. Gaul, M. Martinez, C. Frederickson, D. Hammond, C. Malato, W. White, and J. Houzvicka, "ELI-Beamlines: Development of next generation short-pulse laser systems," in *RESEARCH USING EXTREME LIGHT: ENTERING NEW FRONTIERS*

*WITH PETAWATT-CLASS LASERS II*, vol. 9515 of *Proceedings of SPIE*, p. 95150F, 2015.

[65] L. Cao, Y. Gu, Z. Zhao, L. Cao, W. Huang, W. Zhou, X. T. He, W. Yu, and M. Y. Yu, "Enhanced absorption of intense short-pulse laser light by subwavelength nanolayered target," *PHYSICS OF PLASMAS*, vol. 17, no. 4, p. 043103, 2010.

[66] D. Margarone, O. Klimo, I. J. Kim, J. Prokupek, J. Limpouch, T. M. Jeong, T. Mocek, J. Psikal, H. T. Kim, J. Proska, K. H. Nam, L. Stolcova, I. W. Choi, S. K. Lee, J. H. Sung, T. J. Yu, and G. Korn, "Laser-Driven Proton Acceleration Enhancement by Nanostructured Foils," *PHYSICAL REVIEW LETTERS*, vol. 109, no. 23, p. 234801, 2012.

[67] U. Masood, M. Bussmann, T. E. Cowan, W. Enghardt, L. Karsch, F. Kroll, U. Schramm, and J. Pawelke, "A compact solution for ion beam therapy with laser accelerated protons," *APPLIED PHYSICS B-LASERS AND OPTICS*, vol. 117, no. 1, pp. 41–52, 2014.

[68] V. Malka, "Laser plasma accelerators," *PHYSICS OF PLASMAS*, vol. 19, no. 5, p. 055501, 2012.

[69] B. Ramakrishna, M. Murakami, M. Borghesi, L. Ehrentraut, P. V. Nickles, M. Schnuerer, S. Steinke, J. Psikal, V. Tikhonchuk, and S. Ter-Avetisyan, "Laser-driven quasimonoenergetic proton burst from water spray target," *PHYSICS OF PLASMAS*, vol. 17, no. 8, p. 083113, 2010.

[70] S. Ter-Avetisyan, B. Ramakrishna, M. Borghesi, D. Doria, M. Zepf, G. Sarri, L. Ehrentraut, A. Andreev, P. V. Nickles, S. Steinke, W. Sandner, M. Schnuerer, and V. Tikhonchuk, "MeV negative ion generation from ultra-intense laser interaction with a water spray," *APPLIED PHYSICS LETTERS*, vol. 99, no. 5, p. 051501, 2011.

[71] S. Ter-Avetisyan, M. Schnurer, H. Stiel, and P. Nickles, "A high-density sub-micron liquid spray for laser driven radiation sources," *JOURNAL OF PHYSICS D-APPLIED PHYSICS*, vol. 36, no. 19, pp. 2421–2426, 2003.

[72] B. Dromey, S. Kar, M. Zepf, and P. Foster, "The plasma mirror - A subpicosecond optical switch for ultrahigh power lasers," *REVIEW OF SCIENTIFIC INSTRUMENTS*, vol. 75, no. 3, pp. 645–649, 2004.

[73] L. Giuffrida, K. Svensson, J. Psikal, D. Margarone, P. Lutoslawski, V. Scuderi, G. Milluzzo, J. Kaufman, T. Wiste, M. Dalui, H. Ekerfelt, I. G. Gonzalez, O. Lundh, A. Persson, A. Picciotto, M. Crivellari, A. Bagolini, P. Bellutti, J. Magnusson, A. Gonoskov, L. Klimsa, J. Kopecek, T. Lastovicka, G. A. P. Cirrone, C. G. Wahlstrom, and G. Korn, "Nano and micro structured targets to modulate the spatial profile of laser driven proton beams," *JOURNAL OF INSTRUMENTATION*, vol. 12, p. C03040, 2017.

[74] R. Snavely, M. Key, S. Hatchett, T. Cowan, M. Roth, T. Phillips, M. Stoyer, E. Henry, T. Sangster, M. Singh, S. Wilks, A. MacKinnon, A. Offenberger, D. Pennington, K. Yasuike, A. Langdon, B. Lasinski, J. Johnson, M. Perry, and E. Campbell, "Intense high-energy proton beams from petawatt-laser irradiation of solids," *PHYSICAL REVIEW LETTERS*, vol. 85, no. 14, pp. 2945–2948, 2000.

[75] M. Roth, A. Blazevic, M. Geissel, T. Schlegel, T. Cowan, M. Allen, J. Gauthier, P. Audebert, J. Fuchs, J. Meyer-ter Vehn, M. Hegelich, S. Karsch, and A. Pukhov, "Energetic ions generated by laser pulses: A detailed study on target properties," *PHYSICAL REVIEW SPECIAL TOPICS-ACCELERATORS AND BEAMS*, vol. 5, no. 6, p. 061301, 2002.

[76] J. Fuchs, T. Cowan, P. Audebert, H. Ruhl, L. Gremillet, A. Kemp, M. Allen, A. Blazevic, J. Gauthier, M. Geissel, M. Hegelich, S. Karsch, P. Parks, M. Roth, Y. Sentoku, R. Stephens, and E. Campbell, "Spatial uniformity of laser-accelerated ultrahigh-current MeV electron propagation in metals and insulators," *PHYSICAL REVIEW LETTERS*, vol. 91, no. 25, p. 255002, 2003.

[77] T. M. Jeong and J. Lee, "Femtosecond petawatt laser," *ANNALEN DER PHYSIK*, vol. 526, no. 3-4, pp. 157–172, 2014.

[78] C. M. Brenner, A. P. L. Robinson, K. Markey, R. H. H. Scott, R. J. Gray, M. Rosinski, O. Deppert, J. Badziak, D. Batani, J. R. Davies, S. M. Hassan,

K. L. Lancaster, K. Li, I. O. Musgrave, P. A. Norreys, J. Pasley, M. Roth, H. P. Schlenvoigt, C. Spindloe, M. Tatarakis, T. Winstone, J. Wolowski, D. Wyatt, P. McKenna, and D. Neely, "High energy conversion efficiency in laser-proton acceleration by controlling laser-energy deposition onto thin foil targets," *APPLIED PHYSICS LETTERS*, vol. 104, no. 8, p. 081123, 2014.

[79] H. Daido, M. Nishiuchi, and A. S. Pirozhkov, "Review of laser-driven ion sources and their applications," *REPORTS ON PROGRESS IN PHYSICS*, vol. 75, no. 5, p. 056401, 2012.

[80] F. Wagner, C. Brabetz, O. Deppert, M. Roth, T. Stoehlker, A. Tauschwitz, A. Tebartz, B. Zielbauer, and V. Bagnoud, "Accelerating ions with high-energy short laser pulses from submicrometer thick targets," *HIGH POWER LASER SCIENCE AND ENGINEERING*, vol. 4, p. e45, 2016.

[81] T. Z. Esirkepov, J. K. Koga, A. Sunahara, T. Morita, M. Nishikino, K. Kageyama, H. Nagatomo, K. Nishihara, A. Sagisaka, H. Kotaki, T. Nakamura, Y. Fukuda, H. Okada, A. S. Pirozhkov, A. Yogo, M. Nishiuchi, H. Kiriyama, K. Kondo, M. Kando, and S. V. Bulanov, "Prepulse and amplified spontaneous emission effects on the interaction of a petawatt class laser with thin solid targets," *NUCLEAR INSTRUMENTS & METHODS IN PHYSICS RESEARCH SECTION A-ACCELERATORS SPECTROMETERS DETECTORS AND ASSOCIATED EQUIPMENT*, vol. 745, pp. 150–163, 2014.

[82] D. J. Stark, L. Yin, B. J. Albright, and F. Guo, "Effects of dimensionality on kinetic simulations of laser-ion acceleration in the transparency regime," *PHYSICS OF PLASMAS*, vol. 24, no. 5, p. 053103, 2017.

[83] E. d'Humieres, A. Brantov, V. Y. Bychenkov, and V. T. Tikhonchuk, "Optimization of laser-target interaction for proton acceleration," *PHYSICS OF PLASMAS*, vol. 20, no. 2, p. 023103, 2013.

[84] R. Capdessus and P. McKenna, "Influence of radiation reaction force on ultraintense laser-driven ion acceleration," *PHYSICAL REVIEW E*, vol. 91, no. 5, p. 053105, 2015.

[85] M. Tamburini, T. V. Liseykina, F. Pegoraro, and A. Macchi, “Radiation-pressure-dominant acceleration: Polarization and radiation reaction effects and energy increase in three-dimensional simulations,” *PHYSICAL REVIEW E*, vol. 85, no. 1, 2, p. 016407, 2012.

# Appendix A

# Paper 1

This paper is protected by publisher's Copyright which does not enable to include it in the university's electronic repository at that time. You can download it from the web site of publisher.

# APPENDIX B

# Paper 2

PHYSICS OF PLASMAS **23**, 123121 (2016)

# Hollow target for efficient generation of fast ions by ultrashort laser pulses

J. Psikal,[1,2,a)] J. Grym,[3] L. Stolcova,[1] and J. Proska[1]
[1]*FNSPE, Czech Technical University in Prague, Prague, Czech Republic*
[2]*ELI-Beamlines Project, Institute of Physics of the Czech Academy of Sciences, Prague, Czech Republic*
[3]*Institute of Photonics and Electronics of the Czech Academy of Sciences, Prague, Czech Republic*

(Received 21 June 2016; accepted 9 December 2016; published online 28 December 2016)

The efficiency of ion acceleration driven by high-power femtosecond laser pulses strongly depends on the target thickness and on the absorption of laser pulse energy into the ionized solid target. Enhanced absorption has been demonstrated for targets with submicrometer structures deposited on their front surface. However, increasing the overall thickness of the target by adding the layer with structures is undesirable. Here, microstructured hollow targets are proposed to enhance the absorption of the laser pulse energy while keeping the target thickness to minimum. It is demonstrated by full 3D particle-in-cell simulations that the efficiency of proton acceleration from hollow targets substantially exceeds the efficiency of the acceleration from flat foils of the same thickness. The fabrication of an ultrathin hollow target (prototype) by focused ion beam milling is also described. *Published by AIP Publishing*. [http://dx.doi.org/10.1063/1.4972880]

## I. INTRODUCTION

Ion acceleration driven by high-power femtosecond laser pulses has been attracting great interest since the start of the new millennium.[1,2] Most experimental groups have been studying ions accelerated from thin metal or insulator foil targets by the so-called Target Normal Sheath Acceleration (TNSA) mechanism.[3] In this scenario, the interaction of an ultrashort intense laser pulse with an ionized solid target is accompanied by the heating of electrons. Their subsequent expansion from the target surface leads to the generation of a strong quasi-static electric field in the sheath on the target surface, which accelerates ions. These are dominated by protons originating from low-Z hydrocarbon deposits on the target rear surface. Acceleration efficiency strongly depends on the target thickness[4–6] as well as on the absorption of the laser pulse energy into the ionized target (through the generation of hot electrons).[7]

In the last decade, several papers were published on the strongly enhanced absorption of ultrashort intense laser pulses at the nanostructured front (laser-irradiated) surface. It has been proposed that laser pulse absorption can reach 90% with a specially designed nanolayered target.[8] However, the thickness of the designed target (approx. 10 $\mu$m) presents a severe limitation in the efficiency of proton acceleration (in the TNSA configuration). From this point of view, thinner micro- and nanostructured targets are more attractive.

In 2D geometry, the shape of the considered structures is usually circular, rectangular, triangular, or sinusoidal.[9–11] In Ref. 9, structures of circular shapes were proposed to enhance laser absorption and laser-ion acceleration due to their simplicity (only one size can be optimized). These targets composed of flat foils with deposited monolayer of spheres of submicron diameter were successfully fabricated and enhanced ion acceleration has been confirmed at three successive experimental campaigns.[12,13]

Experimental results and numerical simulations have shown the optimal diameter of the sphere to be around 0.5 $\mu$m.[9,12] However, such targets have still limitations in the acceleration efficiency due to their minimum thickness given by the size of the spheres plus the thickness of the substrate on which the spheres are deposited. Therefore, we propose in this paper the hollow target which can combine nanostructured surface with small target thickness, both favorable for efficient laser-ion acceleration by ultrashort femtosecond laser pulses. A prototype of the hollow target has been successfully fabricated by focused ion beam (FIB) milling of a thin silicon nitride (SiN) membrane. The procedure is described in the second part of this paper.

We should note that the hollow (multi-hole) target for laser-proton acceleration has been theoretically proposed in Ref. 14. However, the idea was not further developed and only simple 2D simulations were introduced. Also, nanohole-alumina targets of the thickness of about 20 $\mu$m with a pore diameter from 40 nm to 450 nm[15–17] were employed to generate soft and hard x-ray radiation at lower laser intensities ($10^{17}$ W/cm$^2$).

## II. NUMERICAL SIMULATIONS OF LASER PULSE INTERACTION WITH HOLLOW TARGETS AND OF THE ENHANCED PROTON ACCELERATION

In the simulations, we assumed linearly p-polarized laser pulse of peak intensity $10^{21}$ W/cm$^2$. The laser pulse temporal profile was Gaussian with the length of 30 fs at the FWHM (in intensity), and the spatial profile of the pulse was Gaussian with the focal spot size of 3 $\mu$m at the FWHM. The laser pulse was incident on the target at the angles of 10° and 45° to the target normal. The parameter values were chosen to simulate a real PW-class laser used for experiments with nanostructured targets.[13]

The numerical study was performed using 2D and 3D versions of the particle-in-cell (PIC) code EPOCH.[18] First, preliminary 2D simulations with a relief rectangular structure

---

[a)] jan.psikal@fjfi.cvut.cz

RIGHTSLINK

(representing a 2D model of hollow target) deposited on the 200 nm thick substrate were run in order to optimize the parameters for hollow targets (see the supplementary material). These simulations demonstrated that the optimal diameter of the holes (gap in the 2D structure) as well as the optimal distance between the holes (width of the 2D rectangular structure) is about 500 nm. The thickness of the structured layer (thus, the thickness of the hollow target) should be larger than 150 nm. The results from 2D simulations are in agreement with an analytical model assuming the heating of electrons from the rectangular structure in the laser field and estimating the optimum value of the height, periodicity, and size for 2D rectangular structures at a given laser intensity.[10,11]

Second, 3D PIC simulations were run with optimized target parameters. Such 3D simulations are computationally expensive, but they are required in order to fully describe the geometry of the targets and to estimate the efficiency of proton acceleration. Three types of targets (see Fig. 1) have been compared - a flat foil of 200 nm thickness, a hollow target of the same thickness (an array of 10 × 10 holes with a diameter of 500 nm and a periodicity of 1 $\mu$m etched through the flat foil), and a monolayer of nanospheres with a diameter of 400 nm deposited on a 100 nm thick foil substrate (the so-called nanosphere target) in order to compare the previous proposal for microstructured target[9] with the new one. The plasma was composed of protons and heavier $C^{6+}$ ions with a ratio of 2:1, and the density of electrons was set to $1.75 \times 10^{23}\ \mathrm{cm}^{-3}$ ($\approx 100\ n_{ec}$, where $n_{ec}$ is the electron critical density) in order to avoid the transparency of the targets during laser-target interaction and to satisfy the computational constraints. The thickness of the targets was kept small but realistic for their fabrication.

The interaction of the laser pulse with the targets has been studied in a simulation box with dimensions of $32\,\mu\mathrm{m} \times 16\,\mu\mathrm{m} \times 16\,\mu\mathrm{m}$ for the incidence angle of 10° or in the box with dimensions of $28\,\mu\mathrm{m} \times 28\,\mu\mathrm{m} \times 16\,\mu\mathrm{m}$ for the incidence angle of 45°. Both simulation boxes consisted of cubic cells with a side length of 16 nm. 100 electrons, 25 protons, and 12.5 $C^{6+}$ ions in average were initialized per each cell occupied by the plasma at maximum density. Convolutional Perfectly Matched Layer (CPML) boundary conditions for fields[19] were applied at the simulation box boundaries. Particles were transmitted through the boundary and removed from the system. Collisions and ionization were not included in the PIC simulations. Since the targets are relatively thin and simultaneously the laser field on the

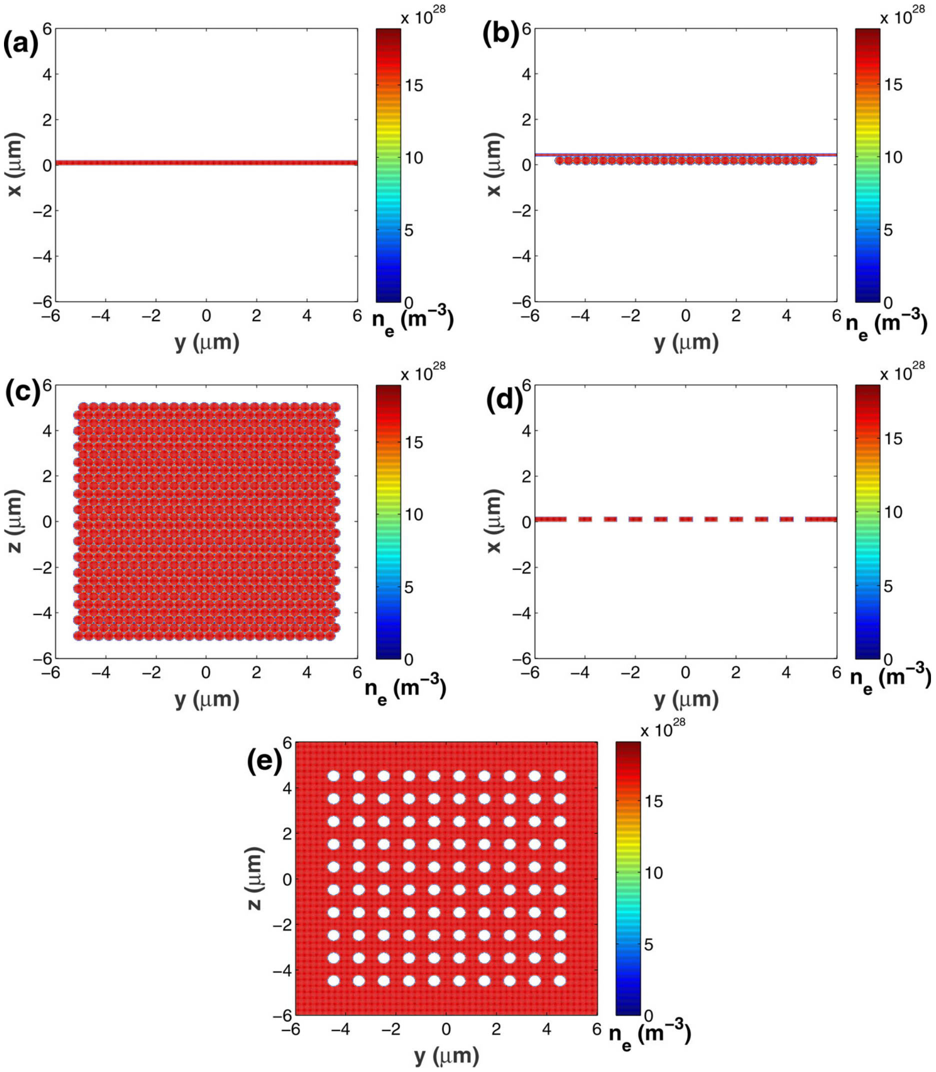

FIG. 1. Three types of targets investigated in our 3D simulations: 2D profiles of (a) flat foil (cross-section at $z = 0$), (b) nanosphere target (cross-section at $z = 0.2\,\mu\mathrm{m}$), (d) hollow target (cross-section at $z = 0.5\,\mu\mathrm{m}$) in the plane of laser propagation; 2D profiles (cross-sections at $x = 0.2\,\mu\mathrm{m}$) of (c) nanosphere target and (e) hollow target in the plane of the target surface.

RIGHTSLINK

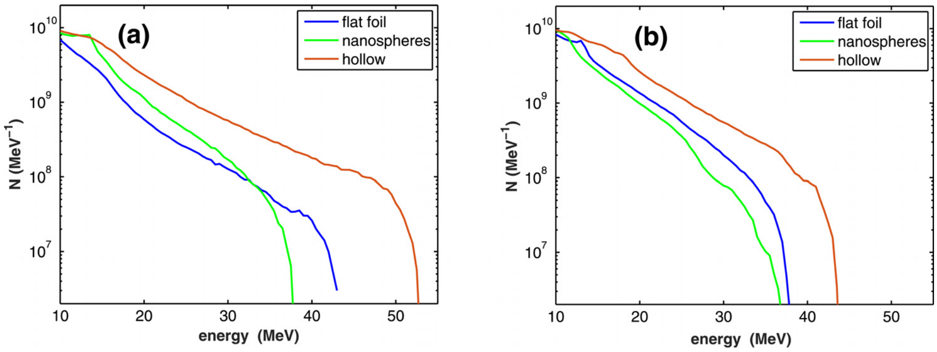

FIG. 2. Energy spectra of protons accelerated from three types of targets from 3D simulations: flat foil (200 nm thick), nanosphere target (spheres of diameter 400 nm deposited on 100 nm flat foil), and hollow target (200 nm thick with holes of diameter 500 nm). The spectra are shown for laser pulse incident on the target at (a) 10° and at (b) 45°.

target front side or the accelerating field on the target rear side is relatively high (sufficient to ionize the matter to a high degree and to heat the population of hot electrons moving with relativistic velocities), we do not expect the effects of collisions and ionization to have a significant influence on the proton acceleration efficiency.

We should note that all simulations were performed under the assumption that the laser pulse contrast is high enough to prevent the expansion of the target due to the laser pedestal before the arrival of the main laser pulse. Due to the fact that the thickness of the targets is smaller than the diameter of the holes, the hollow structure should survive if the whole ultrathin target itself is sustained by a sufficient laser pulse contrast level. Usually, these ultrathin targets have been employed in the experiments with ultrashort pulses of the length of about 30 fs generated by Ti:sapphire lasers.[20,21]

The final energy spectra of accelerated protons from the three targets investigated in our 3D simulations, presented in Fig. 2, show that the hollow target is favorable for the acceleration in terms of the maximum energy and the number of high energy protons for both incidence angles. In contrast, the acceleration efficiency for the nanosphere target is similar to flat foil at the larger incidence angle.[22] The results are summarized in Table I.

The enhancement of the proton acceleration from the hollow target can be explained by a higher efficiency of electron heating during laser pulse interaction with the nanostructured surface of the target. Hot electron temperature, characterizing heated electrons during the interaction,[23] reaches its highest value in simulations with the hollow target. Despite the efficient absorption of the laser pulse energy in the nanosphere targets and the corresponding increase in the number of heated electrons, the hot electron temperature is less enhanced.

TABLE I. Maximum proton energy $E_{pmax}$ and number of accelerated high-energy protons (with energy $E > 10\,\mathrm{MeV}$) in the forward direction $N_{p10}$, absorption of laser pulse energy in ionized targets $\kappa$, energy transformation efficiency into high-energy protons $\eta_{10}$, and hot electron temperature after laser-target interaction $T_h$. The targets are irradiated by 30 fs laser pulse at two incidence angles ($\theta = 10°$ and $\theta = 45°$).

| Type of target | $\theta$ | $E_{pmax}$ [MeV] | $N_{p10}$ | $\kappa$ | $\eta_{10}$ | $T_h$ [MeV] |
|---|---|---|---|---|---|---|
| Flat foil | 10° | 43 | $3.1 \times 10^{10}$ | 0.18 | 0.022 | 3.3 |
| Flat foil | 45° | 38 | $4.9 \times 10^{10}$ | 0.34 | 0.036 | 3.1 |
| Hollow | 10° | 52 | $7.5 \times 10^{10}$ | 0.41 | 0.062 | 4.5 |
| Hollow | 45° | 44 | $7.8 \times 10^{10}$ | 0.5 | 0.063 | 5.6 |
| Nanosphere | 10° | 38 | $5.3 \times 10^{10}$ | 0.46 | 0.038 | 3.6 |
| Nanosphere | 45° | 37 | $4.1 \times 10^{10}$ | 0.48 | 0.028 | 3.9 |

The observed increase in hot electron temperature can be ascribed to the local enhancement of the electric field in the presence of nanostructures (holes) on the target surface. Longitudinal and transverse electric fields inside the target surface layer are shown in Fig. 3 for the flat foil and the hollow target tested in 3D simulations with a laser pulse incidence angle of 10° to the target normal. Although the laser wave cannot propagate through the target with subwavelength holes, the laser field can interact with electrons at plasma-vacuum boundary inside the holes, at least in the target surface layer of the thickness of laser skin depth. Then, the laser field can extract electrons to vacuum from the structured surface and accelerate them back to the plasma, where they can easily get out of phase with the laser wave and thus gain their energy. The electron displacement from the target inner surface amplifies the electric field inside the holes in the longitudinal direction and in the transverse direction perpendicular to the laser field, which can accelerate electrons to larger energies.

Even though we observed an increase in the absorption of the laser pulse energy in ionized targets and the increase in the hot electron temperature for the larger incidence angle, the efficiency of proton acceleration was rather lower in this case, especially in terms of maximum proton energy. The increase in the absorption can be explained by a larger electric field component of the oscillating laser wave perpendicular to the target surface and larger projection of the spot size on the target irradiated by the laser beam at oblique incidence compared to close-to-normal incidence. On the other hand, a large number of hot electrons, especially in the case of structured targets, leave quickly the interaction region towards the lateral side of the targets in the case of 45° incidence angle due to a large initial spread of generated hot electrons; thus, they are not efficiently employed for the proton acceleration (large spread of hot electrons in the case of structured targets compared with flat foil is well illustrated in Fig. 4 in Ref. 13).

Besides the efficiency of the proton acceleration, it is also important to consider the angular distribution of the accelerated protons from the targets. In Fig. 4, angular distributions of the accelerated protons (with energy $E_p > 10\,\mathrm{MeV}$) are compared for the flat foil and the hollow target irradiated by a

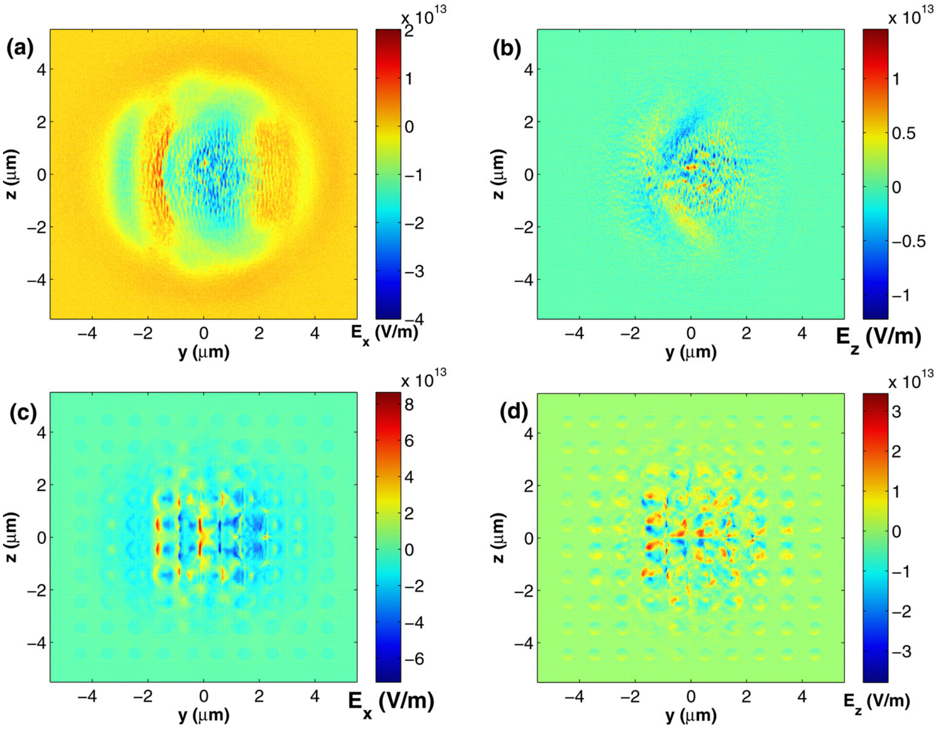

FIG. 3. Longitudinal and transverse (perpendicular to the oscillating laser field) electric fields, respectively, for flat foil ((a) and (b)) and for hollow target ((c) and (d)) in their front (laser-irradiated) target surface layer (at the depth of 30 nm from the initial plasma-vacuum boundary) for the simulations with laser incidence angle on the target equal to 10°. In the case of the hollow target, the field amplitudes are enhanced approximately two times.

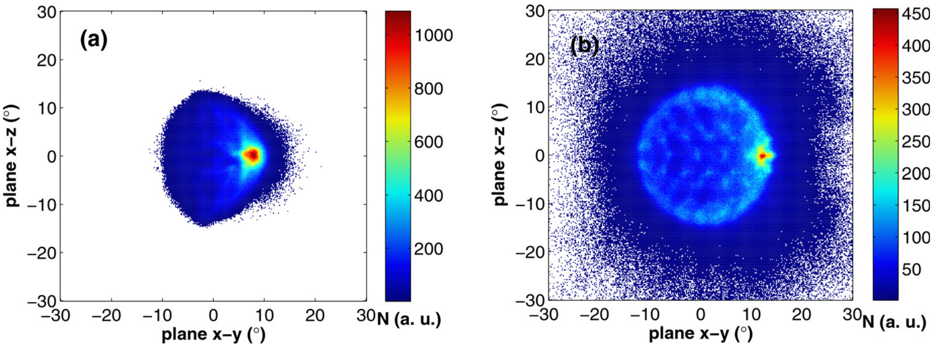

FIG. 4. Angular distributions of the accelerated high-energy protons (with energy $E_p > 10\,\text{MeV}$) from (a) the flat foil and (b) hollow target irradiated by a laser pulse at 45°.

laser at the incidence angle of 45°. The angular spread of each proton is calculated from momentum components as the deviation of proton trajectory from the target normal direction. The results show a broader angular spread of protons in the case of the hollow target which can be attributed to the nanostructured rear surface of the target (due to the presence of the holes through the target) in agreement with observations in a recent experiment with targets covered by a monolayer of nanospheres on the rear side.[24] This effect can be explained by a large transverse emittance of the generated proton beam due to the curved surface. To reduce the angular spread, we could design a target with a flat rear side, perforated only from the front side by a periodic array of microwells. However, manufacturing of such a target by focused ion beam milling (discussed in Section III) would be extremely challenging.

Fig. 4 shows that most protons are deflected from the target normal direction towards the laser pulse propagation direction. The average deflection angle of protons is about 5°, close to the theoretical prediction $\phi \approx \sqrt{E_p/(2m_pc^2)}\sin\theta$ in Ref. 25, where $E_p$ is the proton kinetic energy, $m_pc^2$ is the proton rest energy, and $\theta$ is the incidence angle of the laser beam on the target.

## III. MANUFACTURING OF HOLLOW TARGETS

The pronounced dependence of laser-driven proton acceleration efficiency on the target parameters imposes strict requirements on the quality of experimentally prepared targets. However, some factors affecting the reproducibility of the (proton acceleration) experiments, such as the target flatness, robustness/durability, or thickness homogeneity, might have been underrated in the past experimental campaigns, possibly due to the limited choice of materials available in the form of self-supporting thin layers. Silicon nitride (SiN) films are now commercially available in thicknesses down to several tens of nanometers with lateral dimensions up to centimeters. Their robustness, toughness, and flatness are ideally suited for advanced targetry. SiN films can either be used as supports or be directly patterned using standard nanotechnology procedures.

Focused ion beam (FIB) instruments are nowadays routinely used for milling, deposition, implantation, and imaging

RIGHTSLINK

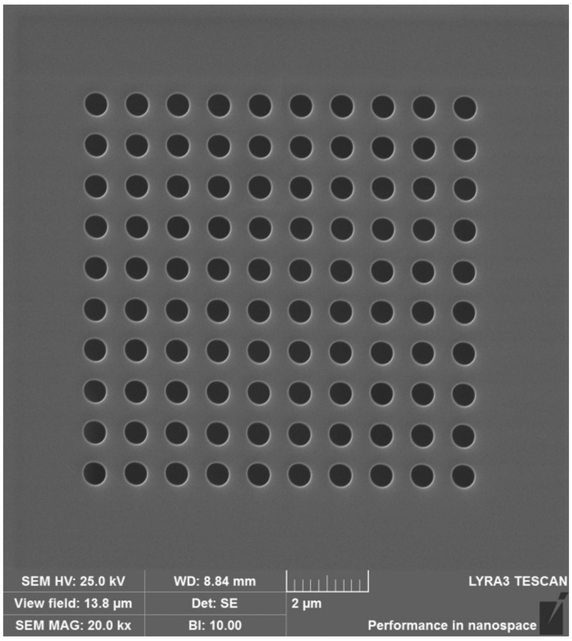

FIG. 5. Scanning electron microscopy image of the hollow target shows a ten-by-ten array of holes with the diameter of 500 nm in a silicon nitride membrane of the thickness of 500 nm fabricated by FIB milling.

of materials over a wide range of length scales. FIB is an excellent tool for rapid prototyping of nanostructures and nanodevices.[26] Dual beam instruments with both electron and ion beam columns enable to localize a desired position on a sample and to remove or deposit material with a high precision without a resist or an etching mask. By carefully controlling the ion beam it is possible to perform precise nanomachining, to produce minute components, or to remove the unwanted material. The ion species, their energy, the probe current, the spot size, and the scanning strategy are essential parameters to control the milling process.[27]

Prototypes of hollow targets were fabricated by FIB milling into 500 nm thick and 200 nm thick SiN membranes (Silson Ltd) using the Tescan Lyra 3GM FIB-SEM system. To reduce sample charging during exposure to electron and ion beams, the membranes were locally coated with a 2 nm layer of Pt by focused ion beam induced deposition.[28] A metalorganic precursor $(CH_3)_3Pt(CpCH_3)$ delivered by a gas injection system was dissociated by FIB to create a local layer of Pt. The example of a ten-by-ten array of holes with the diameter of 500 nm and the period of 1 $\mu$m fabricated into a silicon nitride membrane is shown in Fig. 5. The arrays were milled using $Ga^+$ ions with the energy of 30 keV using a medium ion beam current of $\sim$200 pA to avoid surface roughening and at the same time to keep short fabrication times.

## IV. CONCLUSIONS

Hollow targets have been proposed for enhanced acceleration of protons driven by high-power femtosecond laser pulses. We demonstrated by means of full 3D particle-in-cell simulations that the maximum energy of the accelerated protons can be increased by about 30% compared with ultrathin flat foil and with the so-called nanosphere targets. Moreover, the number of the accelerated high-energy protons from the hollow target is increased approximately by a factor of two compared with a flat foil of the same thickness. The enhanced proton acceleration is maintained with a larger incidence angle of the laser beam on the hollow target in contrast to the nanosphere target. The advantage of the hollow target is the possibility of its very low thickness and larger absorption of the laser pulse energy by the microstructured target at the same time. In addition, the fabrication of the first prototype of the hollow target by focused ion beam milling has been demonstrated.

## SUPPLEMENTARY MATERIAL

See supplementary material for the results of preliminary 2D simulations with a relief rectangular structure deposited on a 200 nm thick substrate.

## ACKNOWLEDGMENTS

This work has been mainly supported by the Czech Science Foundation, Project No. 15-02964S. Computational resources were provided in the frame of IT4Innovations Centre of Excellence project (CZ.1.05/1.1.00/02.0070), funded by the European Regional Development Fund and the national budget of the Czech Republic via the Research and Development for Innovations Operational Programme, as well as Czech Ministry of Education, Youth and Sports via the project Large Research, Development and Innovations Infrastructures (LM2011033). Access to the CERIT-SC computing and storage facilities provided by the CERIT-SC Center, provided under the programme "Projects of Large Research, Development, and Innovations Infrastructures" (CERIT Scientific Cloud LM2015085), is greatly appreciated. The results of this research have been also achieved using the DECI resource ARIS based in Greece at GRNET S.A. with support from the PRACE aisbl. Partial support by the project ELI - Extreme Light Infrastructure Phase 2 (CZ.02.1.01/0.0/0.0/15_008/0000162) through the European Regional Development Fund is also acknowledged.

[1] A. Macchi, M. Borghesi, and M. Passoni, Rev. Mod. Phys. **85**, 751 (2013).
[2] H. Daido, M. Nishiuchi, and A. S. Pirozhkov, Rep. Prog. Phys. **75**, 056401 (2012).
[3] S. Wilks, A. Langdon, T. Cowan, M. Roth, M. Singh, S. Hatchett, M. Key, D. Pennington, A. MacKinnon, and R. Snavely, Phys. Plasmas **8**, 542 (2001).
[4] A. Mackinnon, Y. Sentoku, P. Patel, D. Price, S. Hatchett, M. Key, C. Andersen, R. Snavely, and R. Freeman, Phys. Rev. Lett. **88**, 215006 (2002).
[5] T. Ceccotti, A. Levy, H. Popescu, F. Reau, P. D'Oliveira, P. Monot, J. P. Geindre, E. Lefebvre, and P. Martin, Phys. Rev. Lett. **99**, 185002 (2007).
[6] J. Fuchs, P. Antici, E. D'Humieres, E. Lefebvre, M. Borghesi, E. Brambrink, C. Cecchetti, M. Kaluza, V. Malka, M. Manclossi, S. Meyroneinc, P. Mora, J. Schreiber, T. Toncian, H. Pepin, and R. Audebert, Nat. Phys. **2**, 48 (2006).
[7] P. Gibbon, A. Andreev, E. Lefebvre, G. Bonnaud, H. Ruhl, J. Delettrez, and A. Bell, Phys. Plasmas **6**, 947 (1999).
[8] L. Cao, Y. Gu, Z. Zhao, L. Cao, W. Huang, W. Zhou, X. T. He, W. Yu, and M. Y. Yu, Phys. Plasmas **17**, 043103 (2010).
[9] O. Klimo, J. Psikal, J. Limpouch, J. Proska, F. Novotny, T. Ceccotti, V. Floquet, and S. Kawata, New J. Phys. **13**, 053028 (2011).
[10] A. Andreev, N. Kumar, K. Platonov, and A. Pukhov, Phys. Plasmas **18**, 103103 (2011).
[11] A. A. Andreev and K. Y. Platonov, Quantum Electron. **41**, 515 (2011).
[12] D. Margarone, O. Klimo, I. J. Kim, J. Prokupek, J. Limpouch, T. M. Jeong, T. Mocek, J. Psikal, H. T. Kim, J. Proska, K. H. Nam, L. Stolcova,

RIGHTSLINK

I. W. Choi, S. K. Lee, J. H. Sung, T. J. Yu, and G. Korn, Phys. Rev. Lett. **109**, 234801 (2012).

[13] D. Margarone, I. J. Kim, J. Psikal, J. Kaufman, T. Mocek, I. W. Choi, L. Stolcova, J. Proska, A. Choukourov, I. Melnichuk, O. Klimo, J. Limpouch, J. H. Sung, S. K. Lee, G. Korn, and T. M. Jeong, Phys. Rev. Spec. Top. Accel. Beams **18**, 071304 (2015).

[14] Y. Nodera, S. Kawata, N. Onuma, J. Limpouch, O. Klimo, and T. Kikuchi, Phys. Rev. E **78**, 046401 (2008).

[15] T. Nishikawa, H. Nakano, N. Uesugi, M. Nakao, and H. Masuda, Appl. Phys. Lett. **75**, 4079 (1999).

[16] U. Chakravarty, V. Arora, J. A. Chakera, P. A. Naik, H. Srivastava, P. Tiwari, A. Srivastava, and P. D. Gupta, J. Appl. Phys. **109**, 053301 (2011).

[17] T. Nishikawa, H. Nakano, K. Oguri, N. Uesugi, K. Nishio, and H. Masuda, J. Appl. Phys. **96**, 7537 (2004).

[18] T. D. Arber, K. Bennett, C. S. Brady, A. Lawrence-Douglas, M. G. Ramsay, N. J. Sircombe, P. Gillies, R. G. Evans, H. Schmitz, A. R. Bell, and C. P. Ridgers, Plasma Phys. Controlled Fusion **57**, 113001 (2015).

[19] J. Roden and S. Gedney, Micr. Opt. Tech. Lett. **27**, 334 (2000).

[20] I. J. Kim, K. H. Pae, I. W. Choi, C.-L. Lee, H. T. Kim, H. Singhal, J. H. Sung, S. K. Lee, H. W. Lee, P. V. Nickles, T. M. Jeong, C. M. Kim, and C. H. Nam, Phys. Plasmas **23**, 070701 (2016).

[21] R. A. Loch, T. Ceccotti, F. Quere, H. George, G. Bonnaud, F. Reau, P. D'Oliveira, M. J. H. Luttikhof, F. Bijkerk, K.-J. Boller, G. Blaclard, and P. Combis, Phys. Plasmas **23**, 093117 (2016).

[22] V. Floquet, O. Klimo, J. Psikal, A. Velyhan, J. Limpouch, J. Proska, F. Novotny, L. Stolcova, A. Macchi, A. Sgattoni, L. Vassura, L. Labate, F. Baffigi, L. A. Gizzi, P. Martin, and T. Ceccotti, J. Appl. Phys. **114**, 083305 (2013).

[23] A. Pukhov, Z. Sheng, and J. Meyer-ter Vehn, Phys. Plasmas **6**, 2847 (1999).

[24] L. Giuffrida, J. Psikal, K. Svensson, D. Margarone, C.-G. Wahlstrom, M. Dalui, P. Lutoslawski, I. Gallardo Gonzalez, V. Scuderi, G. Milluzzo, H. Ekerfelt, J. Kaufman, T. Wiste, A. Persson, J. Magnusson, A. Gonoskov, A. Picciotto, A. Bagolini, M. Crivellari, P. Bellutti, T. Lastovicka, G. A. P. Cirrone, O. Lundh, and G. Korn, "Manipulation of laser-accelerated proton beam profiles by nano- and micro-structured targets," Phys. Rev. Spec. Top. Accel. Beams (submitted).

[25] T. Morita, T. Z. Esirkepov, S. V. Bulanov, J. Koga, and M. Yamagiwa, Phys. Rev. Lett. **100**, 145001 (2008).

[26] N. Bassim, K. Scott, and L. A. Giannuzzi, MRS Bull. **39**, 317 (2014).

[27] L. A. Giannuzzi, *Introduction to Focused Ion Beams (Instrumentation, Theory, Techniques and Practice)* (Springer, USA, 2005).

[28] I. Utke, P. Hoffmann, and J. Melngailis, J. Vac. Sci. Technol., B **26**, 1197 (2008).

RIGHTSLINK

# Appendix C

# Paper 3

PHYSICS OF PLASMAS **21**, 073108 (2014)

# Increased efficiency of ion acceleration by using femtosecond laser pulses at higher harmonic frequency

J. Psikal,[1,a)] O. Klimo,[1,2] S. Weber,[2] and D. Margarone[2]
[1]*FNSPE, Czech Technical University in Prague, 11519 Prague, Czech Republic*
[2]*ELI-Beamlines Project, Institute of Physics of the ASCR, 18221 Prague, Czech Republic*

(Received 6 May 2014; accepted 15 July 2014; published online 28 July 2014)

The influence of laser frequency on laser-driven ion acceleration is investigated by means of two-dimensional particle-in-cell simulations. When ultrashort intense laser pulse at higher harmonic frequency irradiates a thin solid foil, the target may become re lativistically transparent for significantly lower laser pulse intensity compared with irradiation at fundamental laser frequency. The relativistically induced transparency results in an enhanced heating of hot electrons as well as increased maximum energies of accelerated ions and their numbers. Our simulation results have shown the increase in maximum proton energy and increase in the number of high-energy protons by a factor of 2 after the interaction of an ultrashort laser pulse of maximum intensity $7 \times 10^{21}\,\mathrm{W/cm^2}$ with a fully ionized plastic foil of realistic density and of optimal thickness between 100 nm and 200 nm when switching from the fundamental frequency to the third harmonics. *© 2014 AIP Publishing LLC.*
[http://dx.doi.org/10.1063/1.4891436]

## I. INTRODUCTION

The generation of highly energetic ion beams from laser-plasma interaction has attracted great interest in the last decade[1] due to the broad range of applications, including cancer therapy,[2] short-lived isotope production for medical applications,[3] isochoric heating of solid-density matter,[4] proton radiography,[5] and fast ignition in inertial confinement fusion.[6] Up to now, the highest energy ions (160 MeV for protons[7] and 1 GeV for carbon ions[8]) have been achieved with high energy (hundreds of Joules) and relatively long (0.5–1 ps) laser pulses on the Trident laser in the so-called Break Out Afterburner (BOA) regime.[9–12] Such source of high energy protons and ions is still not useful for societal applications because of the large size of currently used laser installations and the limited repetition rate. Nevertheless, smaller laser facilities, delivering a few tens of J and short laser pulses, which can in principle operate at 10 Hz repetition rate[13] are more promising.

The BOA regime, where the energy of accelerated protons is currently the highest in comparison with all other experimentally investigated regimes, relies on the fact that the laser pulse can burn through the target. In the experiments with longer and relatively high energy pulses, this is achieved naturally due to rapid expansion of the target heated by the first part of the laser pulse.[14,15] With shorter laser pulses, this can be however hardly achieved. In principle, one may use such an intense pulse that the target becomes relativistically transparent. However, such regime is not accessible at the moment. According to the estimate provided by Jung *et al.*[15] based on the previous model,[16] the onset of the relativistic transparency takes place at the time $t_1 = (12/\pi^2)^{1/4}\sqrt{(n_e/n_c)\tau d/(a_0 c_s)}$, where $n_e/n_c$ is the ratio of initial electron density to the critical electron density, $d$ is the target thickness, $a_0$ normalized laser amplitude, $\tau$ laser pulse duration at FWHM, and ion sound speed $c_s \approx \sqrt{Z m_e c^2 a_0/m_i}$. The lowest density compact solid matter, which is routinely available (plastic targets) has a free electron density of about $200\,n_c$ (for the wavelength of Ti:Sapphire laser equal to 800 nm), when fully ionized. Thus, we can estimate that, for example, for laser pulse duration (FWHM) of 20 fs and 200 nm thick plastic foil, laser intensity about $4 \times 10^{22}\,\mathrm{W/cm^2}$ is required to obtain relativistic transparency during laser-target interaction. Moreover, an ultraintense pulse works partially like a piston pushing a cloud of electrons ahead,[17] which further increases the required intensity for very short pulses.[18]

Nevertheless, there might be another approach how to make the target relativistically transparent than increasing laser pulse energy and the pulse length, converting the laser pulse to higher frequency. For example, since the critical electron density $n_c \sim \omega^2$, the same free electron density $n_e$ expressed in terms of critical density is reduced nine times (e.g., it is reduced to $\sim 20\,n_c$ for plastic foil) for the third harmonics compared with the fundamental frequency. Obviously, the parameter $a_0$ is also reduced but only three times for the third harmonics $(a_0 \sim \sqrt{I}/\omega)$.[19] Since the relativistically induced transparency takes place when $n_c \lesssim n_e \lesssim (1 + a_0^2/2)^{1/2} n_c$,[20,21] the intensity required for relativistic transparency can be significantly reduced. Namely, $(\frac{n_e}{10^{23}\,\mathrm{cm^{-3}}} \times \frac{\lambda}{\mu\mathrm{m}})^2 \lesssim \frac{I}{2.2{\cdot}10^{22}\,\mathrm{W/cm^{-2}}}$ is required for the target to be relativistically transparent assuming that $n_e > n_c$. Again, required laser intensity can be partially reduced by assuming target expansion,[15,16] which is important especially for longer laser pulses and for the similarity parameter[22] $S = n_e/(a_0 n_c) \gg 1$.

Obvious argument against this approach can be that conversion to the third harmonics costs a lot of energy. On the other hand, it is known that this conversion greatly improves the contrast of the laser pulse and not only in the nanosecond

---

[a)]jan.psikal@fjfi.cvut.cz

© 2014 AIP Publishing LLC

This article is copyrighted as indicated in the article. Reuse of AIP content is subject to the terms at: http://scitation.aip.org/termsconditions. Downloaded to IP: 147.32.25.202 On: Mon, 28 Jul 2014 13:15:48

domain but also in the picosecond domain.[23] Thus, the improvement of the laser pulse intensity contrast usually performed through the double plasma mirror technique,[24] which implies a similar energy loss, can be avoided in such case. Another clear argument can be that the electrons are less heated with lower $a_0$ and thus the proton energy should be smaller. However, we will demonstrate in this paper that such point of view does not apply here, because the regime of laser target interaction and proton acceleration is substantially different.

## II. COMPARISON OF ION ACCELERATION BY USING FUNDAMENTAL AND THE THIRD HARMONIC FREQUENCY

In order to show in more detail the mechanism which was discussed above, we have employed our 2D3V particle-in-cell (PIC) code[25] (with two spatial and three velocity components). In the simulations, we assumed the interaction of laser pulses with homogeneous fully ionized polyethylene $CH_2$ foils of the density $0.9\,g/cm^3$, where the free electron density is $n_e = 3.5 \times 10^{23}\,cm^{-3}$, at the wavelengths $\lambda_1 = 800\,nm$ corresponding to the fundamental frequency ($1\omega$) and $\lambda_3 = 264\,nm$ corresponding to the third harmonic frequency ($3\omega$). The electron density $n_e$ is equal to 200 $n_c$ and 21.8 $n_c$ for $1\omega$ and $3\omega$ cases, respectively. Ultrahigh laser pulse contrast is assumed, thus, all targets are initialized with step-like density profile. In order to prevent numerical heating,[26] the initial plasma temperature is set to 3 keV and the cell size is 8 nm. The laser pulse has $\sin^2$ temporal shape of full duration about 40 fs ($15\tau$ for $1\omega$ case and $45\tau$ for $3\omega$, where $\tau$ is the laser wave period). The peak intensity of linearly (p-)polarized pulse is set to $7.2 \times 10^{21}\,W/cm^2$ (dimensionless amplitudes $a_0 = 58$ and $a_0 = 19.1$ for $1\omega$ and $3\omega$ cases, respectively, where $I\lambda^2 = a_0^2 \times 1.37 \cdot 10^{18}$ $[W \cdot \mu m^2/cm^2]$). The focal spot diameter is set to $3\,\mu m$ at FWHM (Gaussian shape). The foils are irradiated at normal incidence since the acceleration of ions has been shown to be more efficient at normal than at oblique incidence for the laser pulse with the same parameters.[27]

Firstly, we illustrate the difference between using $1\omega$ and $3\omega$ pulses for the foil of thickness 200 nm. At $1\omega$ case ($\lambda_1 = 800\,nm$), most of the laser pulse is reflected from the target, but a small part is transmitted through the foil (with amplitude $a_0 \approx 5$). At $3\omega$ ($\lambda_3 = 264\,nm$), large part of the laser pulse is transmitted through the target (the foil is "punched through" before the end of the laser-target interaction) due to the induced transparency, see Fig. 1. Although $a_0$ is reduced almost three times by switching the laser frequency, the maximum proton energy in the forward direction is increased from 132 MeV at $1\omega$ case to 277 MeV at $3\omega$ case (see proton energy spectra in Fig. 2(a)). This strongly differs from the standard model of Target Normal Sheath Acceleration (TNSA) mechanism,[28] where the maximum ion energy is directly proportional to $\sim a_0$ by assuming ponderomotive scaling of hot electron temperature.[29] Moreover, the number of accelerated ions can be also substantially increased. For example, the number of protons with energy higher than 60 MeV already suitable for proton therapy applications is enhanced by factor 4 in $3\omega$ compared with $1\omega$ case for the used target thickness. Thus, two different ion acceleration regimes take place for the same foil thickness and laser pulse intensity, but at different laser frequencies. For $3\omega$ pulse, an enhanced ion acceleration connected with relativistic transparency, such as Laser BOA, should be operative.[15]

The enhancement of proton energy and number can be explained by a more efficient electron heating in $3\omega$ case due to relativistically induced transparency. When the target is relativistically transparent, electrons can be accelerated by the ponderomotive force in the whole target volume (given by the target thickness), whereas they are accelerated only in the surface layer determined by the skin depth for opaque targets. Therefore, the work done by the ponderomotive force on the electrons is higher for thicker relativistically transparent targets ($3\omega$ case) even if $a_0$ is smaller than for the opaque target ($1\omega$ case). In the energy spectra of electrons which are located behind the rear side of the foil (Fig. 2(b)), two distinct populations of hot electrons can be identified for $3\omega$, whereas only one population appears for $1\omega$ case. The first population can be approximated by $N_e \approx \exp(-E_k/T_h)$, where the hot electron temperature $T_h$ is about 4.6 MeV and 6.7 MeV in $1\omega$ and $3\omega$ case, respectively. Thus, one can observe that the temperature and number of hot electrons in the first population is enhanced for $3\omega$ (relativistically transparent) compared with $1\omega$ (nontransparent) case, which also corresponds to the increased absorption of laser pulse energy in the plasma (45% vs. 21% for $3\omega$ and $1\omega$, respectively). The high-energy tail in the spectrum for $3\omega$ case, which can be regarded as the second population of hot electrons, corresponds to the electron bunches directly accelerated by the propagating laser wave beyond the target similarly to the case of the so-called direct laser acceleration.[30]

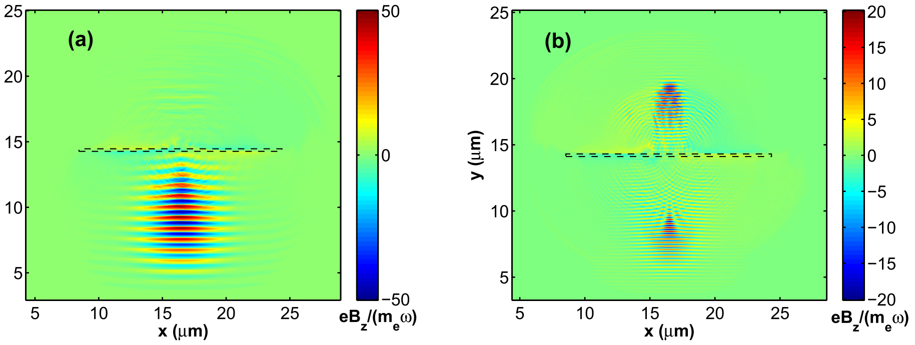

FIG. 1. Magnetic field $B_z$ in the simulation box showing reflected and transmitted part of the laser pulse after its interaction with 200 nm thick foil of electron density $3.5 \times 10^{23}\,cm^{-3}$ for (a) $1\omega$ and (b) $3\omega$ cases. Initial position of the foil is marked by the dashed line.

This article is copyrighted as indicated in the article. Reuse of AIP content is subject to the terms at: http://scitation.aip.org/termsconditions. Downloaded to IP: 147.32.25.202 On: Mon, 28 Jul 2014 13:15:48

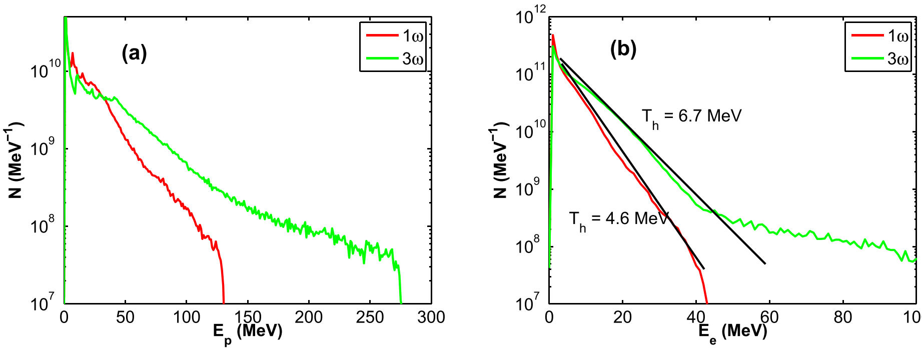

FIG. 2. Energy spectra of (a) accelerated protons in the forward direction at the end of simulations (approximately 100 fs after laser-foil interaction) and (b) heated electrons at the target rear (non-irradiated) side at the end of laser-target interaction for $1\omega$ and $3\omega$ cases and target thickness 200 nm. Hot electrons can be described by temperature $T_h$ except for high-energy tail at $3\omega$ case.

We should note that this mechanism works also when a small target preplasma at the front or rear side was assumed in the simulations instead of initial step-like density plasma profile. For example, when an exponential density profile $\exp(-x/L)$ with the scale length $L = 80$ nm was initialized and the thickness of the layer with constant maximum density was substantially reduced in order to keep the areal density of the target the same in the simulations, the maximum energy of accelerated protons only slightly differs (about 5% at most) for any combination of step-like and exponential density profiles on the target front/rear sides.

### A. Dependence on the target thickness

The efficiency of ion acceleration varies with the target thickness as shown in several experimental and theoretical studies.[31,32] Moreover, one may obtain induced transparency with thinner targets more easily,[9] especially when the target density is slightly above the threshold for induced transparency as in our case. Therefore, in the following set of simulations, we illustrate the difference between using $1\omega$ and $3\omega$ pulses for various thicknesses of plastic foils ranging from 20 nm to 1 $\mu$m. Fig. 3 shows the dependence of (a) maximum energies, (b) numbers of high-energy protons, and (c) maximum energies of $C^{6+}$ ions accelerated in the forward and backward directions (with respect to the propagation direction of the incident laser beam) as well as (d) the dependence of the ratio of the absorbed and transmitted laser pulse energy to the total laser beam energy on the foil thickness and laser frequency. The simulations show that a noticeable part of the laser pulse can propagate through the foil up to the thickness of 400 nm for $3\omega$, whereas the thickness less than 100 nm is required for $1\omega$ case. Note that the plasma skin depth $c/\omega_{pe}$,[19] where $\omega_{pe} \approx \sqrt{e^2 n_e/(\epsilon_0 \gamma_L m_e)}$ assuming relativistic mass of electrons oscillating in the linearly polarized laser field with relativistic factor $\gamma_L \approx \sqrt{1 + a_0^2/2}$, is about 60 nm and 35 nm for $1\omega$ and $3\omega$ case, respectively. Thus, the transmission of a substantial part of laser pulse energy through the foil could be explained by the thickness of the foil smaller than the skin depth for $1\omega$ case. On the contrary, only relativistically induced transparency is able to explain this effect for the foils thicker than 50 nm in the $3\omega$ case.

For laser frequency $3\omega$, the enhancement of maximum energy and the number of accelerated high-energy protons

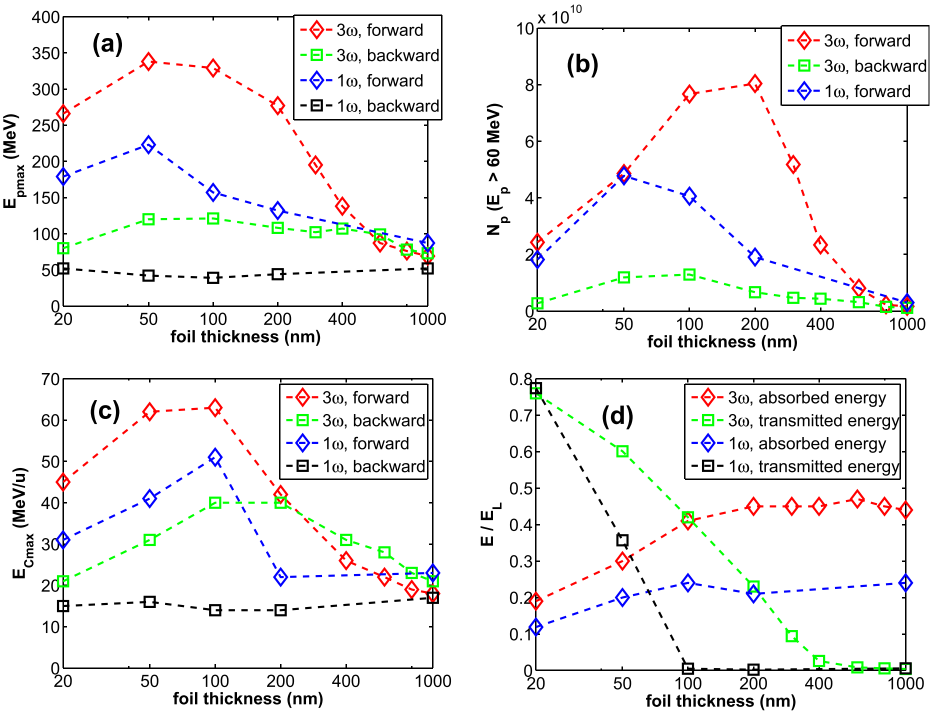

FIG. 3. Dependence of (a) maximum proton energy and (b) numbers of high energy protons (energy > 60 MeV), (c) maximum energy of $C^{6+}$ ions accelerated in the forward/backward direction on the thickness of ionized plastic foil ($CH_2$) irradiated by $1\omega$ and $3\omega$ laser pulse. (d) Dependence of the laser pulse energy transmitted through the foil and the absorbed energy in plasma on the foil thickness. The following thickness of the foil can be used in the simulations: 20 nm, 50 nm, 100 nm, 200 nm, 300 nm, 400 nm, 600 nm, 800 nm, 1 $\mu$m.

This article is copyrighted as indicated in the article. Reuse of AIP content is subject to the terms at: http://scitation.aip.org/termsconditions. Downloaded to IP: 147.32.25.202 On: Mon, 28 Jul 2014 13:15:48

roughly correlates with the amount of transmitted laser pulse energy and with the asymmetry of ion acceleration from the front and rear sides of the fully ionized polyethylene foils (in the backward and forward directions, respectively). Only 3% of the laser pulse energy incident on the target is transmitted through the foil in the case of 400 nm thickness. In fact, only a small rear part of the pulse propagates through with maximum amplitude $a_0 \approx 10$. The amount of transmitted laser pulse energy as well as the length of the transmitted part of the pulse (and its amplitude) significantly increases with decreasing thickness. For 300 nm thick foil, the amount of transmitted laser pulse energy reaches almost 10% of the incident energy and the maximum amplitude of the transmitted part of the pulse is $a_0 \approx 15$. For 50 nm foil, 60% of the pulse energy is transmitted and the maximum transmitted pulse amplitude is close to the amplitude of the incident laser pulse. However, the amount of the absorbed energy in the plasma is reduced for the thinnest foils as the density of the expanding foil decreases rapidly already during laser-target interaction. Reduced laser pulse absorption and relatively low number of particles in the laser focal spot lead to the decrease in the number of high-energy protons even if the maximum energy only slightly falls for the thinnest foils.

At fundamental laser frequency, the enhancement of proton energy and number can be also observed with decreasing target thickness. However, such enhancement is less pronounced than for the third harmonic frequency. The increase in maximum energy for the foil of thickness 200 nm compared with 1 $\mu$m about 50% in the forward direction is in qualitative agreement with previous experimental observations at significantly lower maximum intensity of the pulse ($\sim 10^{19}$ W/cm$^2$).[31] The most efficient proton acceleration takes place at the foil thickness 50 nm when the foil becomes transparent already during laser-target interaction due to its rapid expansion. In $3\omega$ case, the highest proton energy can be also observed for 50 nm foil. Nevertheless, the optimum thickness for $3\omega$ is between 100 nm and 200 nm, since there is a clear maximum of the number of high-energy protons, whereas the maximum energy is only slightly lower compared with 50 nm foil.

When a part of the laser pulse is transmitted through the foil, one can observe a strong asymmetry in terms of maximum energy of accelerated ions in the forward/backward direction (Fig. 3(a)). We observed this asymmetry when the transmitted part has amplitude $a_0 \gg 1$ (when the $v \times B$ term in the Lorentz force becomes significant as the electric term). At amplitude $a_0 \gg 1$, electrons oscillating in the laser wave have relativistic quiver velocity,[19] their trajectories can be bent by the magnetic field of the wave towards laser propagation direction and their energy is enhanced. Such increase in electron energy is translated into fast ions. The transmitted laser wave with amplitude $a_0 \gg 1$ is observed in our simulations only for targets with thickness equal or less than 400 nm at $3\omega$ case, whereas it is observed for all studied foils at $1\omega$ (even if the amount of transmitted laser pulse energy is below 1% for the foils thicker than 50 nm).

The dependence of maximum energy on the foil thickness is quite similar for heavier $C^{6+}$ ions (see Fig. 3(c)). Since the protons from target surface layer are accelerated prior to heavier ions due to their higher charge to mass ratio, the protons partly shield accelerating electric field for $C^{6+}$ ions. Therefore, the maximum energy of $C^{6+}$ ions per atomic mass unit is reduced on 20%–40% of the energy of protons. One can also observe that the ratio of the energy of $C^{6+}$ ions accelerated in the backward direction to the energy of the ions accelerated in the forward direction is slightly enhanced compared with protons. The difference can be ascribed to acceleration of protons prior carbon ions towards target interior from the front (laser-irradiated) side due to radiation pressure in the initial stage of interaction, which subsequently leads to a relatively small amount of light ions (protons) on the target front surface compared with the amount of heavier ions. After laser-target interaction, a significantly lower number of protons on the front target side shields the accelerating electric field on carbon ions less than on the rear target side.

### B. Dependence on the target density at $3\omega$ case

In the simulations described above, the target density was fixed at $n_e = 3.5 \times 10^{23}$ cm$^{-3}$, which is a realistic density for fully ionized polyethylene $CH_2$ foil. However, this density was slightly above theoretical threshold for the induced transparency for a given laser pulse amplitude. Therefore, in the second set of simulations, we investigated the using of the third harmonic frequency for various target densities (from $4.375 \times 10^{22}$ cm$^{-3}$ to $7.0 \times 10^{23}$ cm$^{-3}$) with fixed thickness of the foil equal to 200 nm. Other parameters have been kept the same as in previous simulations.

One can observe similarly to previous set of simulations that the ion acceleration is enhanced in the forward direction when a part of the pulse is transmitted and, simultaneously, when it has a larger amplitude ($a_0 \gg 1$) after propagation through the target. For electron density $n_e = 3.5 \times 10^{23}$ cm$^{-3}$, the maximum energy of accelerated protons is equal to 277 MeV, whereas it is only 108 MeV in the backward direction (see Fig. 4(a)). When we increase the target density by factor 2 up to $n_e = 7.0 \times 10^{23}$ cm$^{-3}$, the laser pulse is not transmitted substantially through the target (electromagnetic wave with amplitude $a_0 \approx 1$ propagates behind the target) and the maximum energy of protons accelerated in the forward and backward directions is almost the same $-119$ MeV and 109 MeV, respectively (but the number of accelerated protons is substantially higher in the forward direction). On the contrary, when the density of the foil is twice or even four times decreased, proton energy in the forward direction increases further about 20% or 30%, respectively. Then, the energy starts to decrease with the density. In the backward direction, the energy is constant except for the lowest density case $n_e = 4.375 \times 10^{22}$ cm$^{-3}$, where it decreases about 20%. Thus, we found the maximum energy of accelerated protons for electron density of the foil $n_e = 8.75 \times 10^{22}$ cm$^{-3}$ ($\approx 5.4\ n_c$ for $3\omega$). However, for another important parameter—the number of high energy protons (with energy higher than 60 MeV suitable for proton therapy), optimal target density between $1.75 \times 10^{23}$ and $3.5 \times 10^{23}$ cm$^{-3}$ ($\approx 10.9\ n_c$ and $21.8\ n_c$ for $3\omega$, respectively), was found in our simulations as can be seen in Fig. 4(b). It corresponds to the highest absorption of laser

This article is copyrighted as indicated in the article. Reuse of AIP content is subject to the terms at: http://scitation.aip.org/termsconditions. Downloaded to IP: 147.32.25.202 On: Mon, 28 Jul 2014 13:15:48

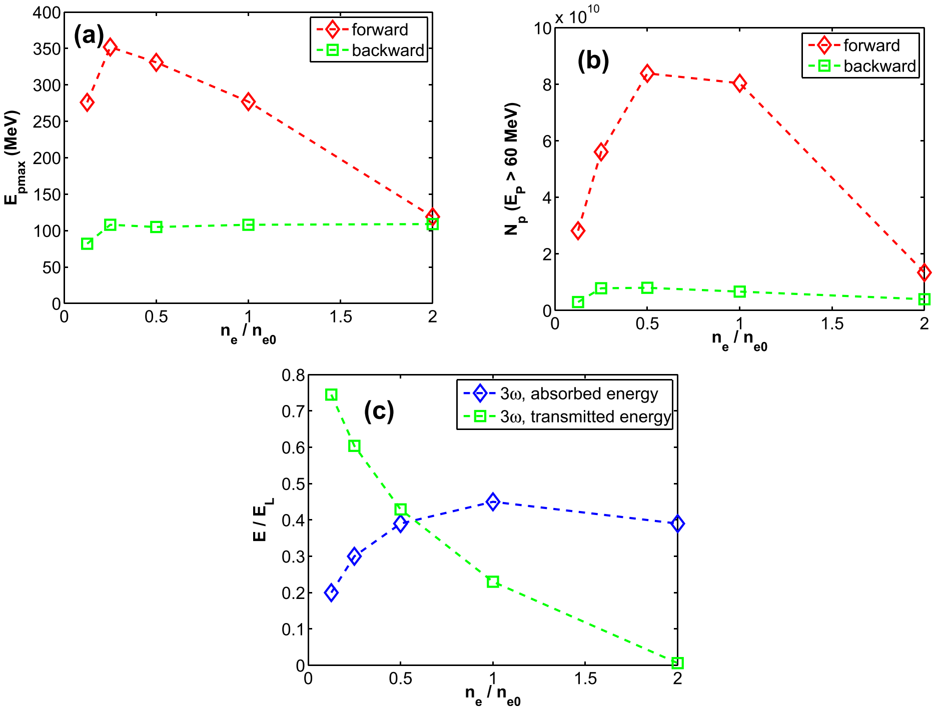

FIG. 4. Dependence of (a) maximum proton energy and (b) numbers of high energy protons (energy > 60 MeV) accelerated in the forward/backward direction, (c) laser pulse energy transmitted through the foil and the absorbed energy in plasma on the density of 200 nm thick ionized plastic foil (CH$_2$) irradiated by $3\omega$ laser pulse. Initial target density is normalized to the electron density $n_{e0} = 3.5 \times 10^{23}\,\mathrm{cm}^{-3}$, which is the density used in previous set of simulations.

pulse energy into the plasma (39% and 45%, respectively). We should note that it does not mean optimal values for all laser and target parameters. The investigation of such dependency on various laser and target parameters is beyond the scope of this paper. For example, one may suppose that the using of the 4th harmonics may be more beneficial when the target of higher density (e.g., metal foils) would be assumed.

## III. CONCLUSION

In conclusion, we have proposed a significant enhancement of ion acceleration from ionized solid target by using ultrashort intense (subPW) laser pulse at higher harmonic frequency. In our numerical simulations, we have demonstrated the increase in maximum proton energy as well as the increase in the number of high-energy protons suitable for proton therapy by factor 2 by using the third harmonic frequency compared with fundamental frequency at optimal thickness of ionized plastic foil. Higher energies and numbers of accelerated ions are explained by a more efficient electron heating and acceleration by the ponderomotive force in the whole target volume (given by the target thickness) when the target is relativistically transparent. Since the laser intensity required for relativistically induced transparency is directly proportional to $\lambda^2 \sim 1/\omega^2$ (where $\lambda$ is the laser wavelength and $\omega$ is the frequency), this regime is achievable more easily with higher (harmonic) laser frequency than the fundamental one.

Such strong enhancement of ion acceleration can surpass other enhancements which propose to use special targets like the ones with microstructures,[33–35] foam,[36] or grating[37] on the surface. Moreover, flat foil targets can be more easily produced than other special targets, which is important from the point of view of future applications of high repetition rate femtosecond lasers.

## ACKNOWLEDGMENTS

This research has been supported by the Czech Science Foundation (Project No. P205/12/P366) and by the Ministry of Education, Youth and Sports of the Czech Republic under projects ELI-Beamlines (CZ.1.05/1.1.00/02.0061), ECOP (CZ.1.07/2.3.00/20.0087). The authors would like to acknowledge IT4Innovations Centre of Excellence project (CZ.1.05/1.1.00/02.0070) funded by the European Regional Development Fund as well as Large Research, Development and Innovation Infrastructures project (LM2011033) funded by the Ministry of Education, Youth and Sports of the Czech Republic for providing computing resources. Also, access to computing and storage facilities owned by parties and projects contributing to the National Grid Infrastructure MetaCentrum, provided under the programme Projects of Large Infrastructure for Research, Development, and Innovations (LM2010005), is greatly appreciated.

[1] A. Macchi, M. Borghesi, and M. Passoni, Rev. Mod. Phys. **85**, 751 (2013).
[2] G. A. P. Cirrone, M. Carpinelli, G. Cuttone, S. Gammino, S. B. Jia, G. Korn, M. Maggiore, L. Manti, D. Margarone, J. Prokupek, M. Renis, F. Romano, F. Schillaci, B. Tomasello, L. Torrisi, A. Tramontana, and A. Velyhan, Nucl. Instrum. Methods Phys. Res. A **730**, 174 (2013).
[3] K. W. D. Ledingham and W. Galster, New J. Phys. **12**, 045005 (2010).
[4] R. A. Snavely, B. Zhang, K. Akli, Z. Chen, R. R. Freeman, P. Gu, S. P. Hatchett, D. Hey, J. Hill, M. H. Key, Y. Izawa, J. King, Y. Kitagawa, R. Kodama, A. B. Langdon, B. F. Lasinski, A. Lei, A. J. MacKinnon, P. Patel, R. Stephens, M. Tampo, K. A. Tanaka, R. Town, Y. Toyama, T. Tsutsumi, S. C. Wilks, T. Yabuuchi, and J. Zheng, Phys. Plasmas **14**, 092703 (2007).
[5] M. Borghesi, A. Mackinnon, D. Campbell, D. Hicks, S. Kar, P. Patel, D. Price, L. Romagnani, A. Schiavi, and O. Willi, Phys. Rev. Lett. **92**, 055003 (2004).

This article is copyrighted as indicated in the article. Reuse of AIP content is subject to the terms at: http://scitation.aip.org/termsconditions. Downloaded to IP: 147.32.25.202 On: Mon, 28 Jul 2014 13:15:48

[6] M. Roth, T. Cowan, M. Key, S. Hatchett, C. Brown, W. Fountain, J. Johnson, D. Pennington, R. Snavely, S. Wilks, K. Yasuike, H. Ruhl, F. Pegoraro, S. Bulanov, E. Campbell, M. Perry, and H. Powell, Phys. Rev. Lett. **86**, 436 (2001).

[7] B. M. Hegelich, D. Jung, B. J. Albright, M. Cheung, B. Dromey, D. C. Gautier, C. Hamilton, S. Letzring, R. Munchhausen, S. Palaniyappan, R. Shah, H.-C. Wu, L. Yin, and J. C. Fernández, "160 MeV laser-accelerated protons from CH2 nanotargets for proton cancer therapy," e-print arXiv:1310.8650 (2013).

[8] D. Jung, L. Yin, D. C. Gautier, H. C. Wu, S. Letzring, B. Dromey, R. Shah, S. Palaniyappan, T. Shimada, R. P. Johnson, J. Schreiber, D. Habs, J. C. Fernandez, B. M. Hegelich, and B. J. Albright, Phys. Plasmas **20**, 083103 (2013).

[9] L. Yin, B. J. Albright, B. M. Hegelich, and J. C. Fernandez, Laser Part. Beams **24**, 291 (2006).

[10] B. J. Albright, L. Yin, K. J. Bowers, B. M. Hegelich, K. A. Flippo, T. J. T. Kwan, and J. C. Fernandez, Phys. Plasmas **14**, 094502 (2007).

[11] L. Yin, B. J. Albright, B. M. Hegelich, K. J. Bowers, K. A. Flippo, T. J. T. Kwan, and J. C. Fernandez, Phys. Plasmas **14**, 056706 (2007).

[12] L. Yin, B. J. Albright, K. J. Bowers, D. Jung, J. C. Fernandez, and B. M. Hegelich, Phys. Rev. Lett. **107**, 045003 (2011).

[13] B. Rus, P. Bakule, D. Kramer, G. Korn, J. T. Green, J. Novak, M. Fibrich, F. Batysta, J. Thoma, J. Naylon, T. Mazanec, M. Vitek, R. Barros, E. Koutris, J. Hrebicek, J. Polan, R. Base, P. Homer, M. Koselja, T. Havlicek, A. Honsa, M. Novak, C. Zervos, P. Korous, M. Laub, and J. Houzvicka, *High-Power, High-Energy, and High-Intensity Laser Technology; and Research Using Extreme Light: Entering New Frontiers With Petawatt-Class Lasers*, Proceedings of SPIE Vol. 8780, edited by J. Hein, G. Korn, and L. Silva (SPIE, 2013) p. 87801T.

[14] B. M. Hegelich, I. Pomerantz, L. Yin, H. C. Wu, D. Jung, B. J. Albright, D. C. Gautier, S. Letzring, S. Palaniyappan, R. Shah, K. Allinger, R. Hoerlein, J. Schreiber, D. Habs, J. Blakeney, G. Dyer, L. Fuller, E. Gaul, E. Mccary, A. R. Meadows, C. Wang, T. Ditmire, and J. C. Fernandez, New J. Phys. **15**, 085015 (2013).

[15] D. Jung, L. Yin, B. J. Albright, D. C. Gautier, S. Letzring, B. Dromey, M. Yeung, R. Hoerlein, R. Shah, S. Palaniyappan, K. Allinger, J. Schreiber, K. J. Bowers, H.-C. Wu, J. C. Fernandez, D. Habs, and B. M. Hegelich, New J. Phys. **15**, 023007 (2013).

[16] X. Q. Yan, T. Tajima, M. Hegelich, L. Yin, and D. Habs, Appl. Phys. B **98**, 711 (2010).

[17] Y. Sentoku, T. Cowan, A. Kemp, and H. Ruhl, Phys. Plasmas **10**, 2009 (2003).

[18] B. Qiao, S. Kar, M. Geissler, P. Gibbon, M. Zepf, and M. Borghesi, Phys. Rev. Lett. **108**, 115002 (2012).

[19] P. Gibbon, *Short Pulse Laser Interactions With Matter: An Introduction* (Imperial College Press, 2005).

[20] E. Lefebvre and G. Bonnaud, Phys. Rev. Lett. **74**, 2002 (1995).

[21] H. Sakagami and K. Mima, Phys. Rev. E **54**, 1870 (1996).

[22] S. Gordienko and A. Pukhov, Phys. Plasmas **12**, 043109 (2005).

[23] D. Hillier, C. Danson, S. Duffield, D. Egan, S. Elsmere, M. Girling, E. Harvey, N. Hopps, M. Norman, S. Parker, P. Treadwell, D. Winter, and T. Bett, Appl. Opt. **52**, 4258 (2013).

[24] C. Thaury, F. Quere, J.-P. Geindre, A. Levy, T. Ceccotti, P. Monot, M. Bougeard, F. Reau, P. D'Oliveira, P. Audebert, R. Marjoribanks, and P. H. Martin, Nat. Phys. **3**, 424 (2007).

[25] J. Psikal, J. Limpouch, S. Kawata, and A. A. Andreev, Czech. J. Phys. **56**, B515 (2006).

[26] H. Ueda, Y. Omura, H. Matsumoto, and T. Okuzawa, Comput. Phys. Commun. **79**, 249 (1994).

[27] J. Limpouch, J. Psikal, O. Klimo, J. Vyskocil, J. Proska, F. Novotny, L. Stolcova, and M. Kveton, *High-Power, High-Energy, and High-Intensity Laser Technology; and Research Using Extreme Light: Entering NEW Frontiers With Petawatt-Class Lasers*, Proceedings of SPIE Vol. 8780, edited by J. Hein, G. Korn, and L. Silva (SPIE, 2013) p. 878027.

[28] R. Snavely, M. Key, S. Hatchett, T. Cowan, M. Roth, T. Phillips, M. Stoyer, E. Henry, T. Sangster, M. Singh, S. Wilks, A. MacKinnon, A. Offenberger, D. Pennington, K. Yasuike, A. Langdon, B. Lasinski, J. Johnson, M. Perry, and E. Campbell, Phys. Rev. Lett. **85**, 2945 (2000).

[29] S. Wilks, A. Langdon, T. Cowan, M. Roth, M. Singh, S. Hatchett, M. Key, D. Pennington, A. MacKinnon, and R. Snavely, Phys. Plasmas **8**, 542 (2001).

[30] A. Pukhov, Z. Sheng, and J. Meyer-ter Vehn, Phys. Plasmas **6**, 2847 (1999).

[31] D. Neely, P. Foster, A. Robinson, F. Lindau, O. Lundh, A. Persson, C. G. Wahlstrom, and P. McKenna, Appl. Phys. Lett. **89**, 021502 (2006).

[32] T. Ceccotti, A. Levy, H. Popescu, F. Reau, P. D'Oliveira, P. Monot, J. P. Geindre, E. Lefebvre, and P. Martin, Phys. Rev. Lett. **99**, 185002 (2007).

[33] O. Klimo, J. Psikal, J. Limpouch, J. Proska, F. Novotny, T. Ceccotti, V. Floquet, and S. Kawata, New J. Phys. **13**, 053028 (2011).

[34] D. Margarone, O. Klimo, I. J. Kim, J. Prokupek, J. Limpouch, T. M. Jeong, T. Mocek, J. Psikal, H. T. Kim, J. Proska, K. H. Nam, L. Stolcova, I. W. Choi, S. K. Lee, J. H. Sung, T. J. Yu, and G. Korn, Phys. Rev. Lett. **109**, 234801 (2012).

[35] V. Floquet, O. Klimo, J. Psikal, A. Velyhan, J. Limpouch, J. Proska, F. Novotny, L. Stolcova, A. Macchi, A. Sgattoni, L. Vassura, L. Labate, F. Baffigi, L. A. Gizzi, P. Martin, and T. Ceccotti, J. Appl. Phys. **114**, 083305 (2013).

[36] A. Sgattoni, P. Londrillo, A. Macchi, and M. Passoni, Phys. Rev. E **85**, 036405 (2012).

[37] T. Ceccotti, V. Floquet, A. Sgattoni, A. Bigongiari, O. Klimo, M. Raynaud, C. Riconda, A. Heron, F. Baffigi, L. Labate, L. A. Gizzi, L. Vassura, J. Fuchs, M. Passoni, M. Kveton, F. Novotny, M. Possolt, J. Prokupek, J. Proska, J. Psikal, L. Stolcova, A. Velyhan, M. Bougeard, P. D'Oliveira, O. Tcherbakoff, F. Reau, P. Martin, and A. Macchi, Phys. Rev. Lett. **111**, 185001 (2013).

This article is copyrighted as indicated in the article. Reuse of AIP content is subject to the terms at: http://scitation.aip.org/termsconditions. Downloaded to IP: 147.32.25.202 On: Mon, 28 Jul 2014 13:15:48

Appendix D

# Paper 4

This paper is protected by publisher's Copyright which does not enable to include it in the university's electronic repository. You can download it from the web site of publisher.

# Appendix E

# Paper 5

This paper is protected by publisher's Copyright which does not enable to include it in the university's electronic repository. You can download it from the web site of publisher.

# Appendix F

# Paper 6

# Manipulation of laser-accelerated proton beam profiles by nanostructured and microstructured targets

L. Giuffrida,[1*] K. Svensson,[2] J. Psikal,[1,3] M. Dalui,[2] H. Ekerfelt,[2] I. Gallardo Gonzalez,[2]
O. Lundh,[2] A. Persson,[2] P. Lutoslawski,[1] V. Scuderi,[1,4] J. Kaufman,[1] T. Wiste,[1] T. Lastovicka,[1]
A. Picciotto,[5] A. Bagolini,[5] M. Crivellari,[5] P. Bellutti,[5] G. Milluzzo,[4] G. A. P. Cirrone,[4]
J. Magnusson,[6] A. Gonoskov,[6] G. Korn,[1] C-G. Wahlström,[2] and D. Margarone[1]

[1]*Institute of Physics ASCR, v.v.i (FZU), ELI-Beamlines project, 182 21 Prague, Czech Republic*
[2]*Department of Physics, Lund University, P.O. Box 118, S-221 00 Lund, Sweden*
[3]*FNSPE, Czech Technical University in Prague, 11519 Prague, Czech Republic*
[4]*Laboratory Nazionali del Sud, INFN, 95125 Catania, Italy*
[5]*Micro-Nano Facility, Fondazione Bruno Kessler, 38123 Trento, Italy*
[6]*Department of Physics, Chalmers University of Technology, 41296 Gothenburg, Sweden*

(Received 9 December 2016; published 4 August 2017)

Nanostructured and microstructured thin foils have been fabricated and used experimentally as targets to manipulate the spatial profile of proton bunches accelerated through the interaction with high intensity laser pulses ($6 \times 10^{19}$ W/cm$^2$). Monolayers of polystyrene nanospheres were placed on the rear surfaces of thin plastic targets to improve the spatial homogeneity of the accelerated proton beams. Moreover, thin targets with grating structures of various configurations on their rear sides were used to modify the proton beam divergence. Experimental results are presented, discussed, and supported by 3D particle-in-cell numerical simulations.

DOI: 10.1103/PhysRevAccelBeams.20.081301

## I. INTRODUCTION

Table-top laser systems, using the chirped-pulse amplification (CPA) technique, which were developed in the last decades, are able to reach ultrahigh intensities (above $10^{18}$ W/cm$^2$) through the generation of femtosecond laser pulses [1], thus offering new possibilities in the study of relativistic laser-matter interactions [2,3]. Among others, laser-driven ion acceleration is one of the most promising and intensively investigated research topics [4], where target normal sheath acceleration (TNSA) is the experimentally most investigated technique. TNSA is based on the relativistic interaction of a thin target and an intense laser pulse and can be used to accelerate protons to several tens of MeV [5–8]. The front surface of the target is ionized by the leading edge of the laser pulse, creating a plasma expanding from the target front. A significant part of the laser pulse energy is absorbed and heats the plasma electrons which subsequently propagate through the target. As these hot electrons exit the rear of the target, they set up very strong electrostatic sheath fields that ionize atoms and molecules present on the target rear surface. Positively charged particles can subsequently be accelerated in these sheath fields in the target normal direction. It is the particles with the highest charge-to-mass ratio that are preferentially accelerated, which, under the present experimental conditions, are protons.

The energy of the accelerated protons depends on the strength of the sheath fields, which in turn scales with the hot electron temperature, and therefore the fraction of absorbed laser energy. It is thus possible to increase the proton energies by enhancing the absorption of laser energy at the front of the target. It has also been shown that the spatial divergence of the emitted protons is energy dependent, which is a consequence of the initial electron sheath shape on the rear of the target, such that the divergence increases with decreasing proton energy [9]. The beams of accelerated protons present unique characteristics, e.g. short bunch duration at the source (~ps) [10], low transverse emittance (few $10^{-3}$ mm mrad [11]), and ultrahigh dose rate (~$10^9$ Gy/s) [12], which make them potentially very attractive for multidisciplinary applications, such as radiation biology [13], hadron therapy [14], proton radiography [15,16], and fast ignition [17].

In previous works, it was demonstrated experimentally that nanospheres deposited on the target front surface can increase the temperature and the distribution of hot electrons generated during relativistic intensity laser-solid interaction and, as a consequence, enhance the energy and number of accelerated protons, as well as the spatial homogeneity of the beam [18]. It has also been shown that it is possible to enhance the maximum energy of

---

[*] Corresponding author.
Lorenzo.Giuffrida@eli-beams.eu

*Published by the American Physical Society under the terms of the Creative Commons Attribution 4.0 International license. Further distribution of this work must maintain attribution to the author(s) and the published article's title, journal citation, and DOI.*

laser-accelerated protons by introducing grating microstructures on the target front surface [19].

We have extended these previous investigations by a study where the spatial profile of the proton beam is manipulated, both in terms of divergence and spatial homogeneity, by introducing nanospheres or $\mu$m-sized grating structures on the rear side of the target. The reported experimental results are supported by 3D particle-in-cell (PIC) numerical simulations.

## II. EXPERIMENTAL SETUP

### A. Laser system and pulse focusing

The multiterawatt laser in the Lund University is a CPA based Ti:sapphire system with a central wavelength of 800 nm, capable of delivering approximately 2 J of energy per pulse (uncompressed) at 10 Hz repetition rate. The typical pulse duration after compression is 35 fs with an amplified spontaneous emission pedestal having an intensity ratio of approximately $10^{-9}$, measured 120 ps prior to the main pulse. A deformable mirror is placed after the laser pulse compressor to correct wavefront aberrations up to, and including the $f/3$ off-axis parabolic focusing mirror (OAP). The measured laser energy delivered into the target chamber was approximately 1 J per pulse during the present experimental study. The full width at half maximum of the laser focal spot was measured to be approximately 3.5 $\mu$m. After the OAP, but prior to the laser focus, a plasma mirror (PM), placed at Brewster's angle, was used to further improve the temporal contrast on the target. In the current experiment, the reflectivity of the plasma mirror was measured to be $(47 \pm 4)\%$ with an estimated temporal contrast ratio enhancement of 2 orders of magnitude [20].

After the PM, the p-polarized laser pulse was focused on target with an incidence angle of 45° relative to the target normal. The laser peak intensity, in vacuum, was determined from the above-mentioned total pulse energy (after the PM), the measured pulse duration, and a recorded high dynamic-range image of the spatial intensity distribution in the focal plane. This results in a peak intensity of about $6 \times 10^{19}$ W/cm$^2$, neglecting any changes to the laser spot size introduced by the PM. A sketch of the setup is shown in Fig. 1(a).

### B. Targets

Targets used during this experimental campaign are sketched in Figs. 1(b) and 1(c). Plastic (Mylar™) foils of 500 nm thickness, covered with monolayers of polystyrene nanospheres of 400 nm diameter, were produced using the technique described in [21] at the ELI Beamlines target laboratory. Flat plastic foils of 900 nm thickness, i.e. the same overall thickness as of the nanosphere-covered targets, were used for comparison. Free-standing silicon nitride (SiN) membranes of 700 nm thickness, developed and fabricated at Fondazione Bruno Kessler, were also used in the experiment. The SiN membranes were deposited by a plasma enhanced chemical vapor deposition reactor and

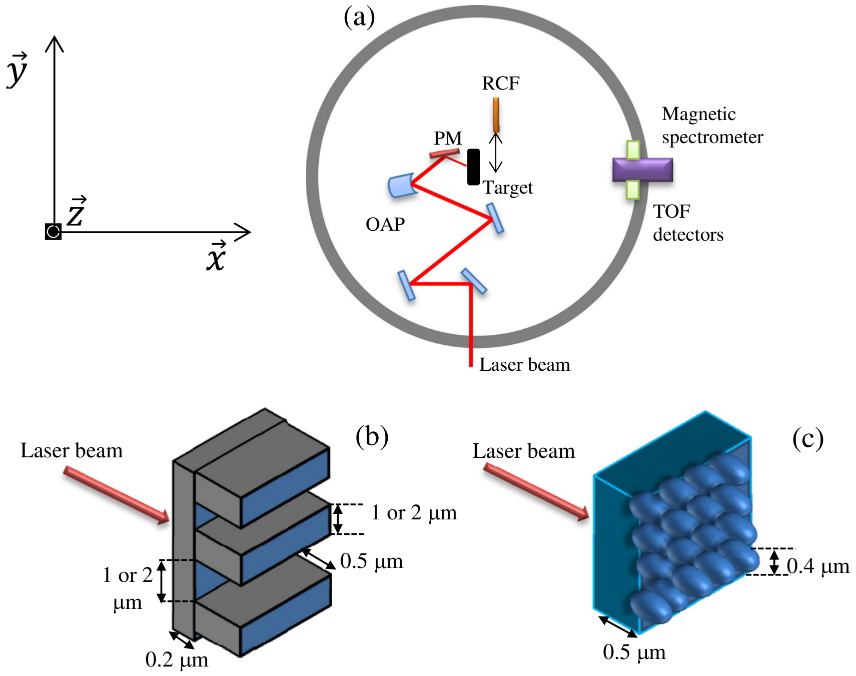

FIG. 1. Top view of the experimental setup (a), sketch showing the plastic target covered with nanospheres (b), and side view of the grating targets (c) used in the experiment. Here $\vec{x}$ is the axis normal to the target surface, $\vec{y}$ is the direction perpendicular to the orientation of grating ridges and $\vec{z}$ is the direction parallel to the orientation of horizontal grating ridges.

defined by a chemical etching of the silicon wafer on their rear. Various grating structures, with different periodicities, were shaped on the SiN membranes. The ridges had widths of $(0.5 \pm 0.1)$ $\mu$m, while the grooves between them were $(0.5 \pm 0.1)$ $\mu$m deep and $(1 \pm 0.1)$ $\mu$m or $(2 \pm 0.2)$ $\mu$m wide.

### C. Proton diagnostics

Various detectors were employed to characterize the beams of laser-accelerated protons. A hyperpure $4.4 \times 4.5\ \mathrm{mm}^2$, 500 $\mu$m thick, single crystal diamond detector (SCDD) was placed behind the target at a distance of 56 cm and an angle of 9° with respect to the target normal. This detector was used in time-of-flight (TOF) configuration, which allows the energy spectrum of the accelerated proton beam to be indirectly determined. A picture of the used detector and its electric scheme are reported in Figs. 2(a) and 2(b), respectively. A magnetic spectrometer placed behind the target in the target normal direction was also used to retrieve proton energy spectra [a sketch is reported in Fig. 2(c)]. This spectrometer consists of a 1 mm entrance slit in front of a 5 cm permanent dipole magnet with 0.83 T mean field strength, deflecting protons according to their energies. Protons are then stopped in a plastic scintillator (Saint Gobain, BC-408 [22]) and the resulting fluorescence is imaged by a 16-bit electron multiplying charged coupled device camera. The scintillator is covered with a 6 $\mu$m thick aluminum foil, which shields it from scattered laser light and optical radiation from the plasma. This foil also stops any low-energy ions of higher nuclear charge, such as carbon, oxygen, or silicon, due to its much higher stopping power for such ions compared to protons. Thanks to this foil, in combination with the energy, mass, and charge dependent dispersion in the magnetic field, as well as the nuclear charge dependent scintillator response, which is much lower for higher nuclear charge ions compared to protons, the observed signal becomes dominated by the contribution from accelerated protons only in the regime investigated in the present study. Finally, radiochromic film (RCF) stacks composed of a few layers of HD-V2 RCF type were used to characterize divergence and spatial uniformity of the accelerated proton beams. The RCF stacks were placed 6 cm behind the target in the target normal direction. The RCF stacks were covered by 2.4 $\mu$m Al filter, in order to cut the protons with less than 275 keV and the visible/UV radiation coming out from the plasma after the laser-target interaction. The positions of the detectors were such that it was not possible to obtain simultaneous information on the spatial profiles and on the energy distribution of the accelerated protons.

## III. EXPERIMENTAL RESULTS

Plastic (Mylar or polyethylene terephthalate) foils of 900 nm thickness (PET) were used as reference targets in terms of accelerated proton beam features in the standard TNSA regime [5–8]. Results obtained with such targets were compared with the ones of proton beams generated from Mylar foils covered with nanospheres on the substrate

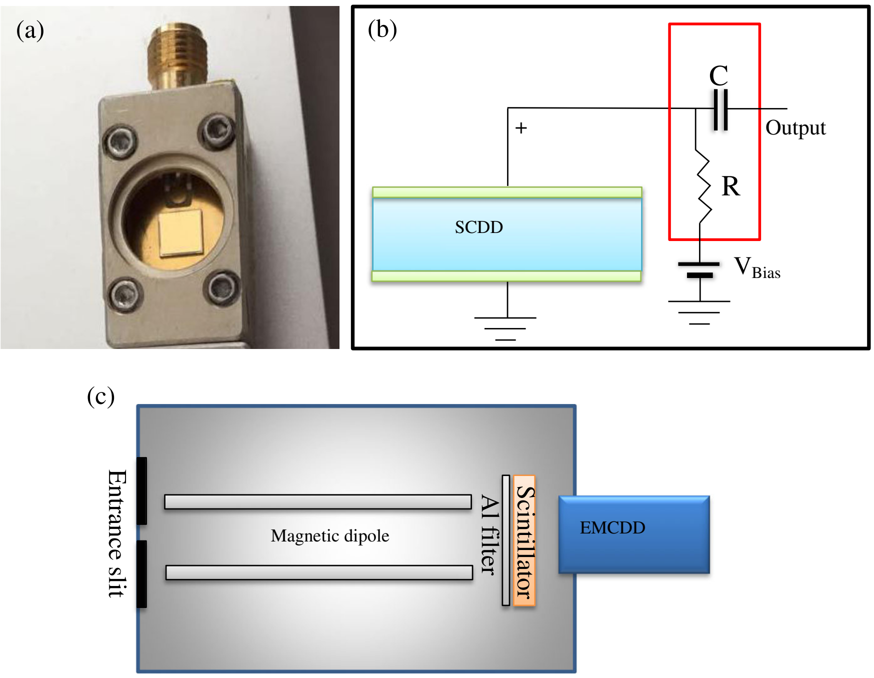

FIG. 2. Photo (a) and electrical scheme (b) of the SCDD detector, and sketch of the magnetic spectrometer (c) used during the experiment.

rear side (NS$_{\rm rear}$). Moreover, targets made of SiN membrane with a thickness of 200 nm (SiN) were used as reference, and targets with gratings on the rear side with a step of 1 $\mu$m (SiN$_{1\,\mu\rm m}$) and 2 $\mu$m (SiN$_{2\,\mu\rm m}$) were also used.

Figure 3 reports energy distributions obtained with the magnetic spectrometer [(a) and (c)] and TOF ion current distributions [(b) and (d)] measured by the SSCD detector for the different types of used targets. TOF measurements were useful during the experiment to control in real time the maximum energy (by identifying the beginning of the signal) and the proton beam flux. However they were placed at a larger angle compared to the magnetic spectrometer.

Figure 3(b) shows that the maximum proton energy was about 3.0 and 2.5 MeV for PET and NS$_{\rm rear}$ targets, respectively. Such result is in agreement with magnetic spectrometer measurements, where the maximum proton energy was about 3.6 and 3.0 MeV for PET and NS$_{\rm rear}$ targets, respectively. It is important to stress that such difference is attributed to the different detection angles of the two diagnostic systems (0° for the spectrometer and 9° for the SSCD detector). Figure 3(b) shows the maximum proton energy in the case of SiN and SiN$_{2\,\mu\rm m}$ targets, which was about 3.0 and 2.3 MeV, respectively. Also in this case the TOF results are in agreement with the ones obtained with the magnetic spectrometer.

Figure 4 shows raw images of proton beam imprints on the RCF for two of the used target types: (a) PET and (b) NS$_{\rm rear}$, in both cases obtained accumulating two consecutive shots. Proton beam imprints for PET show a divergence in FWHM, of ±5°. With NS$_{\rm rear}$ the situation is very different, and the divergence increases drastically up to ±10°. Furthermore, proton beams emerging from these targets are spatially more homogeneous than beams generated with PET. The degree of inhomogeneity of proton beams emerging from PET is about 16%, but only 8% in the case of NS$_{\rm rear}$. Such parameter was determined reconstructing a histogram of the beam dose profile. Then the standard deviation was calculated and divided by the mean which provided percentage value that describes the degree of homogeneity. The fact that the calculation is performed in dose domain is crucial as the intensity profile does not correspond to reality due to nonlinear response of the films. A comparison of the RCF imprints of protons emerging from the different targets (SiN, and SiN$_{1\,\mu\rm m}$ and SiN$_{2\,\mu\rm m}$) is shown in Fig. 5. The proton beam imprint for SiN [Fig. 5(a)], obtained accumulating two consecutive shots, shows a divergence of about ±4°. The shape of the proton imprint is very different when grating structures are present on the rear of the target [Figs. 5(b) and 5(c)], where in both cases RCFs were obtained only after one shot. The first important feature is that, in the direction parallel to the

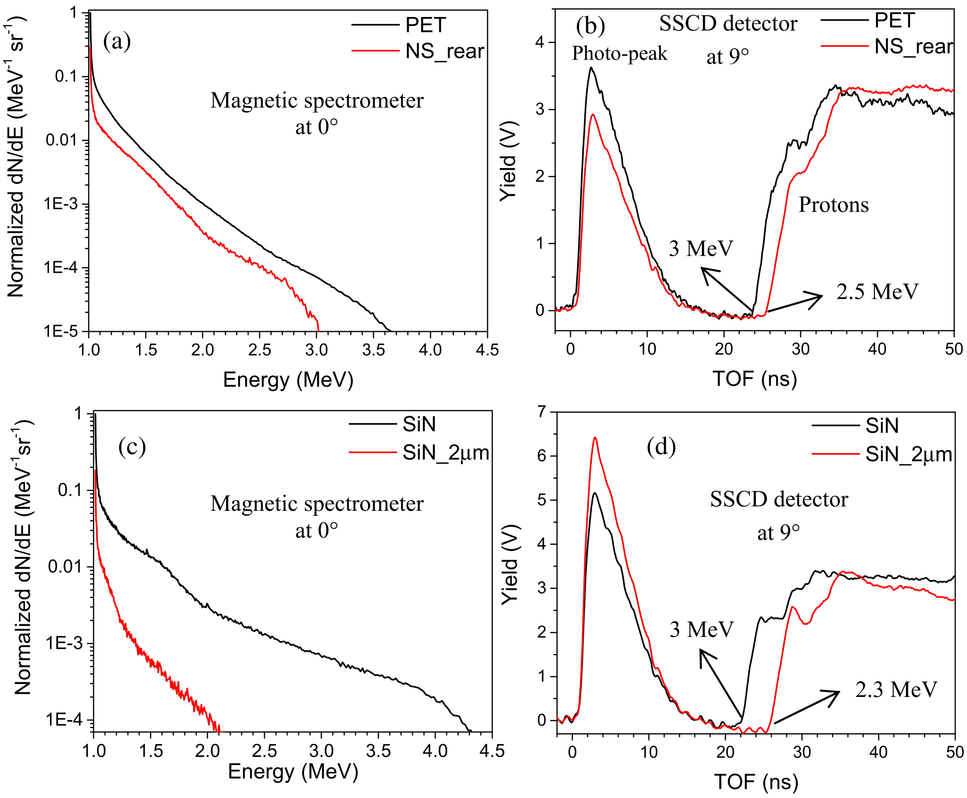

FIG. 3. Proton energy distributions measured by the magnetic spectrometer for PET and NS$_{\rm rear}$ (a) and for SiN and SiN$_{2\,\mu\rm m}$ (c); the corresponding TOF spectra from the SSCD detector are shown in (b) and (d).

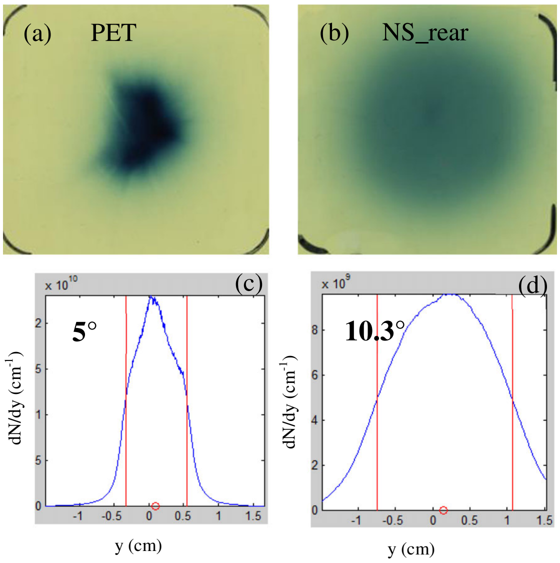

FIG. 4. Examples of radiochromic films (obtained accumulating 2 shots) showing spatial profiles of proton beams generated from PET target (a) and from NS$_{rear}$ (b). (c) and (d) represent the lateral profile of the proton beam respectively for PET and NS$_{rear}$ targets.

grating orientation, the divergence of the beam is reduced being about ±4° for SiN and ranging between ±1° and ±2° for SiN$_{1\,\mu m}$ and SiN$_{2\,\mu m}$ (statistical fluctuations in such a range are measured in different shots). The second very pronounced feature is observed in the direction perpendicular to the grating ridges, where the proton beam imprints are strongly stretched.

## IV. SIMULATIONS

In order to better understand the physics behind the experimental results, different sets of PIC simulations (2D and 3D) were performed with the PIC codes EPOCH [23] and PICADOR [24]. The ECLIPSE cluster built within the ELI-Beamlines project was used for the 3D simulations using the EPOCH code. Computing and storage facilities provided by the CERIT-SC Center were used for 2D simulations.

In the 3D simulations, which can fully describe the interaction geometry, we assumed a linearly p-polarized laser pulse with a Gaussian temporal profile of 30 fs (FWHM) and a Gaussian spatial profile of the beam with focal spot size of 4 μm (FWHM). The peak intensity of the pulse was set to $2 \times 10^{19}$ W/cm$^2$, the laser beam was incident on target with a 45° angle with respect to the target normal. The target is composed of a $C^{6+}H_2^{+}$ plasma with density of 40 $n_{ec}$, where $n_{ec}$ is the electron critical density. The initial target density profile was steplike in all cases. In the simulations, we assumed flat foils with a thickness of 700 nm (the same shape of the target as SiN target in the experiment) and grating target with the parameters shown in Fig. 1(b), i.e. with grooves of 0.5 $\mu$m in depth and 2 $\mu$m in width (the same shape of the target as SiN_2 $\mu$m target in the experiment). The sizes of cubic cells in 3D were equal to $16^3$ nm$^3$ and the number of macroparticles per cell was set to 40 electrons, 10 protons, and 5 $C^{6+}$ ions. The simulation box has sizes of $20 \times 28 \times 16$ $\mu$m.

The simulation results for SiN and SiN$_{2\,\mu m}$ presented in Fig. 6 show a good agreement with the experimental results. The simulations show a regular shape for the angular distribution of the accelerated protons from SiN

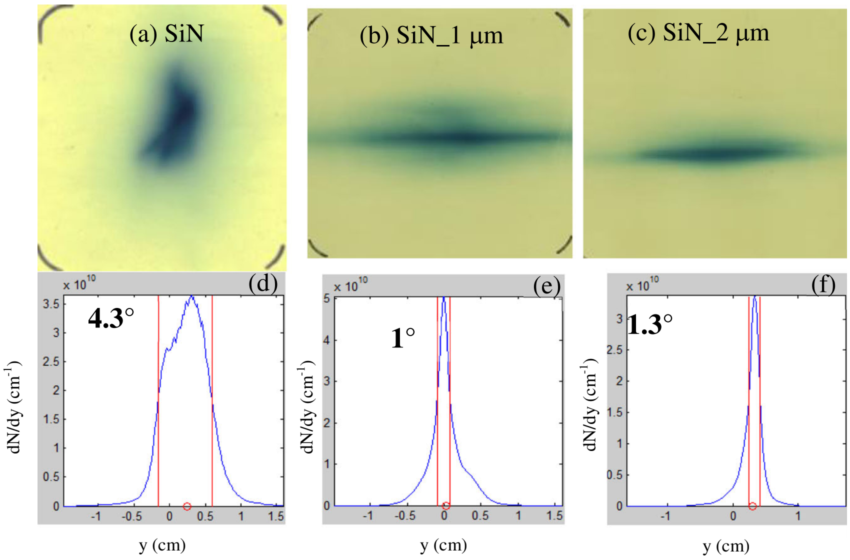

FIG. 5. Examples of radiochromic films showing the spatial profiles of proton beams emerging from SiN (obtained accumulating 2 shots) (a), from a SiN$_{1\,\mu m}$ (1 shot) (b) and from a SiN$_{2\,\mu m}$ (1 shot) (c) targets. (d),(e),(f) show the lateral profile of the proton beam for the different targets in (a)–(c).

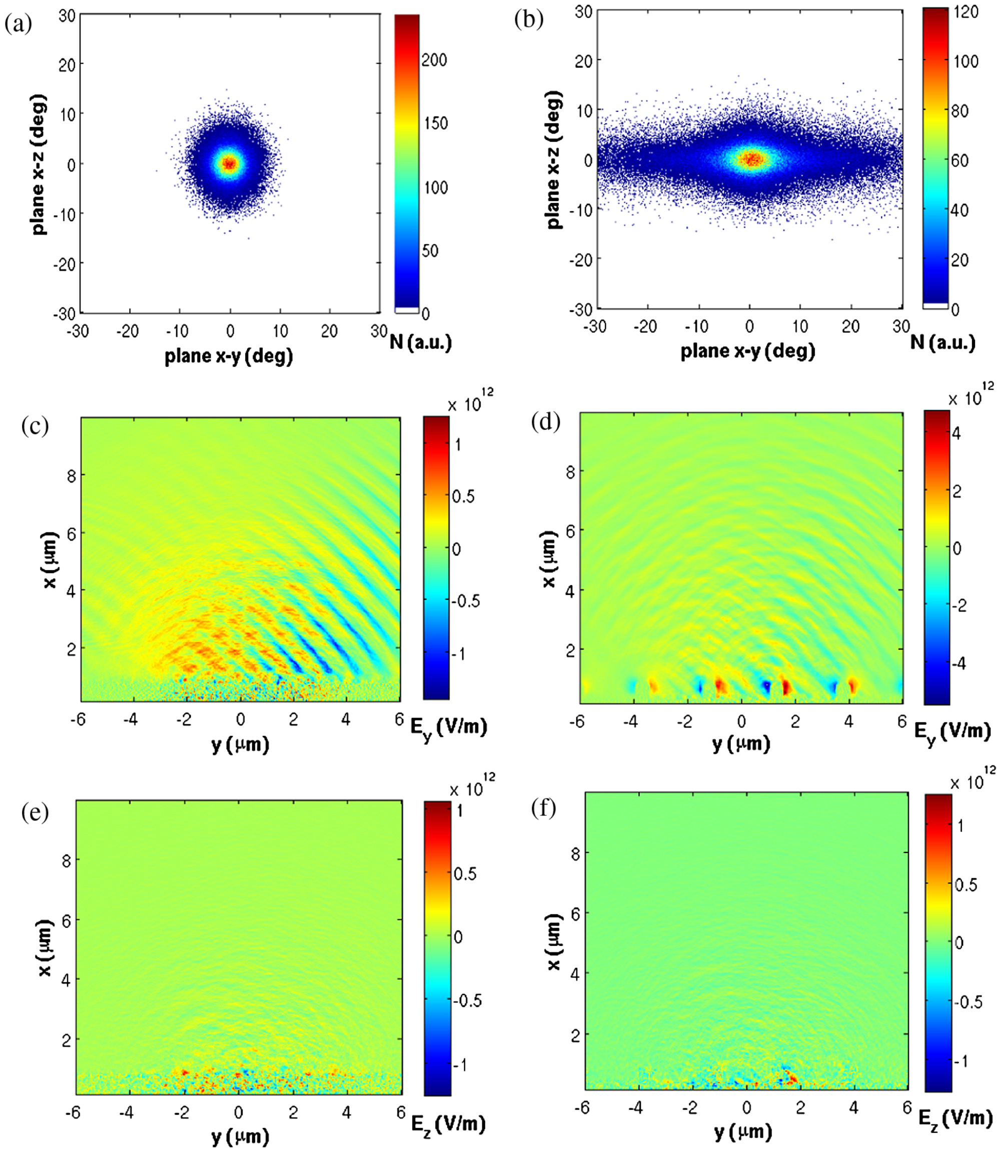

FIG. 6. Angular distribution of accelerated protons from 3D PIC simulations for SiN (a) and $\mathrm{SiN}_{2\,\mu\mathrm{m}}$ (b). (a), (b) Horizontal axis: deflection angle from the target normal direction ($x$ axis) in the plane $x-y$; vertical axis: deflection angle from the target normal direction ($x$ axis) in the plane $x-z$; colorbar: number of numerical macroparticles per spatial angle in simulations. Electric field perpendicular to the grating orientation for SiN (c) and $\mathrm{SiN}_{2\mu\mathrm{m}}$ (d) and electric field parallel to the grating orientation for SiN (e) and $\mathrm{SiN}_{2\,\mu\mathrm{m}}$ (f). The target front (laser-irradiated) surface is at $x = 0$, slightly outside the area shown in (c)–(f) (the laser comes from the bottom).

[see Fig. 6(a)] and a large angular spread perpendicular to the grating orientation (in the $y$ axis direction) for the structured target ($\mathrm{SiN}_{2\,\mu\mathrm{m}}$) [see Fig. 6(b)]. These results are better explained in Figs. 6(c) and 6(d), where the electric field in the $y$ axis direction is reported for the two targets. In Fig. 6(d) a transverse component of the electric field is present, which is mainly responsible for stretching the proton beam in the transverse direction. Figures 6(e) and 6(f) show the electric field in the $z$ axis direction for SiN and $\mathrm{SiN}_{2\,\mu\mathrm{m}}$ targets, respectively. They present very similar features, thus they cannot explain the observed difference in proton beam divergence in the $z$ direction, i.e. parallel to the grating grooves. However, it is clear from Figs. 6(a) and 6(b) that the density of the proton beam in the case of the SiN target is several times larger than in the case of the $\mathrm{SiN}_{2\,\mu\mathrm{m}}$ [the number of accelerated protons per unit solid angle in (a) is twice larger than in (b) in the middle of the beam]. Thus, a possible explanation for the different divergence measured experimentally for the flat and grating targets could be that the higher proton density at the source (in proximity of the target) for SiN can result in a higher divergence of the accelerated proton beam due to a larger

Coulomb repulsion between particles during the beam expansion. Similar results were observed for the geometric emittance calculated from 3D simulations, which was estimated to be about 0.45 mm mrad in the $z$ direction for both targets in the case of high-energy protons (above 2 MeV).

These results were also independently confirmed by 2D simulations using the codes EPOCH [23] and PICADOR [24] with similar parameters of the interaction in both 2D simulations. The results from 2D simulations qualitatively agree with 3D calculations in the influence of the presence of grating structures on the rear surface of the target in terms of corresponding proton angular distribution.

## V. DISCUSSION AND CONCLUSIONS

The possibility to manipulate the spatial profiles of proton beams generated by the interaction of an intense femtosecond laser pulse and advanced targets with surface nano- or microstructures on the rear side has been experimentally and numerically explored.

Nanospheres covering the rear surface of a flat plastic foil affect the final proton beam spatial profile in terms of beam divergence and homogeneity, such that it has a larger divergence and a more homogeneous spatial distribution compared to a proton beam emerging from a flat plastic foil of equivalent total thickness. This effect can be explained through a larger transverse emittance of the generated proton beam due to the microcurved surface, which smoothes down beam inhomogeneity compared to flat targets.

Grating structures of $\mu$m size covering the rear of silicon nitride targets were also used to modify the proton beam spatial distribution, reducing its divergence in the direction parallel to the grating orientation and stretching it in the perpendicular direction due to transverse electric fields generated inside the target grooves. This effect is completely new and according to our knowledge it was never investigated before. The behavior of these targets is completely different from that of targets described in [25], where metallic foils covered by sinusoidal microgrooves were irradiated with the aim of measuring the source size of the laser-accelerated protons for a given energy. In fact those targets were much thicker and the dimensions and size of the grooves were very different compared to the grating targets used in our investigations. Moreover, the most crucial difference lies in the laser pulse parameters. Reference [25] reports pulse duration of few hundreds of fs, whereas 35 fs pulses were used in our experiment. Since TNSA regime takes place during the laser-target interaction and the acceleration of ions is stopped shortly after the interaction, the front of the accelerated proton stream keeps the initial structure of the rear side of the target for ultrashort pulses during the whole acceleration time. In this case, the sheath is not homogeneous and the protons are accelerated both along the target normal direction and into the transverse direction as well. This phenomenon is illustrated by a strong transverse electric field generated due to rear-side structures [see Fig. 6(d)]. In the case of much longer laser pulses, e.g. in [25], the structures on the proton beam front are gradually smoothed and protons are mostly accelerated by a homogenized sheath along the target normal direction. Therefore, a modulated rear surface is here translated only into strip structures appearing in the proton beam spatial profile (as can be seen in Fig. 1 in [25] or in Fig. 2 in [26], but not in a larger proton beam divergence).

The present experimental results are confirmed by numerical simulations performed by using 2D and 3D PIC codes. A possible explanation of the observed reduction in proton divergence is Coulomb repulsion between charged particles during the proton beam expansion, which might be larger for the flat foil due to larger density of ions in the beam. However, this effect is not easily predictable by the PIC simulations because they show proton acceleration and propagation only up to a distance of a few $\mu$m from the target, i.e. where this effect is not yet fully developed.

Protons accelerated from targets with micro- and nanostructures on their rear side could be useful for applications in multidisciplinary research fields. In fact, the controlled divergence and the enhanced spatial homogeneity can be beneficial when using the generated proton beam for radiography [15] or cell irradiation [27,28], especially in the case of large objects to be investigated with a high temporal resolution, thus to be placed close to the source of nonrelativistic protons.

## ACKNOWLEDGMENTS

This work has been supported by the project ELI—Extreme Light Infrastructure—phase 2 (CZ.02.1.01/0.0/0.0/15_008/0000162) from European Regional Development Fund, the Ministry of Education, Youth and Sports of the Czech Republic (project No. LQ1606), the Czech Science Foundation (project No. 15-02964S), LASERLAB-EUROPE (Grant Agreement No. 284464, EC's Seventh Framework Programme), the Swedish Research Council and the Knut and Alice Wallenberg foundation, including its funding of the PLIONA project. Access to the CERIT-SC computing and storage facilities provided by the CERIT-SC Center, provided under the program "Projects of Large Research, Development, and Innovations Infrastructures" (CERIT Scientific Cloud LM2015085), is greatly appreciated.

[1] D. Strickland and G. Mourou, Compression of amplified chirped optical pulses, Opt. Commun. **56**, 219 (1985).

[2] G. Morou, C. Labaune, M. Dunne, N. Naumova, and V. Tikhonchuk, Relativistic laser-matter interaction: from attosecond pulse generation to fast ignition, Plasma Phys. Control. Fusion **49**, B667 (2007).

[3] Y. I. Salamin, S. Hu, K. Hatsagortsyan, and C. Keitel, Relativistic high-power laser–matter interactions, Phys. Rep. **427**, 41 (2006).

[4] V. Malka and P. Mora, Principles of laser–plasma accelerators, Les accélérateurs de particules laser–plasma, C.R. Phys. **10**, 106 (2009).

[5] M. Passoni, L. Bertagna, and A. Zani, Target normal sheath acceleration: theory, comparison with experiments and future perspectives, New J. Phys. **12**, 045012 (2010).

[6] S. C. Wilks, A. B. Langdon, T. E. Cowan, M. Roth, M. Singh, S. Hatchett, M. H. Key, D. Pennington, A. MacKinnon, and R. A. Snavely, Energetic proton generation in ultraintense laser–solid interactions, Phys. Plasmas **8**, 542 (2001).

[7] S. P. Hatchett *et al.*, Electron, photon, and ion beams from the relativistic interaction of Petawatt laser pulses with solid targets, Phys. Plasmas **7**, 2076 (2000).

[8] F. Wagner *et al.*, Maximum Proton Energy above 85 MeV from the Relativistic Interaction of Laser Pulses with Micrometer Thick CH2 Targets, Phys. Rev. Lett. **116**, 205002 (2016).

[9] D. C. Carroll *et al.*, Active manipulation of the spatial energy distribution of laser-accelerated proton beams, Phys. Rev. E **76**, 065401 (2007).

[10] B. Dromey *et al.*, Picosecond metrology of laser-driven proton bursts, Nat. Commun. **7**, 10642 (2016).

[11] T. E. Cowan *et al.*, Ultralow Emittance, Multi-MeV Proton Beams from a Laser Virtual-Cathode Plasma Accelerator, Phys. Rev. Lett. **92**, 204801 (2004).

[12] K. W. D. Ledingham, P. R. Bolton, N. Shikazono, and C.-M. C. Ma, Towards Laser Driven Hadron Cancer Radiotherapy: A Review of Progress, Appl. Sci. **4**, 402 (2014).

[13] A. Yogo *et al.*, Development of laser-driven quasi-monoenergetic proton beam line for radiobiology, Nucl. Instrum. Methods Phys. Res., Sect. A **653**, 189 (2011).

[14] M. Durante and J. S. Loeffer, Charged particles in radiation oncology, Nat. Rev. Clin. Oncol. **7**, 37 (2010).

[15] J. Mackinnon *et al.*, Proton Radiography of a Laser-Driven Implosion, Phys. Rev. Lett. **97**, 045001 (2006).

[16] M. Borghesi, A. Schiavi, D. H. Campbell, M. G. Haines, O. Willi, A. J. MacKinnon, L. A. Gizzi, M. Galimberti, R. J. Clarke, and H. Ruhl, Proton imaging: a diagnostic for inertial confinement fusion/fast ignitor studies, Plasma Phys. Control. Fusion **43**, A267 (2001).

[17] M. Temporal, R. Ramis, J. J. Honrubia, and S. Atzeni, Fast ignition induced by shocks generated by laser-accelerated proton beams, Plasma Phys. Control. Fusion **51**, 035010 (2009).

[18] D. Margarone *et al.*, Laser-Driven Proton Acceleration Enhancement by Nanostructured Foils, Phys. Rev. Lett. **109**, 234801 (2012); D. Margarone *et al.*, Laser-driven high-energy proton beam with homogeneous spatial profile from a nanosphere target, Phys. Rev. ST Accel. Beams **18**, 071304 (2015).

[19] T. Ceccotti *et al.*, Evidence of Resonant Surface-Wave Excitation in the Relativistic Regime through Measurements of Proton Acceleration from Grating Targets, Phys. Rev. Lett. **111**, 185001 (2013).

[20] G. Doumy, F. Quéré, O. Gobert, M. Perdrix, P. Martin, P. Audebert, J. C. Gauthier, J.-P. Geindre, and T. Wittmann, Complete characterization of a plasma mirror for the production of high-contrast ultraintense laser pulses, Phys. Rev. E **69**, 026402 (2004).

[21] L. Stolcova, J. Proska, F.Novotny, M. Prochazka, and I. Richter, Periodic arrays of metal nanobowls as SERS-active substrates, in *NANOCON 2011* (2011), vol. 1, pp. 737–741.

[22] Saint-Gobain website: http://www.crystals.saint-gobain.com/sites/imdf.crystals.com/files/documents/organics-brochure.pdf.

[23] T. D. Arber *et al.*, Contemporary particle-in-cell approach to laser-plasma modelling, Plasma Phys. Control. Fusion **57**, 113001 (2015).

[24] S. Bastrakov, R. Donchenko, A. Gonoskov, E. Efimenko, A. Malyshev, I. Meyerov, and I. Surmin, Particle-in-cell plasma simulation on heterogeneous cluster systems, J. Comput. Sci. **3**, 474 (2012).

[25] H. Ruhl, T. Cowan, and J. Fuchs, The generation of micro-fiducials in laser-accelerated proton flows, their imaging property of surface structures and application for the characterization of the flow, Phys. Plasmas **11**, L17 (2004).

[26] T. E. Cowan *et al.*, Ultralow Emittance, Multi-MeV Proton Beams from a Laser Virtual-Cathode Plasma Accelerator, Phys. Rev. Lett. **92**, 204801 (2004).

[27] S. D. Kraft *et al.*, Dose-dependent biological damage of tumour cells by laser-accelerated proton beams, New J. Phys. **12**, 085003 (2010).

[28] D. Doria *et al.*, Biological effectiveness on live cells of laser driven protons at dose rates exceeding $10^9$ Gy/s, AIP Adv. **2**, 011209 (2012).

# Appendix G

# Paper 7

PHYSICAL REVIEW SPECIAL TOPICS—ACCELERATORS AND BEAMS **18,** 071304 (2015)

# Laser-driven high-energy proton beam with homogeneous spatial profile from a nanosphere target

D. Margarone,[1] I. J. Kim,[2,3] J. Psikal,[1,4] J. Kaufman,[1,4] T. Mocek,[5] I. W. Choi,[2,3] L. Stolcova,[1,4]
J. Proska,[4] A. Choukourov,[1,6] I. Melnichuk,[6] O. Klimo,[1,4] J. Limpouch,[1,4] J. H. Sung,[2,3]
S. K. Lee,[2,3] G. Korn,[1] and T. M. Jeong[2,3,*]

[1]*ELI-Beamlines Project, Institute of Physics ASCR, v.v.i. (FZU), 182 21 Prague, Czech Republic*
[2]*Center for Relativistic Laser Science, Institute for Basic Science, Gwangju 500-712, Republic of Korea*
[3]*Advanced Photonics Research Institute, GIST, Gwangju 500-712, Republic of Korea*
[4]*FNSPE, Czech Technical University in Prague, 11519 Prague, Czech Republic*
[5]*HiLASE project, Institute of Physics of the ASCR, 18221 Prague, Czech Republic*
[6]*Faculty of Mathematics and Physics, Department of Macromolecular Physics,*
*Charles University in Prague, Czech Republic*

(Received 11 February 2015; published 10 July 2015)

A high-energy, high-yield proton beam with a good homogeneous profile has been generated from a nanosphere target irradiated by a short (30-fs), intense ($7 \times 10^{20}$ W/cm$^2$) laser pulse. A maximum proton energy of 30 MeV has been observed with a high proton number of $7 \times 10^{10}$ in the energy range 5–30 MeV. A homogeneous spatial profile with a uniformity (standard deviation from an average value within 85% beam area) of 15% is observed with the nanosphere dielectric target. Particle-in-cell simulations show the enhancement of proton cutoff energy and proton number with the nanosphere target and reveal that the homogeneous beam profile is related with a broadened angular distribution of hot electrons, which is initiated by the nanosphere structure. The homogeneous spatial properties obtained with the nanosphere target will be advantageous in developing laser-driven proton sources for practical applications in which high-quality beams are required.

DOI: 10.1103/PhysRevSTAB.18.071304 PACS numbers: 52.38.Ph, 41.75.Jv, 52.50.Dg

## I. INTRODUCTION

In the past decade, great attention has been paid to laser-driven ion acceleration as an innovative approach for medical applications, especially cancer therapy [1]. Because of the novel concept, research groups have mostly focused on the basic performances of laser-accelerated ion beams, i.e., the increase in the maximum proton or ion energy using advanced targets, the generation of quasimonoenergetic energy spectra, and the search for efficient acceleration mechanisms. As a result, the production of 60–70-MeV protons [2], quasimonoenergetic features in the spectrum [3,4], and various acceleration schemes, such as target normal sheath acceleration (TNSA) [5], radiation-pressure acceleration (RPA) [6,7], break-out afterburner [8,9], and hybrid TNSA-RPA [10,11], were reported in the literature. Despite the fast progress and great potential of laser-driven ion acceleration, a number of issues including the increase of proton energy up to a few hundreds of MeV, high-conversion efficiency, reduced shot-to-shot fluctuations in the energy spectrum, and improved ion beam quality are still considered as main topics to be investigated and resolved in the near future [12].

The use of laser-driven proton sources in practical applications requires the production of reliable, high-energy, and high-conversion-efficiency proton beams. As an effort in this direction, a micron-thick plastic foil target covered by a nanosphere monolayer was proposed [13], and its capability of producing ~10-MeV proton beams with enhanced conversion efficiency was experimentally demonstrated by using a 100-TW-class laser at an intensity of $5 \times 10^{19}$ W/cm$^2$ [14]. The role of the nanosphere monolayer was to boost the laser absorption on the laser-irradiated target surface. The higher absorption enhanced the hot electron population generated. As a consequence, the proton beam cutoff energy was increased by a factor of 1.5 and the number of protons by a factor of 6. The main motivation of our work is to extend the validity of such an acceleration mechanism at higher laser intensities and also to report the improved homogeneity of the proton beam spatial profile in order to show its potential use when higher proton energies (100-MeV level), which are needed for medical applications (namely, hadron therapy), are obtained.

In this paper, we report on laser-driven proton acceleration using nanosphere targets (similar to the previous ones in Refs. [14] and [15]) at higher laser intensities (up to

---

[*] To whom all correspondence should be addressed.
jeongtm@gist.ac.kr

*Published by the American Physical Society under the terms of the Creative Commons Attribution 3.0 License. Further distribution of this work must maintain attribution to the author(s) and the published article's title, journal citation, and DOI.*

$7 \times 10^{20}$ W/cm$^2$) confirming the enhancement of the proton cutoff energy and the increase of the proton number. The completely new achievement is represented by the generation of a homogeneous proton beam spatial profile, which is experimentally observed and considered as an additional benefit of the use of a nanosphere insulator target. In fact, irregular proton beam spatial profiles are common for a dielectric target, and their origin can be explained by several mechanisms [16]. Our two-dimensional (2D) particle-in-cell (PIC) simulations show good agreement with the experimental observations in terms of proton cutoff energy and proton number and also provide an interpretation of the origin of the homogeneous beam spatial profile ascribable to a broad angular distribution of hot electrons on the front surface of the nanosphere target. Both experimental and numerical results show that a micron-thick foil target with a nanosphere monolayer has a crucial importance of producing high-energy high-quality proton beams through laser-matter interaction at higher laser intensities; thus, the nanosphere target can be used as a proton beam source for multidisciplinary applications.

## II. EXPERIMENTAL SETUP AND DIAGNOSTICS

Our acceleration experiments were performed with the 30-fs, 0.1-Hz-repetition-rate, 1-PW laser operating at the Center for Relativistic Laser Science (CoReLS), Institute for Basic Science (IBS) in Korea. The overall output performance of the petawatt laser is described elsewhere [17]. A double plasma mirror system was employed to maintain the temporal contrast ratio (ratio between the intensity of a main femtosecond pulse and the intensity of a nanosecond pedestal) as low as $3 \times 10^{11}$ up to 6 ps before the main laser pulse. This is a crucial parameter when using a target with special structures on the front surface which should be sustained from the preplasma formed by amplified spontaneous emission and prepulse before the main laser pulse [18]. On the other hand, the laser energy on target was reduced by a factor of more than 2 compared to the output at the exit of the pulse compressor chamber, due to the presence of a double plasma mirror system which was used to enhance the laser pulse temporal contrast ratio on target. The laser pulse was focused with an $f/3$ off-axis parabolic (OAP) mirror, and the measured spot size was $\sim 4$ $\mu$m at FWHM, yielding a maximum peak intensity of $7 \times 10^{20}$ W/cm$^2$. Such an intensity value was estimated by considering a laser pulse energy of $\sim 30$ J at the exit of the pulse compressor reduced to $\sim 10$ J delivered on target because of the upstream optical elements (double plasma mirror, large-aperture half-wave plates, and gold-coated OAP). Furthermore, a laser energy of 2.5 J (25%) out of 10 J was contained in the 4-$\mu$m focal spot. The laser beam was $s$-polarized on target.

Two types of targets were used in the experiment: (i) planar target (PT) consisting of a 700-nm-thick Mylar foil and (ii) nanosphere target (NST) with an effective thickness of 720 nm. The latter consisted of a monolayer of polystyrene spheres (470 nm in diameter) placed on a double layer substrate (200-nm-thick silicon nitride membrane and 50-nm-thick polyethylene film on the rear side). Details on the fabrication of target substrates (hydrocarbon polymeric thin films) using the physical vapor deposition technique can be found in Ref. [19], and the fabrication of the nanosphere target is based on the self-assembly at the water-air interface as described in Ref. [20]. The damage-threshold fluence of the nanosphere structure has been estimated to range between 1 and 10 J/cm$^2$ for approximate nanosecond laser pulses [21]; thus, the nanosphere structure was operational in our experimental conditions, in which the prepulse intensity was maintained at $10^9$–$10^{10}$ W/cm$^2$ when considering the temporal contrast ratio. The target was inclined by 9° to the laser propagation direction to avoid the laser pulse retroreflection. The proton and ion energy spectra were measured by a Thomson Parabola (TP) spectrometer equipped with a microchannel plate (MCP) and a 16-bit charge-coupled device (CCD). A phosphor screen in the MCP was placed 12 cm away from the output plane of the electric field (25.5 kV/cm) and the magnetic field gradient (0.4 T/cm) deflection regions. The image on the phosphor screen was relayed to the CCD camera for a real-time measurement. A typical TP

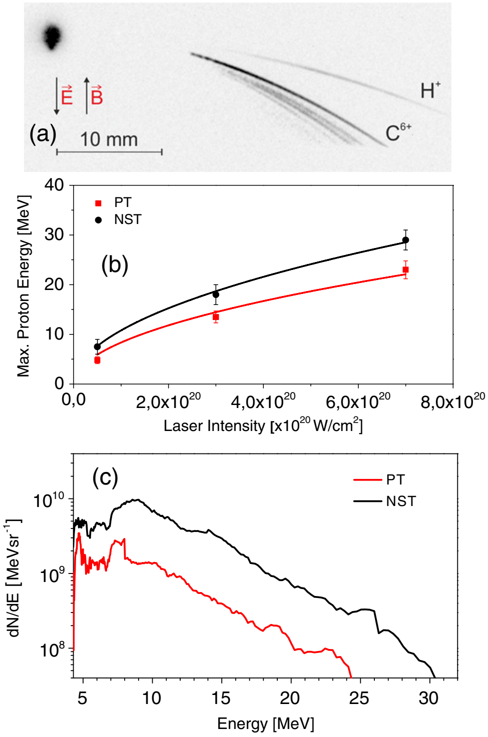

FIG. 1. Typical TP snapshot for a NST target (a); maximum proton energy vs laser intensity in three different experimental campaigns at CoReLS-IBS (b); typical proton energy distributions for PT and NST targets at $7 \times 10^{20}$ W cm$^{-2}$ (c).

spectrum is shown in Fig. 1(a). The absolute number calibration for the proton energy spectra was done by installing striped CR-39 track detectors in front of the MCP device [22]. A stack of radiochromic film (RCF) detectors was placed 5 cm behind the target mainly for an *ex situ* estimation of the entire proton beam spatial profile and divergence in different proton energy ranges [23]. The parasitic dose contribution by high-energy protons in a certain RCF layer was corrected by a post-data-analysis process using predetermined weighting coefficients obtained from the proton Bragg curves simulated in the stopping and range of ions in matter.

## III. RESULTS AND DISCUSSIONS

As demonstrated in previous papers [14,15], both the proton cutoff energy and the number of protons further increased with nanosphere targets at higher intensities. Figure 1(b) shows the proton cutoff energy as a function of laser intensity on the target. The experimental data referring to three different campaigns at different laser intensities of about $5\times10^{19}$, $3\times10^{20}$, and $7\times10^{20}$ W/cm$^2$, respectively, are summarized. The maximum proton energy roughly scales with the square root of the laser intensity, which is considered as the typical scaling law in the TNSA regime. The maximum proton energy for the nanosphere target is roughly 1.5 times higher than for the planar one in the whole laser intensity range.

Figure 1(c) shows proton energy spectra for PT and NST targets recorded with the TP spectrometer. The maximum cutoff energies (with a corresponding intensity 5 times higher than the noise standard deviation after background subtraction) for PT and NST targets are about 24 and 30 MeV, respectively. Thus, an increase of about 25% in the maximum proton energy is achieved with the NST target. The total proton yield for energies above 5 MeV is also enhanced from $1.5\times10^{10}$ for PT to $6.9\times10^{10}$ for NST, resulting in an increase of 350% (a factor of about 4.5) in the total proton number. If the proton number in the energy window 13–23 MeV is considered, the enhancement is more than a factor of 3 for NST compared to PT. The proton acceleration efficiency, defined by the ratio between the total proton beam energy [integral of $E\cdot f(E)$, where $E$ is the proton energy and $f(E)$ is the proton energy distribution] and the laser energy, is also enhanced by a factor of about 5 (from 0.3% for planar targets to 1.5% for nanosphere targets).

The enhancement of the proton cutoff energy and the proton number are also confirmed by PIC simulations. The 2D PIC code described in Ref. [24] was employed for detailed analyses of experimental results. The input parameters of simulation runs were appropriately adjusted to circumvent the limitation of the 2D PIC method. In the simulations, both the planar foil and the nanosphere target consist of $C^{6+}H_2{}^{+}$ plasma with an electron density ($n_e$) of $3.5\times10^{23}$ cm$^{-3}$ ($200n_c$), where $n_c$ is the critical electron density. The planar foil target has a thickness of 750 nm. The nanosphere target consists of a monolayer of closely packed nanospheres on the front (laser-irradiated) side and a 250-nm-thick dielectric substrate similarly to the real geometry measured through SEM analyses [20]. Each nanosphere has a diameter of 460 nm. The beam width of the focal spot is set to 1.6 $\mu$m (at FWHM). Gaussian distributions in temporal and spatial profiles are assumed in simulations. A smaller beam diameter than the experimental one is used to represent 3D-lateral losses of hot electrons in the 2D-geometry model as discussed in Ref. [14]. The target is initialized with a steplike density profile. However, a 30-fs prepulse with one-hundredth peak intensity of the main pulse, which arrives 50 fs prior to the main pulse interaction (based on spectral phase interferometry for direct electric-field reconstruction measurements) and creating a short preplasma on the target, is introduced in our simulations. Since the diameter of the spheres is several times smaller than the focal spot size, the result is not sensitive to the distribution of the nanospheres owing to the laser focal spot position. In a real 3D geometry, the electrons traveling on a line parallel to the surface would experience a spatial periodicity equal to the size of the sphere only along a limited set of directions [25]. According to their initial acceleration direction, electrons can cross any vacuum region between any couple of spheres or can travel along a different path, showing an even more complicated periodicity of the system. However, as observed in our first theoretical proposal [13], the results are not very different when a monolayer of nanospheres having random diameters in the range 200–800 nm are used compared to nanospheres having a fixed diameter. Thus, even if multidimensional effects are more complicated, we expect a similar qualitative difference between the nanosphere target and the flat foil when comparing 2D and 3D PIC simulation outputs.

The simulation results for proton energy spectra are shown in Fig. 2. The energies of accelerated protons at the end of the simulations (200 fs after laser-target interaction)

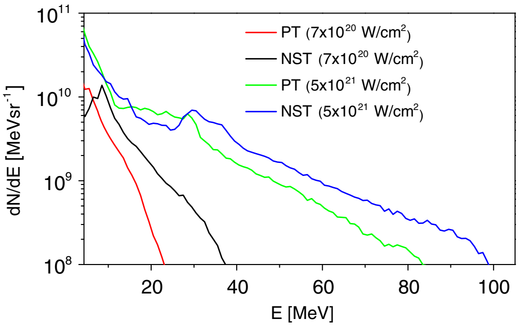

FIG. 2. Proton energy spectra for planar and nanosphere targets at the end of PIC simulations.

were compared with the experimental ones. The cutoff energy agrees relatively well for a planar target, whereas the proton energy from a nanosphere target is overestimated in the PIC simulation. The higher cutoff energy in the PIC simulation (~23%) can be explained by larger lateral losses of hot electrons in the experiment (two lateral dimensions in 3D) due to their larger angular spread at the target front surface. As already mentioned, only one lateral dimensional loss is considered in our 2D PIC simulations, and we applied a correction factor based on the decrease of the laser beam size in the 2D simulations. However, such a correction is fully applicable only for planar foils, since in the case of nanosphere targets a focal spot size below 1 $\mu$m (close to the diffraction limit) should have been used. This was not possible to be set up in our PIC simulations. Therefore, we applied the same correction to planar and nanosphere targets. The envisioned proton energy spectrum with the same nanosphere target at even higher laser intensity is also plotted in Fig. 2. According to the PIC simulations, a cutoff energy of 100 MeV is expected when a nanosphere target is irradiated by a laser pulse with an intensity of $5 \times 10^{21}$ W/cm$^2$ that is still in agreement with the square root of the laser intensity scaling law valid in the TNSA regime.

Figure 3 shows proton beam profiles recorded with RCF layers at different proton energies. The images in Fig. 3 were obtained by scanning RCFs with three shots accumulated for the NST and five shots for the PT, and the image quality was improved with a linear pseudocolor scale. As for the PT, the proton beam divergence decreases from ~30° to ~20° as the proton energy increases. A significant decrease to ~6° in the divergence angle was observed in a RCF layer located close to the cutoff energy. The same result can be observed in PIC simulations. As for the NST, the divergence angle remains constant for all proton energies (~25°). Moreover, a ring structure is observed outside the proton beam profile. Such a ring structure is very regular and thus can be easily removed with a proper collimator. It is inferred from PIC simulations that a higher divergence of protons at a higher energy is related with the lateral expansion of outermost peak structures (corresponding to a ring structure in the experiment) in the angular distribution of protons (as discussed below).

Figures 4(a) and 4(b) show the angular spectrum and the momentum of hot electrons in the phase space for the planar and the nanosphere targets from PIC simulations. The difference in angular distribution can be explained by trajectories of electrons on the front surface of the targets as shown in Ref. [25], and it agrees well with our previous numerical results obtained at a lower laser intensity [13]. Hot electrons can be generated when the electric field associated with the laser pulse, which forces electrons to oscillate in vacuum, is shielded by the plasma (ionized target). The shielding of the laser pulse electric field strongly depends on the morphology of the target front surface. When this surface consists of multiple curvatures, such as in the case of a nanosphere target, the electric field can be shielded in various directions of electron oscillations, thus leading to a larger number of electrons generated and to an increase in their temperature, along with a broader angular distribution.

The electron sheath distribution shortly after the end of laser-target interaction can be extracted from the PIC simulations as shown in Figs. 4(c) and 4(d) for both NST and PT. The shape of the hot electron cloud on the target rear side (electron sheath distribution) is different due to the initial angular distribution of hot electrons generated on the target front side. In fact, after the initial propagation through the target, the electrons recirculate back and forth and also propagate towards the target lateral sides. Our interpretation is that a narrow angular distribution of the generated hot electrons for a plane target leads to electron filamentation in the dielectric foil. However, we are not able to consider such filamentation by numerical simulations, since PIC simulations have to start with the presence of a "warm" plasma having some ionization degree since the very beginning, which is a mandatory assumption due to numerical constraints.

The most interesting feature in our results is the homogeneous beam profile obtained with a nanosphere dielectric target, as already shown in Fig. 3. This homogeneous spatial profile is particularly evident when it is compared to the one obtained with a planar insulator target where typical irregular features are present. According to Refs. [16,26], the observation of irregular structures in the beam profile on RCF is attributed to electron filaments

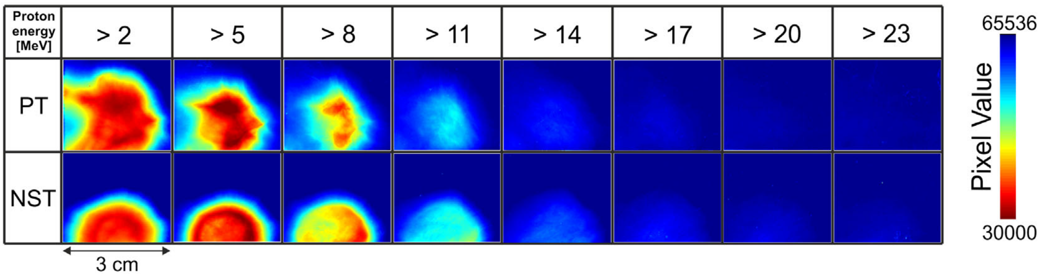

FIG. 3. Proton beam profile using red color channel for PT and NST targets obtained from the RCF diagnostics.

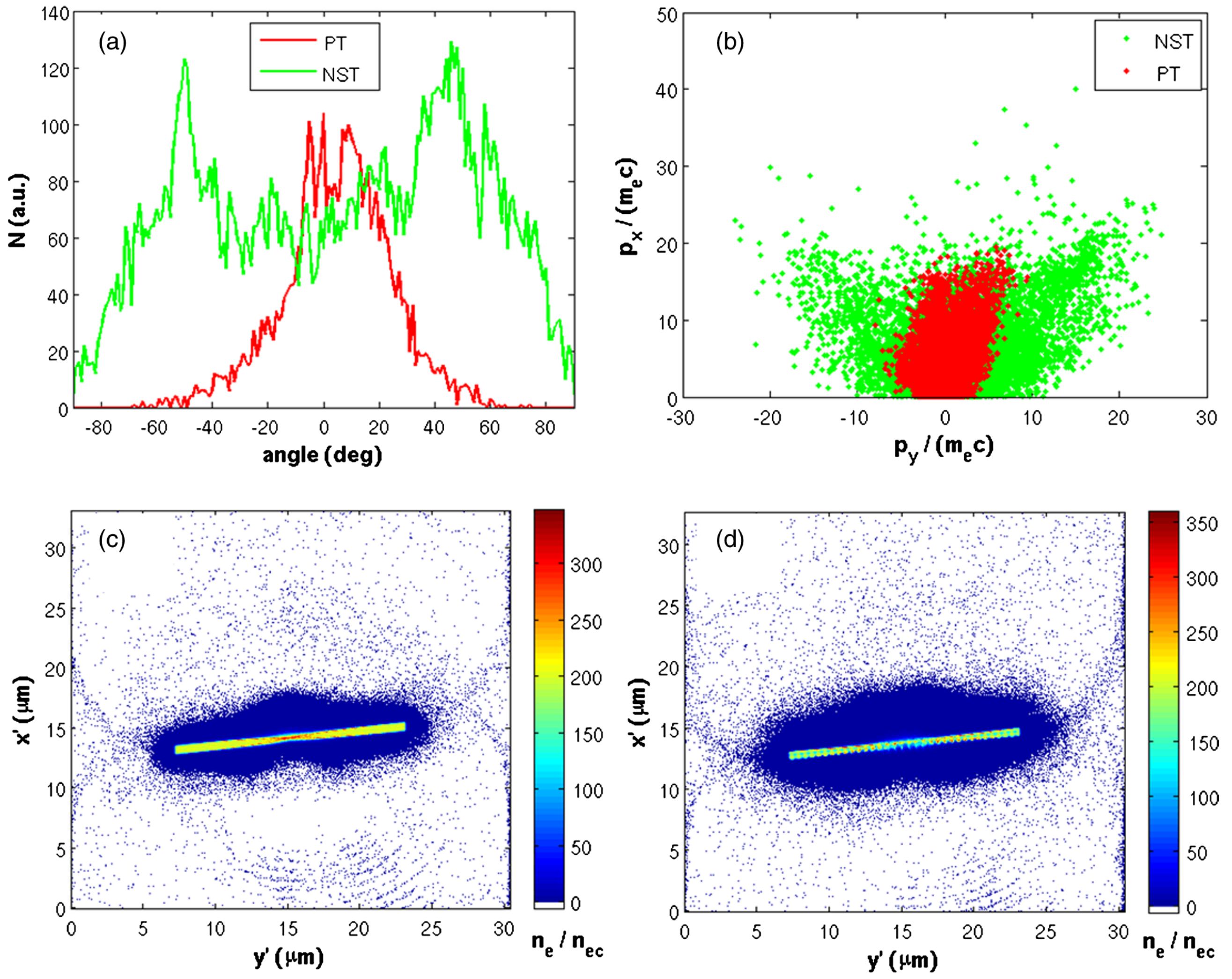

FIG. 4. (a) Angular distribution of hot electrons with energy higher than 1 MeV during laser-target interaction in the forward direction. (b) Momentum space of hot electrons in the forward direction; electrons moving along the target normal direction have a perpendicular component of momentum $p_y = 0$. (c) Hot electron distribution for a PT; (d) hot electron distribution for a NST.

developed in insulators. This filamentation is ascribed to the instability of the ionization front related to the electric field ionization process [26]. Only a small perturbation on an underlying smooth hot electron sheath distribution can lead to inhomogeneity in the spatial profile of the accelerated protons and typically appears for insulator layers thicker than 100 nm [16,27]. On the other hand, a broad (relatively low current density) and homogeneous angular distribution of hot electrons generated in a nanosphere target can mitigate such filamentation, resulting in a homogeneous proton beam profile.

The difference in spatial proton beam profiles between planar and nanosphere targets can be partially explained with the help of PIC simulation results. Figure 5 shows the proton density distributions about 150 fs after the laser-target interaction. In the case of a planar foil [Fig. 5(a)], a narrow peak structure is observed in the expanding proton front. This narrow ion beam might show irregular structures in the spatial beam profile (as recorded experimentally by RCFs) due to filamentation experienced by hot electrons. In fact, even if the electron filamentation cannot be observed directly in our PIC simulations (because ionization and collisions are not included), it is reasonable to assume that the narrow angular distribution of hot electrons (relatively high current density) can generate filamentation when propagating through an insulator target, in agreement with previous theoretical and experimental findings [16,27,28]. On the other hand, for a nanosphere target [Fig. 5(b)], a broader proton front profile with two smaller peaks (corresponding to the ring structure observed experimentally) is shown. This might be ascribed to the absence of filamentation in the hot electron population when propagating through the insulator target thanks to their broad and homogeneous spatial distribution.

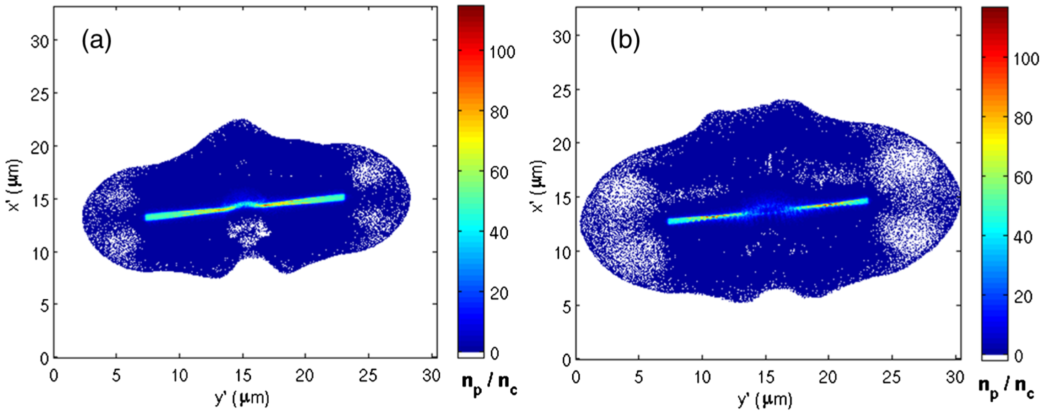

FIG. 5. Proton density distribution after laser-target interaction (a) for a planar target and (b) for a nanosphere target.

## IV. CONCLUSIONS

We have extended the validity of the micron-thick nanosphere targets to higher intensities (up to $7 \times 10^{20}$ W/cm$^2$) by enhancing the cutoff energy and the number of laser-driven protons with respect to our previous achievements [14,15]. Besides, we have shown for the first time that a nanosphere dielectric target could produce a homogeneous beam profile with a constant divergence angle. In fact, insulator targets are widely investigated by research groups working in this field, since they present the main advantage to allow reducing shot-to-shot fluctuations in the accelerated proton beam number compared to metallic foils where the protons are accelerated from hydrocarbon impurities on the target rear side, thus leading to large fluctuations in the proton beam current. On the other hand, dielectric targets typically show an inhomogeneous spatial profile due to filamentation effects of the hot electrons which develop during their propagation through the insulator foil. This is a clear drawback which typically limits the use of such targets, especially when ultrahigh intensities, and hence large hot electron current densities, are used.

The homogeneous proton beam profile could be partially explained by the mitigation of hot electron instabilities due to an increased transverse momentum component. Thus, from both our experimental and numerical results, it can be concluded that homogeneous and high-energy proton beams having high-conversion efficiency can be attained by using nanosphere dielectric targets. A continuous effort to produce homogeneous and high-yield 100-MeV-level proton beams from a nanosphere insulator target should be pursued for biomedical applications having a high societal impact. According to our numerical simulations, a 100-MeV proton cutoff energy can be achieved at a laser intensity of about $5 \times 10^{21}$ W/cm$^2$ by using a focusing mirror with a shorter focal length and by improving the reflection efficiency of a plasma mirror. Moreover, a clear increase of the proton yield (a factor of 2.5 for NST compared to PT) in an energy range already of interest for medical applications (73–83 MeV) [29] is achievable.

From a practical point of view, a micron-thick nanosphere dielectric target can provide a freestanding, robust, and easy-to-handle target solution, and the improved spatial features obtained with a nanosphere target offer additional benefits in delivering proton beams to a potential user station for applications (such as radiobiology or future laser-based hadron therapy) through a beam transport system using magnetic optics. In fact, the homogeneous beam profile and its constant divergence angle are crucial features in designing the whole beam transport section for applications. In conclusion, due to the increasing demand of reliable proton beams for multidisciplinary applications, the use of nanosphere dielectric targets can be considered as a promising solution to provide high-energy and high-yield proton beam sources with an improved beam quality in terms of the spatial profile.

## ACKNOWLEDGMENTS

The technical supports provided by the Center for Relativistic Laser Science of Institute for Basic Science, Korea, and by the Advanced Photonics Research Institute of GIST, Korea, are greatly acknowledged. This work was supported by IBS (Institute for Basic Science, Korea) under IBS-R012-D1. This research was also supported by the Academy of Sciences of the Czech Republic (M100101210), by the Ministry of Education, Youth and Sports of the Czech Republic (ELI-Beamlines reg. No. CZ.1.05/1.1.00/02.0061 and project No. LD14089), by Czech Science Foundation Project No. 15-02964S, and partially by the project "Centre for Innovation and Technology Transfer" (Project No. CZ.1.05/3.1.00/10.0210).

[1] S. V. Bulanov and V. S. Khoroshkov, Plasma Phys. Rep. **28**, 453 (2002).

[2] R. A. Snavely, M. H. Key, S. P. Hatchett, T. E. Cowan, M. Roth, T. W. Phillips, M. A. Stoyer, E. A. Henry, T. C. Sangster, M. S. Singh, S. C. Wilks, A. MacKinnon,

A. Offenberger, D. M. Pennington, K. Yasuike, A. B. Langdon, B. F. Lasinski, J. Johnson, M. D. Perry, and E. M. Campbell, Phys. Rev. Lett. **85**, 2945 (2000); S. A. Gaillard, T. Kluge, K. A. Flippo, M. Bussmann, B. Gall, T. Lockard, M. Geissel, D. T. Offermann, M. Schollmeier, Y. Sentoku, and T. E. Cowan, Phys. Plasmas **18**, 056710 (2011).

[3] B. M. Hegelich, B. J. Albright, J. Cobble, K. Flippo, S. Letzring, M. Paffett, H. Ruhl, J. Schreiber, R. K. Schulze, and J. C. Fernandez, Nature (London) **439**, 441 (2006).

[4] A. Henig, S. Steinke, M. Schnurer, T. Sokollik, R. Horlein, D. Kiefer, D. Jung, J. Schreiber, B. M. Hegelich, X. Q. Yan, J. Meyer-ter-Vehn, T. Tajima, P. V. Nickles, W. Sandner, and D. Habs, Phys. Rev. Lett. **103**, 245003 (2009).

[5] S. C. Wilks, A. B. Langdon, T. E. Cowan, M. Roth, M. Singh, S. Hatchett, M. H. Key, D. Pennington, A. MacKinnon, and R. A. Snavely, Phys. Plasmas **8**, 542 (2001).

[6] T. Esirkepov, M. Borghesi, S. V. Bulanov, G. Mourou, and T. Tajima, Phys. Rev. Lett. **92**, 175003 (2004).

[7] A. Macchi, F. Cattani, T. V. Liseykina, and F. Cornolti, Phys. Rev. Lett. **94**, 165003 (2005).

[8] L. Yin, B. J. Albright, K. J. Bowers, D. Jung, J. C. Fernández, and B. M. Hegelich, Phys. Rev. Lett. **107**, 045003 (2011).

[9] D. Jung, L. Yin, B. J. Albright, D. C. Gautier, S. Letzring, B. Dromey, M. Yeung, R. Hörlein, R. Shah, S. Palaniyappan, K. Allinger, J. Schreiber, K. J. Bowers, H. C. Wu, J. C. Fernandez, D. Habs, and B. M. Hegelich, New J. Phys. **15**, 023007 (2013).

[10] S. Kar, K. F. Kakolee, B. Qiao, A. Macchi, M. Cerchez, D. Doria, M. Geissler, P. McKenna, D. Neely, J. Osterholz, R. Prasad, K. Quinn, B. Ramakrishna, G. Sarri, O. Willi, X. Q. Yuan, M. Zepf, and M. Borghesi, Phys. Rev. Lett. **109**, 185006 (2012).

[11] I J. Kim, K. H. Pae, C. M. Kim, H. T. Kim, J. H. Sung, S. K. Lee, T. J. Yu, I. W. Choi, C.-L. Lee, K. H. Nam, P. V. Nickles, T. M. Jeong, and J. Lee, Phys. Rev. Lett. **111**, 165003 (2013).

[12] H. Daido, M. Nishiuchi, and A. S. Pirozhkov, Rep. Prog. Phys. **75**, 056401 (2012).

[13] O. Klimo, J. Psikal, J. Limpouch, J. Proska, F. Novotny, T. Ceccotti, V. Floquet, and S. Kawata, New J. Phys. **13**, 053028 (2011).

[14] D. Margarone, O. Klimo, I. J. Kim, J. Prokupek, J. Limpouch, T. M. Jeong, T. Mocek, J. Psikal, H. T. Kim, J. Proska, K. H. Nam, L. Stolcova, I. W. Choi, S. K. Lee, J. H. Sung, T. J. Yu, and G. Korn, Phys. Rev. Lett. **109**, 234801 (2012).

[15] D. Margarone, O. Klimo, I J. Kim, J. Prokupek, J. Limpouch, T. M. Jeong, T. Mocek, J. Psikal, H. T. Kim, J. Proska, K. H Nam, I. W. Choi, T. Levato, L. Stolcova, S. K. Lee, M. Krus, F. Novotny, J. H. Sung, J. Kaufman, T. J. Yu, and G. Korn, in *Proceedings of the SPIE Conference: High-Power, High-Energy, and High-Intensity Laser Technology, and Research Using Extreme Light: Entering New Frontiers with Petawatt-Class Lasers*, edited by J. Hein, G. Korn, and L. O. Silva (SPIE, Bellingham, WA, 2013), Vol. 8780, p. 878023.

[16] J. Fuchs, T. E. Cowan, P. Audebert, H. Ruhl, L. Gremillet, A. Kemp, M. Allen, A. Blazevic, J.-C. Gauthier, M. Geissel, M. Hagelich, S. Karsch, P. Parks, M. Roth, Y. Sentoku, R. Stephens, and E. M. Campbell, Phys. Rev. Lett. **91**, 255002 (2003).

[17] T. M. Jeong and J. Lee, Ann. Phys. (Amsterdam) **526**, 157 (2014).

[18] K. A. Ivanov, A. V. Brantov, S. I. Kudryashov, S. V. Makarov, D. A. Gozhev, R. V. Volkov, A. A. Ionin, V. Yu. Bychenkov, and A. B. Savelev, Laser Phys. Lett. **12**, 046005 (2015).

[19] A. Choukourov, I. Melnichuk, I. Gordeev, O. Kylián, J. Hanuš, J. Kousal, P. Solař, L. Hanyková, J. Brus, D. Slavínská, and H. Biederman, Thin Solid Films **565**, 249 (2014).

[20] J. Limpouch, J. Psikal, O. Klimo, J. Vyskocil, J. Proska, F. Novotny, L. Stolcova, and M. Kveton, in *Proceedings of the SPIE Conference: High-Power, High-Energy, and High-Intensity Laser Technology and Research Using Extreme Light: Entering New Frontiers with Petawatt-Class Lasers*, edited by J. Hein, G. Korn, and L. O. Silva (SPIE, Bellingham, WA, 2013), Vol. 8780, p. 878027.

[21] D. Margarone, A. Velyhan, L. Torrisi, M. Cutroneo, L. Giuffrida, A. Picciotto, J. Krasa, S. Cavallaro, J. Limpouch, O. Klimo, J. Psikal, J. Proska, and F. Novotny, Appl. Surf. Sci. **272**, 132 (2013).

[22] R. Prasad, D. Doria, S. Ter-Avetisyan, P. S. Foster, K. E, Quinn, L. Romagnani, C. M. Brenner, J. S. Green, P. Gallegos, M. J. V. Streeter, D. C. Carroll, O. Tresca, N. Dover, C. A. J. Palmer, J. Schreiber, D. Neely, Z. Najmudin, P. McKenna, M. Zepf, and M. Borghesi, Nucl. Instrum. Methods Phys. Res., Sect. A **623**, 712 (2010).

[23] D. Kirby, S. Green, F. Fiorini, D. Parker, L. Romagnani, D. Doria, S. Kar, C. Lewis, M. Borghesi, and H. Palmans, Laser Part. Beams **29**, 231 (2011).

[24] J. Pšikal, J. Limpouch, S. Kawata, and A. A. Andreev, Czech. J. Phys. **56**, B515 (2006).

[25] V. Floquet, O. Klimo, J. Psikal, A. Velyhan, J. Limpouch, J. Proska, F. Novotny, L. Stolcova, A. Macchi, A. Sgattoni, L. Vassura, L. Labate, F. Baffigi, L. A. Gizzi, Ph. Martin, and T. Ceccotti, J. Appl. Phys. **114**, 083305 (2013).

[26] M. Manclossi, J. J. Santos, D. Batani, J. Faure, A. Debayle, V. T. Tikhonchuk, and V. Malka, Phys. Rev. Lett. **96**, 125002 (2006).

[27] M. Roth, A. Blazevic, M. Geissel, T. Schlegel, T. E. Cowan, M. Allen, J.-C. Gauthier, P. Audebert, J. Fuchs, J. Meyer-ter-Vehn, M. Hegelich, S. Karsch, and A. Pukhov, Phys. Rev. ST Accel. Beams **5**, 061301 (2002).

[28] M. N. Quinn, D. C. Carroll, X. H. Yuan, M. Borghesi, R. J. Clarke, R. G. Evans, J. Fuchs, P. Gallegos, L. Lancia, K. Quinn, A. P. L. Robinson, L. Romagnani, G. Sarri, C. Spindloe, P. A. Wilson, D. Neely, and P. McKenna, Plasma Phys. Controlled Fusion **53**, 124012 (2011).

[29] G. Cuttone *et al.*, Eur. Phys. J. Plus **126**, 65 (2011).

# Appendix H

# Paper 8

PHYSICAL REVIEW X **6,** 041030 (2016)

# Proton Acceleration Driven by a Nanosecond Laser from a Cryogenic Thin Solid-Hydrogen Ribbon

D. Margarone,[1,*] A. Velyhan,[1] J. Dostal,[2] J. Ullschmied,[2] J. P. Perin,[3] D. Chatain,[3] S. Garcia,[3] P. Bonnay,[3] T. Pisarczyk,[4] R. Dudzak,[2] M. Rosinski,[4] J. Krasa,[1] L. Giuffrida,[1] J. Prokupek,[2] V. Scuderi,[1,6] J. Psikal,[1,5] M. Kucharik,[5] M. De Marco,[1] J. Cikhardt,[2,5] E. Krousky,[2] Z. Kalinowska,[4] T. Chodukowski,[4] G. A. P. Cirrone,[6] and G. Korn[1]

[1]*Institute of Physics ASCR, FZU, ELI-Beamlines project, Prague 182 00, Czech Republic*
[2]*Institute of Plasma Physics ASCR, PALS Laboratory, Prague 182 00, Czech Republic*
[3]*CEA INAC-SBT, Grenoble 38000, France*
[4]*Institute of Plasma Physics and Laser Microfusion, Warsaw 01-497, Poland*
[5]*FNSPE/FEE, Czech Technical University, Prague 166 36, Czech Republic*
[6]*Laboratori Nazionali del Sud, INFN, Catania 95125, Italy*

(Received 2 April 2016; revised manuscript received 27 September 2016; published 8 November 2016)

A high-power pulsed laser is focused onto a solid-hydrogen target to accelerate forward a collimated stream of protons in the range 0.1–1 MeV, carrying a very high energy of about 30 J (~5% laser-ion conversion efficiency) and extremely large charge of about ~0.1 mC per laser pulse. This result is achieved for the first time through the combination of a sophisticated target system ($H_2$ thin ribbon) operating at cryogenic temperature (~10 K) and a very hot H plasma (~300 keV "hot electron" temperature) generated by a subnanosecond laser with an intensity of ~$3 \times 10^{16}$ W/cm$^2$. Both the H plasma and the accelerated proton beam are fully characterized by *in situ* and *ex situ* diagnostics. Results obtained using the ELISE (experiments on laser interaction with solid hydrogen) $H_2$ target delivery system at PALS (Prague) kJ-class laser facility are presented and discussed along with potential multidisciplinary applications.

DOI: 10.1103/PhysRevX.6.041030 Subject Areas: Plasma Physics

## I. INTRODUCTION

Hydrogen is the most abundant element in the Universe; however, it is rarely present in the solid state where it shows a hexagonal close-packed structure. Solid hydrogen was produced in the laboratory for the first time by Dewar decreasing the temperature below hydrogen's melting point (~14 K) [1]. The interior of gas giant planets (e.g., Jupiter) is at extremely high pressure, and this condition allows for the conversion of solid molecular hydrogen ($H_2$) into its metallic form. Although it was predicted over 70 years ago [2], the observation of the insulator-to-metal transition in solid $H_2$ still remains one of the great challenges of condensed-matter physics [3]. The first combination of cryogenic solid $H_2$ and intense laser pulses is reported in Ref. [4], where isolated filaments of solid hydrogen (few mm in diameter and few mm long) were irradiated with a laser and generated a plasma with an electron energy of about 200 eV and proton energy of about 1 keV. Other experiments were performed using a thick solid-hydrogen target irradiated by 18-ns ruby laser pulses generating H plasma in the backward direction [5]. Cryogenic targets have also been widely used for the generation of laser-driven extreme ultraviolet (XUV) sources for lithography and microscopy [6].

In view of the prospects offered by emerging acceleration mechanisms and the motivations provided by important applications, including the potential use in hadron therapy of cancer or fast ignition for inertial confinement fusion, laser-driven proton acceleration has attracted growing attention from the scientific community [7,8]. Target normal sheath acceleration (TNSA), which is the most experimentally investigated laser acceleration mechanism, currently enables the production of proton beams with maximum energies of 60–85 MeV [9]. The beams typically have broad energy spectra; however, monoenergetic features in laser-driven proton beams have been shown experimentally [10].

Multidisciplinary applications, especially medical ones, have stringent requirements for laser-accelerated protons, such as high-energy (60–250 MeV), high average current (in principle achievable by using 1–10-Hz lasers), target purity, repeatable generation, and monochromaticity. While the progress towards such requirements will be facilitated by the development of next-generation laser facilities, equally important advances can be made by developing novel target media specifically tailored to advanced acceleration regimes. The characteristics required of such a target are that it be thin (1–50 $\mu$m), relatively low density ($5 \times 10^{20}$–$5 \times 10^{22}$ cm$^{-3}$) and capable of producing only protons (with no contaminants) and of operating at a high repetition rate as both refreshable and debris free. For this

---

[*] Corresponding author.
daniele.margarone@eli-beams.eu

*Published by the American Physical Society under the terms of the Creative Commons Attribution 3.0 License. Further distribution of this work must maintain attribution to the author(s) and the published article's title, journal citation, and DOI.*

reason, cryogenic hydrogen is currently being considered and several approaches are being explored and developed ranging from *in situ* growth of solid-hydrogen slabs (which are typically millimeters thick and require controlled thermal evaporation to access thinner target regimes) [11] to cylindrical jets of few $\mu$m in diameter [12].

The ELISE (experiments on laser interaction with solid hydrogen) target delivery system, which is the result of a joint development carried out at CEA Grenoble, employs an alternative approach that provides a continuous flow of thin laminar targets of solid hydrogen with a very well controlled and tunable thickness in the tens of $\mu$m range [13]. This type of sophisticated target system is used here for the first time with a high-power laser (nanosecond and low contrast) to accelerate proton beams propagating forward with a maximum energy of ~1 MeV and with a total charge on the order of 0.1 mC per laser pulse, thus demonstrating a very high laser-ion conversion efficiency (~5% in the 0.1–1 MeV range), which is twice that of the total charge and efficiency of plastic targets irradiated in similar experimental conditions. Besides the energy and number of accelerated protons, our measurements aim to characterize, for the first time, the interaction of a high-energy (kJ-class), long (subnanosecond), low-intensity contrast ($10^{-6}$–$10^{-1}$ at 1.3–0.3 ns prior the main pulse intensity) with a solid-hydrogen planar target. The results achieved in the experimental campaign at PALS (Prague) are extensively described and discussed. Particular attention is paid to technological issues that would be encountered in a high-energy Petawatt (PW) system [e.g., tolerance to electromagnetic pulse (EMP), vacuum compatibility, effects of prepulse] along with the future possible usage of ELISE at emerging PW-class, high repetition rate laser facilities.

## II. CRYOGENIC SOLID HYDROGEN THIN RIBBON

The ELISE cryogenic target delivery system designed and developed at the Low Temperature Laboratory of CEA enables the production of the continuous flow of a solid-$H_2$ slab (ribbon) through a newly designed extrusion apparatus that does not contain any movable parts. The thermodynamic properties of a $H_2$ fluid are used to generate a pressure rise in a cell and push the solid $H_2$ out through a calibrated nozzle. The solid-$H_2$ ribbon has a 1-mm width, controllable thicknesses (20–100 $\mu$m) depending on the nozzle employed, and an electron density of $5.36 \times 10^{22}$ cm$^{-3}$ (steplike).

The experimental cell for the solid-$H_2$ ribbon production is equipped with two heat exchangers, one situated at its base (E1) and another one situated at its top (E2), enabling the cell to achieve the required temperature values, as schematically shown in Fig. 1(a). The temperature of E1 ($T_1$) is regulated below the triple point of the gas (i.e., below 13 K for $H_2$) and the temperature of E2 ($T_2$) is regulated above it (typically 20 K). When the valve V1 is opened, $H_2$ enters the cell and immediately condenses, thus blocking the extrusion nozzle. The cell is completely filled

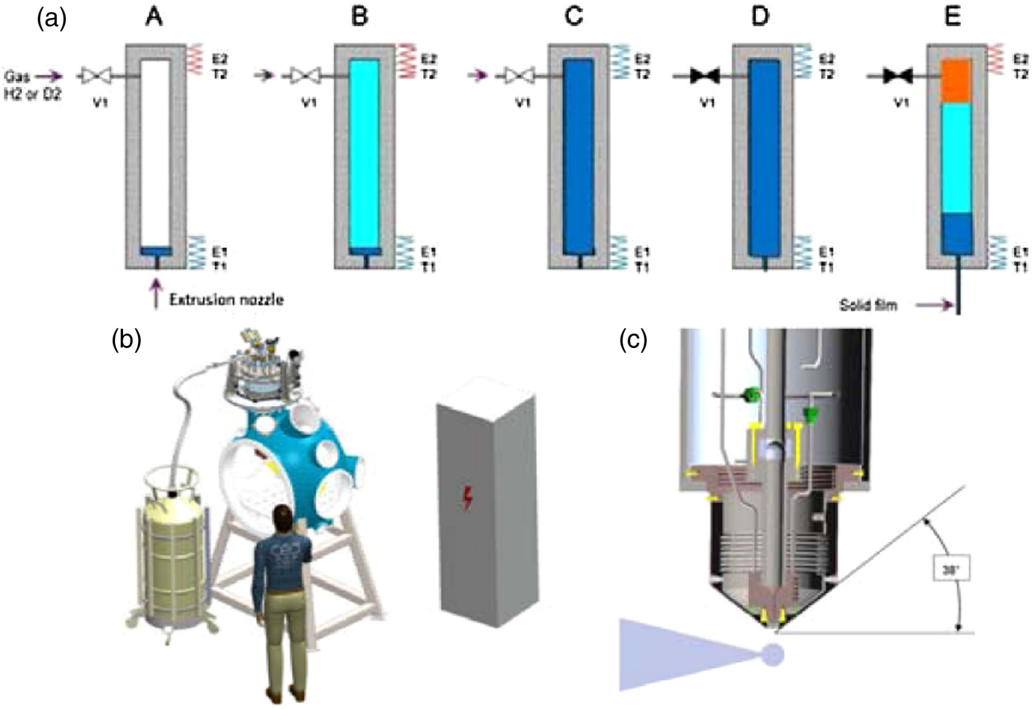

FIG. 1. (a) Different phases of the solid $H_2$ ribbon generation, (b) scheme of the ELISE installation at PALS, (c) sketch of the ELISE nozzle.

with liquid hydrogen ($T_2$ is regulated above the triple point), then $T_2$ is decreased slowly below the triple point in order to fill the cell completely with solid $H_2$ and the valve is closed. Finally, $T_2$ is increased to generate a pressure rise in the cell ($T_1$ is regulated close to the triple point) and solid $H_2$ is extruded through the nozzle. The solid $H_2$ extrusion speed can be regulated close to 10 mm/s by precisely controlling $T_1$ and $T_2$. The solid film then evaporates under the effect of heat radiation, being finally evacuated by a pumping system. More details about the ELISE working principle and functional tests performed at CEA are reported in Ref. [13].

The main parts of the ELISE installation are shown in Fig. 1(b): (i) a cryostat cooled with liquid helium through a transfer line connected to a liquid helium Dewar, (ii) an electrical cabinet situated close to the experimental chamber, (iii) an *ad hoc* electrical shielding system to prevent disturbances from EMP during high-energy laser-matter interaction, and (iv) a differential pumping system ($10^{-5}$–$10^{-4}$ mbar). The aperture of the cone close to the nozzle is 38 deg on both sides (incoming laser and outgoing proton beam) as shown in Fig. 1(c).

## III. EXPERIMENTAL SETUP AT PALS SUBNANOSECOND LASER FACILITY

The experiment is performed at the Prague Asterix Laser System (PALS) facility in Prague [14], using the kJ-class (up to 600 J in our experiment), subnanosecond (0.3-ns FWHM), and linearly polarized laser beam. The laser pulse is focused into a focal spot of 80 $\mu$m by an $f = 2$ spherical lens to reach a nominal intensity of $3 \times 10^{16}$ W/cm$^2$ on the target in vacuum conditions of $10^{-5}$–$10^{-4}$ mbar. The solid-H ribbon (62 $\mu$m thick, 1 mm wide) is irradiated by the laser with normal incidence to the ribbon surface. The ns-long laser pulse temporal shape reported in Fig. 2(a) shows that although approximately 500 J are contained in the main pulse (300 ps at FWHM), the residual laser energy (about 100 J) is stored in the nanosecond pedestal. Thus, around 50 J of the pulse energy is delivered on target before the maximum intensity peak is reached and, as a consequence, generates a typical preplasma. Figure 2(a) shows the presence of three intensity regions: the 0-I region represents the low-intensity ($3 \times 10^{10}$ W cm$^{-2}$) laser precursor, I-II is the medium intensity (up to $10^{15}$ W cm$^{-2}$) pedestal, and II-III is the high-intensity (nominally up to $3 \times 10^{16}$ W cm$^{-2}$) main pulse.

Besides setting up plasma and ion diagnostics, a series of basic experimental tests (vacuum and electrical) are performed to check the working functionalities of the ELISE target delivery system when operating in a harsh laser plasma environment. In fact, high-energy laser-matter interaction typically generates a giant EMP associated with electron oscillations on a target inside the PALS vacuum chamber [15], which can cause several issues for real-time detectors commonly used for laser-generated plasma characterization. A typical EMP signal detected by a $B$ probe (placed 26 cm from the target and registered with a 6-GHz oscilloscope having 25-GS/s sampling rate) is shown in Fig. 3(a). The signal's maximum amplitude is about 130 V and is reached at the beginning of the laser-target interaction. The fast Fourier transform (FFT) of the EMP signal reported in Fig. 3(b) shows a number of frequency domains ranging from 100 MHz to 3 GHz. Although various electronic components are part of the ELISE system, the giant EMP signal amplitude did not interfere with the correct operation of the cryogenic device, mainly thanks to the optimal electrical shielding design.

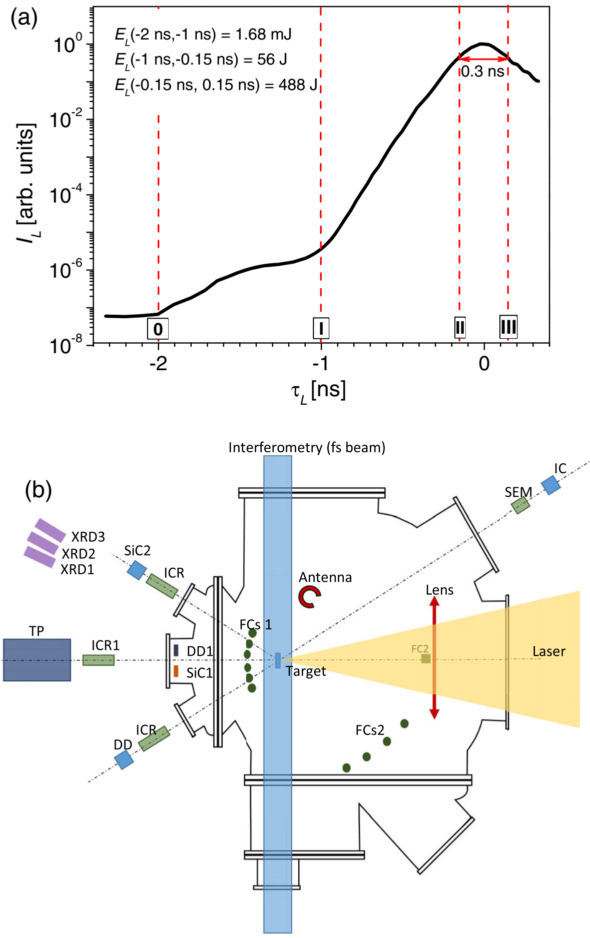

FIG. 2. (a) PALS laser temporal profile: intensity ($I_L$) in arbitrary units (the laser-energy $E_L$ content in different time windows is reported in the caption) versus time ($\tau_L$). (b) Sketch of the setup used in the experiment with the H target (top view).

Finally, the pressure value in the vacuum chamber is monitored during ELISE continuous operation and the vacuum level is found to be fully compliant with the experimental needs, especially in terms of required pressure for typically used ion diagnostics ($10^{-5}$–$10^{-4}$ mbar).

Ion analyzers, such as a calibrated Thomson-parabola (TP) spectrometer (equipped with imaging plates), ion collectors (IC or ICR) [16], silicon-carbide (SiC) detectors,

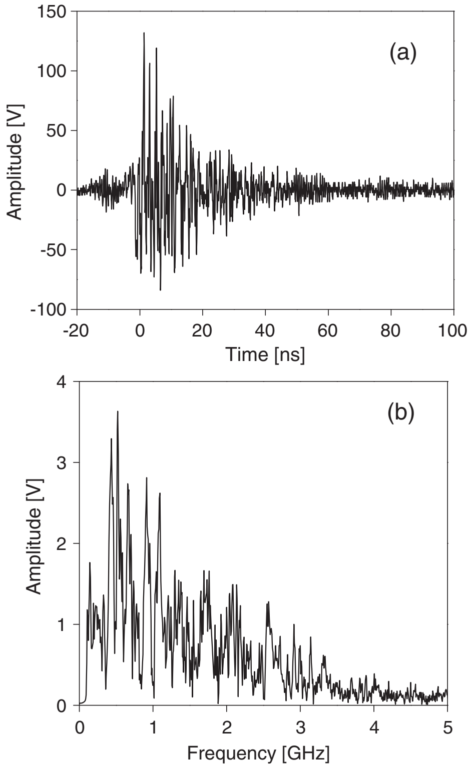

FIG. 3. Amplitude of the EMP signal measured with a $B$ probe placed 26 cm from the laser-target interaction point (a) and corresponding frequency spectrum (b).

and diamond detectors (DD) [17], as well as small Faraday cups (FC) [18], placed at various distances and directions, as schematically shown in Fig. 2(b), are used to detect and characterize the accelerated proton beams in terms of energy and angular distributions.

Figure 4(a) shows a typical TP spectrometer snapshot where protons, carbon ions, and other contaminants (oxygen, nitrogen, etc.) are detected when a plastic target ($CH_2$) is irradiated with the PALS laser. In contrast, only protons (pure H plasma coming from the high purity of the $H_2$ gas) are accelerated from the H target, as reported in Fig. 4(b). This TP spectrum confirms that the cryogenic H target and, as a consequence, the produced hydrogen plasma are free of any contaminants that are present on the surface of metallic or plastic foils typically used in the TNSA acceleration regime. The TOF spectra measured for the same laser shot with the H target by SiC and IC are shown in Fig. 4(c), along with the TP signal recalculated in TOF at an equivalent detection distance of 1.75 m. The SiC and the DD are more suitable to detect fast (energetic) protons as described in Ref. [17] compared to IC; in fact, the TOF signal around 200 ns [see Fig. 4(c)] is much more pronounced in the case of SiC. The photopeak ascribable to the XUV plasma radiation (present in all the used detectors) is measured almost instantaneously and is used as a trigger signal.

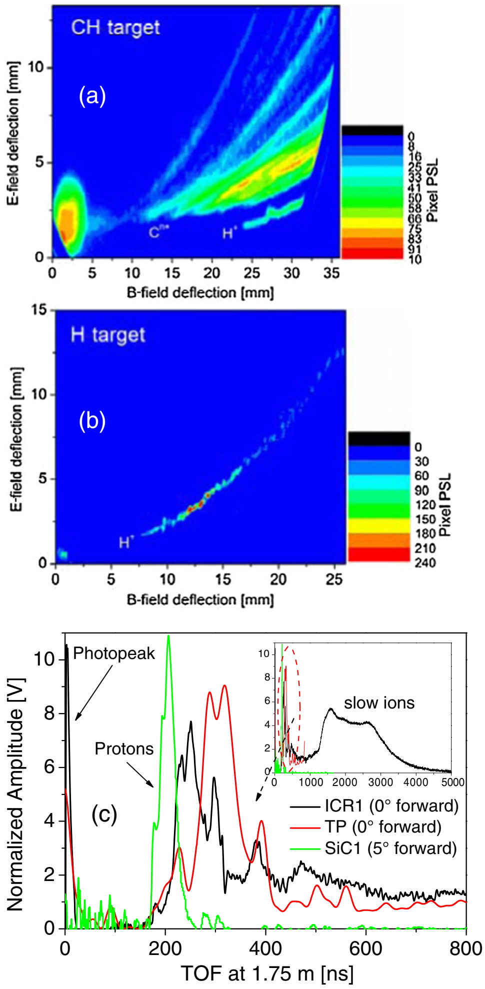

FIG. 4. (a) TP snapshot showing the typical signal from a plastic target (presence of protons, carbon, and other ions), where PSL is the photo-stimulated luminescence value. (b) TP snapshot showing the exclusive presence of protons for the H target (pure H plasma). (c) TOF spectra detected by ICR1, SiC1, and TP (recalculated at a distance of 1.75 m). The inset shows the slow ion TOF signal present up to 5 $\mu$s.

A Ti:sapphire laser system having a wavelength of 808 nm and pulse duration of 40 fs is used to carry out time-resolved measurements that enable the determination of plasma density distribution through a three-frame interferometric system previously optimized and normally used at PALS [19]. The three frames are recorded successively with a time delay of 1 ns. The 2D plasma density profiles are used to measure the plasma electron density and, as a consequence, the number of slow protons in the laser produced plasma propagating both forward and backward.

Three scintillation detectors for hard x rays (HXR1, HXR2, HXR3) are placed 3 m from the target and at 45 deg with respect to the target normal in the forward direction, as sketched in Fig. 2(b). These detectors are described in detail in Ref. [20]. The HXR1-3 detectors are shielded by interlocked lead bricks of 5 cm thickness, and by 5, 10, and 15 cm of lead shield at their front, respectively. Moreover, since the sensitivity of each detector is slightly different, they are cross-calibrated using the same Pb shielding (5 cm) in front of all detectors in a few dedicated shots. The HXR measurements are important for the estimation of the so-called "hot electron" temperature assuming that hard x rays are produced as bremsstrahlung radiation of such electrons, as described in Ref. [21].

## IV. RESULTS AND DISCUSSION

Four raw interferometric snapshots recorded through the optical interferometry technique, using the fs-class Ti:sapphire laser as a probe beam, are reported in Fig. 5. They show the H-plasma expansion for the same laser shot at four different times with respect to the arrival of the main laser pulse: −0.2 ns [Fig. 5(a)] and −0.07 ns [Fig. 5(b)] before the main intensity peak, 0.9 ns [Fig. 5(c)] and 1.9 ns [Fig. 5(d)] after it. The interferometry snapshots [Figs. 5(b)–5(d)] are acquired during the same laser shot, while Fig. 5(a) is acquired during a different laser shot but at very similar laser irradiation conditions. The plasma electron density maps can be retrieved after a proper analysis using the "maximum-of-a-fringe" method [19,22], as shown in Figs. 5(i)–5(n) for the four different time frames; thus, the corresponding axial density profile can be calculated [see plots in Figs. 5(i) and 5(l)–5(n)]. The plasma density ($n_e$) profile on the $z$ axis roughly follows an exponential decay function $(n_e(z)^{1/4}n_0e^{-z/L})$, where $L$ is the density scale length and $n_0$ is the maximum electron density [19,22]. The interferometric measurements show the presence of a preplasma generated on the target front side at about −200 ps (i.e., before the main intensity peak) with a scale length of about 150 $\mu$m. At about −70 ps, a plasma is also generated at the target rear side with a scale length of 200 $\mu$m. The plasma length at the target rear side after 0.9 and 1.9 ns is approximately 600 and 900 $\mu$m, respectively, which corresponds to a bulk plasma expansion velocity of $\sim 5 \times 10^5$ m/s, which identifies the group of slow protons in the H plasma. The group of fast protons with kinetic energy in the range 0.1–1 MeV is not discernable. The estimated plasma electron number, which basically corresponds to the total number of slow protons, is $4 \times 10^{16}$ at the front and $3 \times 10^{16}$ at the rear side of the irradiated target after 1.9 ns with respect to the arrival of the main laser pulse.

The normalized TOF proton signals measured through different ion detectors are summarized in Fig. 6(a). Both ICR1 and TP (placed along the laser axis in the forward direction) show a proton current signal starting slightly after 100 ns, which corresponds to proton energy of approximately 1.2 MeV. On the other hand, DD1 (placed at 5 deg from the laser axis in the forward direction) shows a slightly faster proton signal corresponding to proton

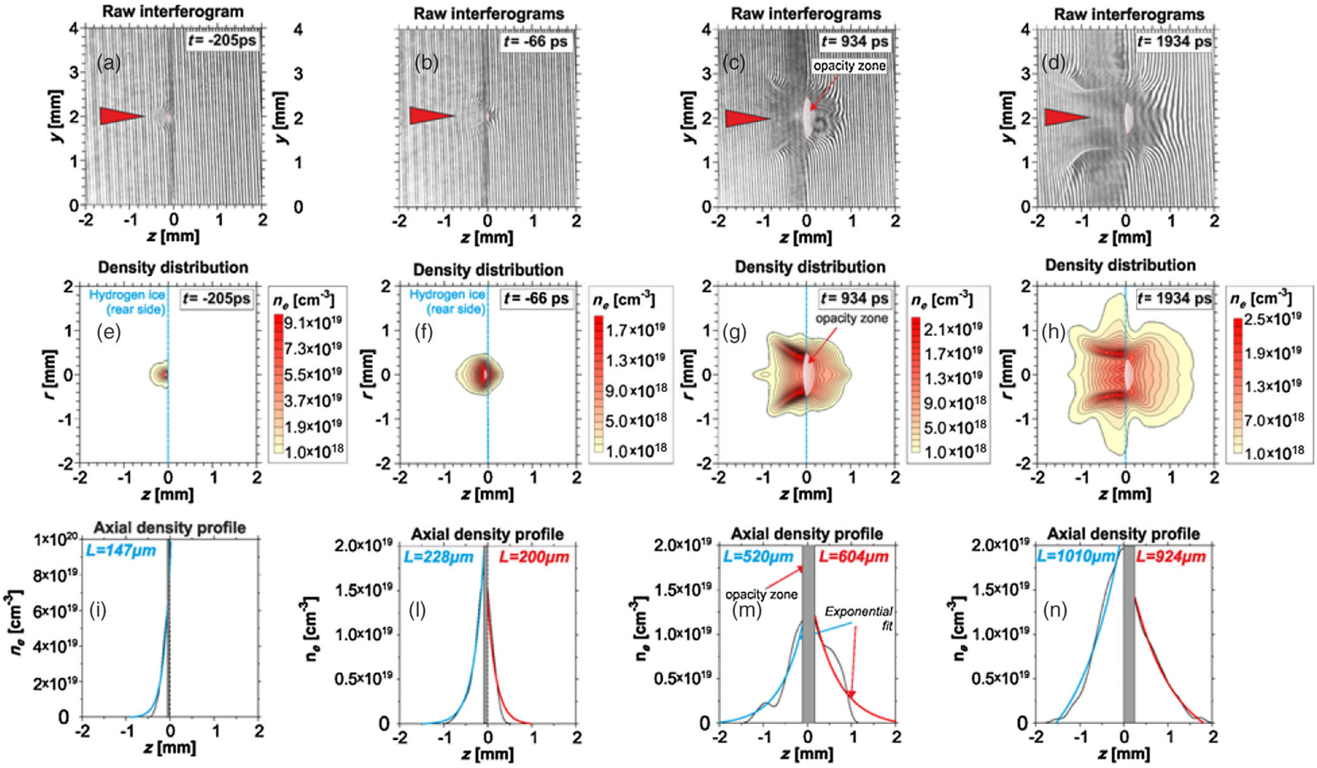

FIG. 5. Raw interferometry snapshots recorded at −0.2, −0.07, 0.9, and 1.9 ns (a)–(d), respectively, corresponding plasma density maps (e)–(h), and axial density profiles (i)–(n). The laser propagates from left to right, as shown by the red arrow.

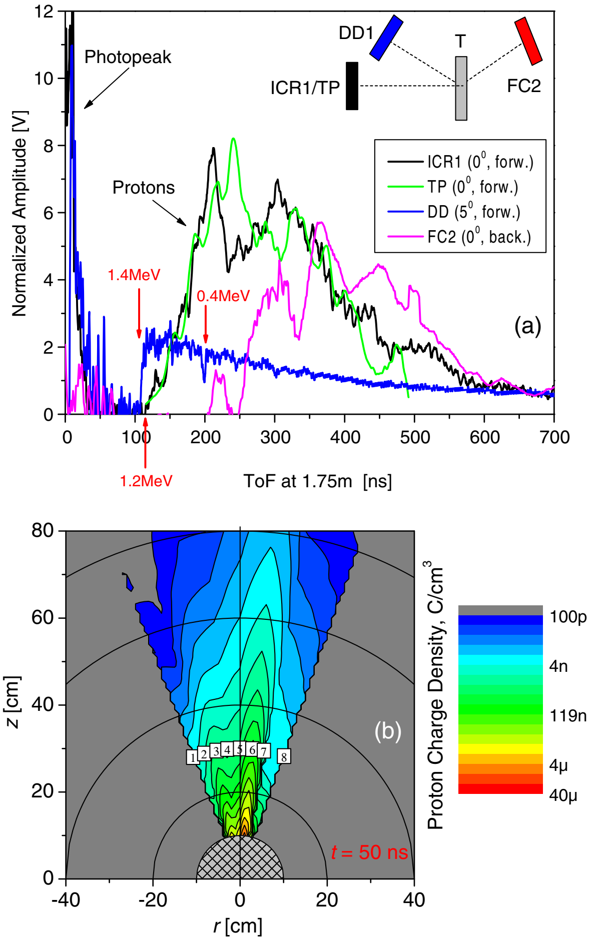

FIG. 6. (a) Normalized TOF signal for the different ion detectors (ICR1, TP, DD1, FC2) used during the same laser shot. (b) Proton angular distribution reconstructed from the eight FCs placed in the forward direction (shown as white squares).

energy of about 1.4 MeV. FC2 (placed at 5 deg from the laser axis in the backward direction) shows a much slower TOF signal at around 200 ns, which indicates proton energy of about 0.4 MeV, thus with a maximum kinetic energy clearly lower than the proton stream propagating forward.

Figure 6(b) shows the proton angular distribution in terms of charge density ($C/cm^3$), which is estimated through the eight FCs placed at various angles in the forward direction [white squares in Fig. 6(b)]. The charge density is derived from the measured ion currents, as presented in Ref. [23]. The maximum ion aperture cone is approximately 25 deg, as shown in the inset of Fig. 7(a), and a small deflection of ~5 deg in the ion stream propagation (with respect to the laser axis) is measured. In fact, the difference shown in the beginning of the proton signal by DD1 compared to ICR1 or TP seems to be ascribable to the abovementioned deflection in the ion emission, since the high-proton energies have a privileged direction of propagation (in this case ~5 deg from the laser axis).

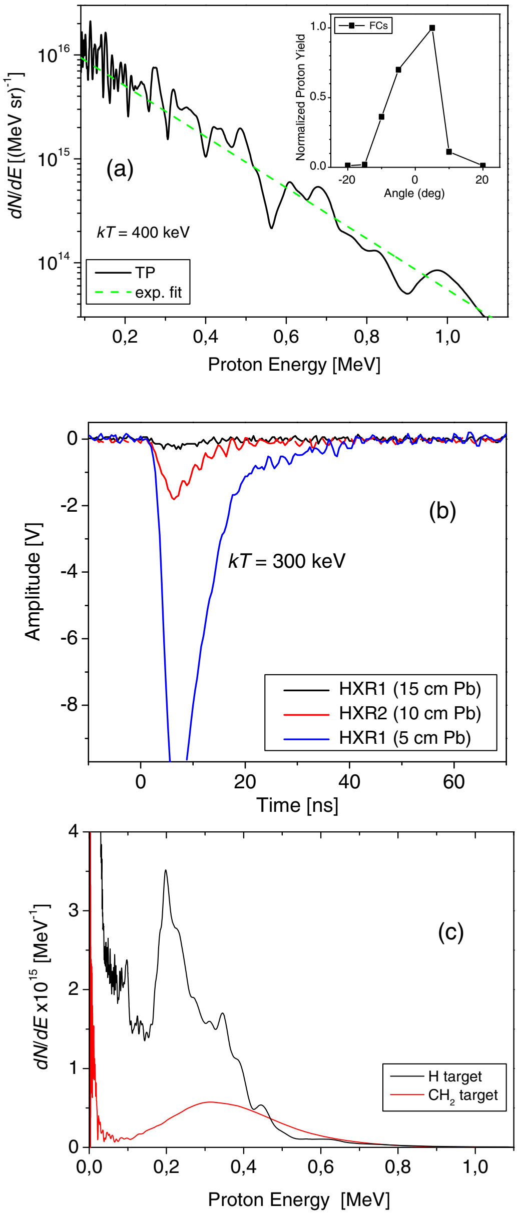

FIG. 7. (a) Proton energy distribution measured with TP (black line) and linear fit (dashed green line) along with the ion angular distribution measured with FCs (see inset). (b) HXR signals measured with the three detectors having different Pb filter thickness (the signal recorded by the detector with a 5-cm Pb shielding is saturated; however, an extrapolation of the signal is used to calculate the hot electron temperature). (c) Proton energy distribution recalculated from TOF spectra acquired with solid-H and $CH_2$ targets in similar laser irradiation conditions.

The TP spectrum is converted in proton energy distribution as reported in Fig. 7(a). A cone of ~25 deg for the accelerated proton stream angular distribution is measured by the small FCs placed behind the target [shown in the inset of Fig. 7(a)]. The $\gamma$-ray signals measured by the HXR plastic scintillators (shielded with three different Pb filters)

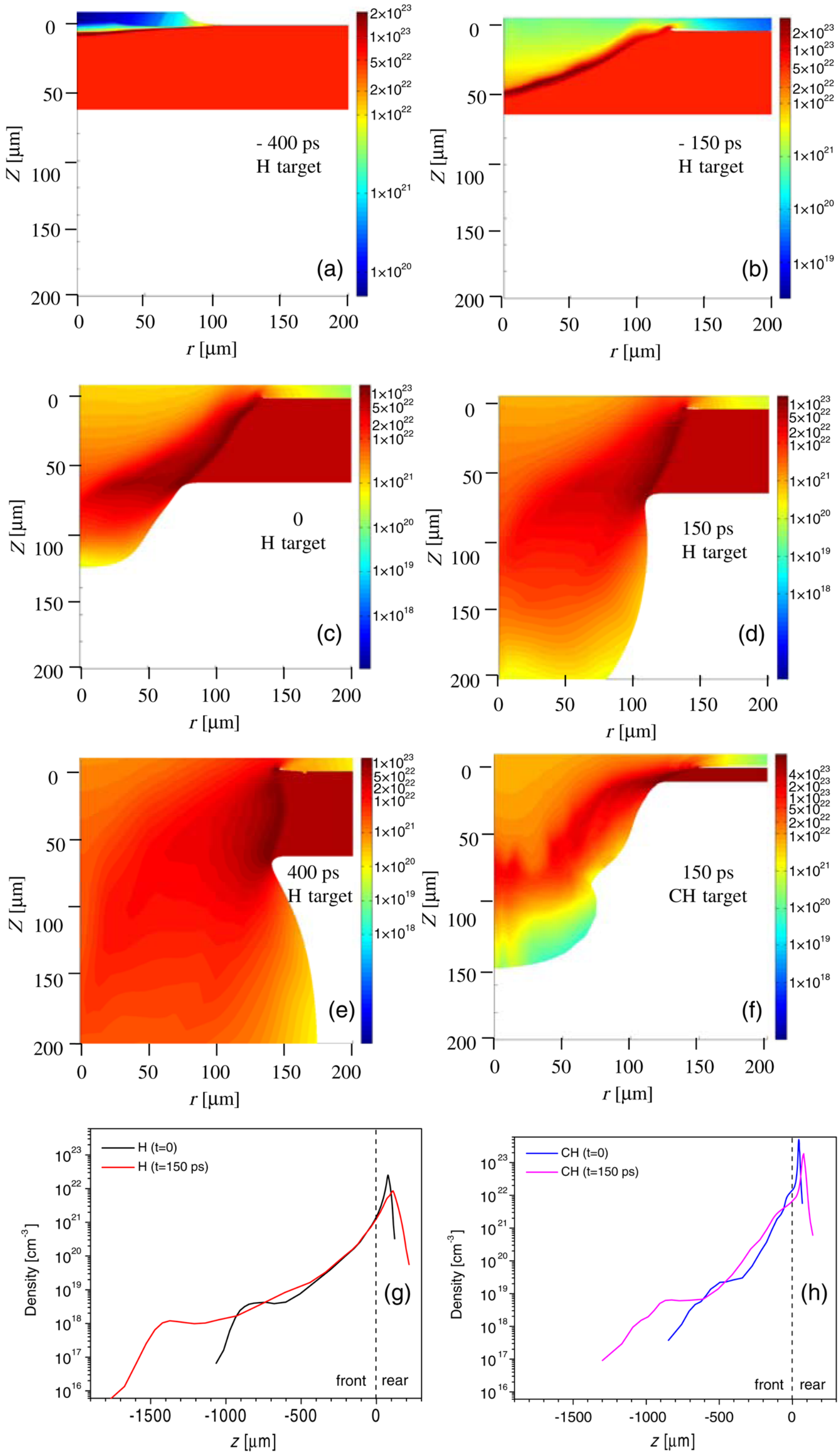

FIG. 8. Hydrodynamic simulation outputs showing the electron density profiles for the H target at different times after the main laser peak intensity (a)–(e) and for the CH target at 150 ps (f). The laser beam propagates from the top along the $z$ axis. The electron density profiles along the $z$ axis at 0 and 150 ps are shown in (g) and (h), respectively, for the H and $CH_2$ targets.

for the same laser shot are shown in Fig. 7(b). The signal recorded by the detector with a 5-cm Pb shielding is saturated; however, an extrapolation of the signal is used to calculate the hot electron temperature ($kT_{\mathrm{hot}}$). The temperature estimated from the HXR spectra analysis is approximately 300 keV, which is in good agreement with the value calculated through the exponential fit of the TP proton energy distribution (~400 keV) shown as a dashed line in Fig. 7(a). This hot electron temperature estimation fits very well the measured maximum proton energy ($E_{\mathrm{max}} \sim 1.4$ MeV), as predicted by experimental scaling laws ($E_{\mathrm{max}} \sim 4.5kT_{\mathrm{hot}}$) reported in Ref. [24].

The maximum proton energy measured with the solid-H target is in agreement with our previous results using metallic, semiconductor, and plastic foils at PALS [25]. However, the number of protons propagating forward with energy of 0.1–1 MeV is enhanced by about a factor of 3 (from $2 \times 10^{14}$ to $6.5 \times 10^{14}$) compared to a plastic ($CH_2$) target having a thickness of 10 $\mu$m, which roughly corresponds to the areal density of the used H target. The proton number is enhanced by about a factor of 4 for protons having energies between 150 and 400 keV (from $1.1 \times 10^{14}$ to $4.8 \times 10^{14}$), as clearly shown in Fig. 7(c). The estimated total energy for the collimated proton beam with energies of 0.1–1 MeV, which are accelerated by the subnanosecond laser into the forward direction, is about 30 J, and the corresponding laser-proton acceleration efficiency $\eta$ (ratio between the total proton beam energy and the incoming laser energy) is about 5%.

We carry out hydrodynamic simulations for both the H and $CH_2$ targets, in order to obtain important information about the interaction physics and the peculiarity in laser ablation with the given temporal profile provided by the PALS system having a low laser intensity contrast [see Fig. 2(a)]. Such simulations are mainly used to model the evolution of the plasma electron density, especially at early stages of the laser-matter interaction. However, hydrodynamic simulations cannot properly describe the acceleration mechanism close to the main laser peak intensity ($>10^{16}$ W/cm$^2$) where hot electrons (responsible for the acceleration of protons with the highest energies) are generated and kinetic effects (potentially responsible for laser absorption enhancement) are expected. The 2D PALE (Prague arbitrary Lagrangian-Eulerian) hydrodynamic code working in cylindrical geometry is used [26]. This code employs the compatible staggered Lagrangian numerical scheme [27], the quotidian equation of state (QEOS), and a rezoning or remapping mechanism improving the robustness of the simulations [28]. The thermal conductivity is treated using a mimetic method with the standard Spitzer-Harm heat conductivity coefficient and heat flux limiter. Ray tracing is used for the laser absorption modeling. A thickness of 10 $\mu$m is chosen for the $CH_2$ target to keep the same areal density as the 62-$\mu$m-thick H target. The outputs of our hydrodynamic simulations are shown in Fig. 8. The maximum electron density for the H plasma is more than a factor of 20 lower than the one of the CH plasma during the whole laser interaction. Furthermore, the electron density values at the focal plane ($\mathrm{FP} = 0$) at two different times for both targets show an enhancement of the relative ratio between the CH- and the H-plasma densities from 10 at the main peak intensity ($t = 0$) to 5 at the FWHM value of the laser intensity ($t = 150$ ps). In particular, the CH-plasma electron density at the focal plane (where the laser intensity is maximized) is about $1.3 \times 10^{22}$ and $6 \times 10^{21}$ cm$^{-3}$ at 0 and 150 ps, respectively. On the other hand, the H-plasma electron density at the focal plane is about $1.3 \times 10^{21}$ cm$^{-3}$, independent of time, thus showing that the laser pulse constantly interacts with a "quasisteady" near-critical density plasma (approximately 2 times the critical density), while the CH plasma always shows an overcritical density, even for longer times. Such numerical results suggest a potential enhancement of the laser absorption at the highest intensities ($>10^{16}$ W/cm$^2$), which involves a larger plasma volume in the case of the H target, thus leading to a higher proton acceleration efficiency, as measured experimentally. On the other hand, in the case of the $CH_2$ target, the laser is entirely absorbed at the target front side.

## V. CONCLUSIONS AND PERSPECTIVES

In this paper, we present and discuss the first experimental results obtained through irradiating a cryogenic thin (62-$\mu$m) solid-hydrogen ribbon with a high-power laser. The investigation of such a system is potentially interesting for condensed-matter physics, e.g., through H spectroscopy studies at extreme conditions (high pressure and high temperature gradient) [29].

The generation of pure hydrogen plasma has advantages from the experimental point of view in terms of plasma generation and characterization, as well as for future multidisciplinary applications of laser-accelerated proton beams, since such a target delivery system can potentially be used at high repetition rates and is essentially debris free. Furthermore, clear benefits for theoretical modeling and numerical simulations are evident. In fact, H plasma can be considered as an ideal sample for theoretical investigations and their experimental verification both in terms of accuracy (a lower number of approximations is needed) and also reduced computational time for modeling [especially with particle-in-cell (PIC) codes for femtosecond and picosecond laser-matter interaction].

This target delivery system has been used on the PALS laser (long pulse, high energy but moderate intensity), which is not the ideal system for reaching high proton energies; however, using ELISE on this laser system requires the solution of similar technological issues that would be encountered on a high-energy PW system (e.g., tolerance to EMP, vacuum compatibility, effects of prepulses). Thin ribbons down to 25 $\mu$m have already been produced; however, the stability of the target along the laser propagation axis has to be improved in terms of shot-to-shot fluctuations, for instance, using a simple technical solution where a mechanical "guide" is placed under the nozzle in order to "channel" the H ribbon and to limit its oscillations. Nevertheless, the shot-to-shot fluctuations measured in our experiment ($\pm 25\ \mu$m along the laser axis) do not affect our experimental results; in fact, we estimate a very small difference in the angle between the laser axis and the target normal due to such spatial fluctuations ($<0.4°$), which does not affect the proton beam features in terms of directionality and maximum energy. The technological solutions employed to operate the ELISE cryostat allow, in principle, the production of H ribbons with thickness down to 5 $\mu$m. The production of lower thickness ribbons (1 $\mu$m or less) can potentially be achieved using a slightly different geometry where the hydrogen ribbon is partially evaporated just before the laser shot through the interaction with a synchronized low-energy laser operating at a wavelength of around 2 $\mu$m, which is the range of maximum absorption for hydrogen.

Our experimental achievements with the ns-class, low-contrast PALS laser demonstrate that a very high total energy of about 30 J is carried by the forward accelerated collimated proton stream to which corresponds a laser-proton acceleration efficiency of ~5% in the 0.1–1 MeV energy range (2–3 times higher than standard plastic foils in the same irradiation conditions), and a proton beam charge of ~0.1 mC per laser pulse. Such efficient proton acceleration is ascribable to volumetric effects in the near-critical density H plasma along the entire target thickness. Although so-called "collisionless shock acceleration" has been shown as a result of the interaction of 10–100-ps laser pulses with a near-critical density target [30], this regime is excluded in our case, since our experiment shows a much higher proton yield compared to Ref. [30]. Moreover, the maximum laser intensity in our experiment is relatively low (corresponding to $a_0 = 0.2$); thus, the resulting hole-boring velocity associated with the ponderomotive force is also low, both for the fully ionized solid density H target (approximately $5 \times 10^{-4}c$) and for the H-plasma density at the laser peak intensity ($3 \times 10^{-3}c$, where $c$ is the speed of light). This would result in proton energies below 1 keV and approximately 20 keV, respectively, estimated by taking into account that the shock velocity is close to the hole-boring velocity [7].

Although a proton acceleration conversion efficiency of 15% was experimentally achieved by Brenner *et al.* for energies of 5–30 MeV using two temporally separated 800-fs laser beams and 5-$\mu$m-thick Au foil (45 deg incidence angle and $p$ polarization) [31], our experimental achievement (5% conversion efficiency for the forward accelerated proton beam in the 0.1–1 MeV energy range) has never been reached with ns-class lasers operating at moderate laser intensities. This result can potentially be improved upon if a ps-class laser system is used. In fact, based on our PIC simulations in the fs regime (see Fig. 9), the ion acceleration efficiency with a low-density solid-H target can reach values of about 25%. Thus, an approximation of 20% for the laser-to-proton acceleration efficiency can be considered if the target thickness is optimized for the specific ps-laser system temporal characteristics. In principle, our experimental achievements might support novel scenarios for the fast ignition scheme where, as suggested in Ref. [32], a collimated laser-generated proton beam is used to induce ignition in a precompressed DT fuel (400 $\mathrm{g/cm^3}$) with a standard inertial confinement fusion (ICF) geometry. Various theoretical works indicate a preference for relatively low proton energies (~10 MeV) at a fuel temperature of a few keV, having a proton bunch duration of several ps (required for the fast ignition scheme) and ~10 kJ total proton beam energy [33]. In the case of the investigated H target, assuming a laser-proton acceleration efficiency of ~20%, the required ps-class laser system should deliver energy of ~50 kJ and moderate laser intensity on target to achieve ignition.

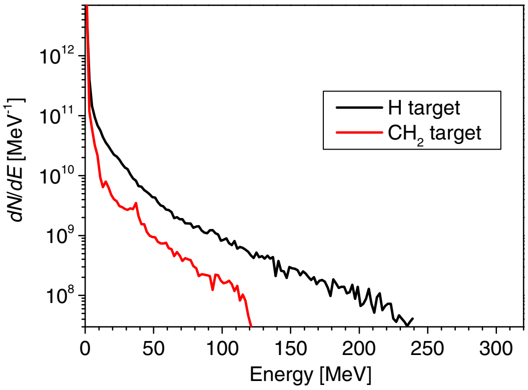

FIG. 9. Proton energy distributions calculated through PIC numerical simulations for different targets with a thickness of 5 $\mu$m and for a laser intensity of $\sim 6 \times 10^{21}$ $\mathrm{W/cm^2}$.

In order to explore the direction in which the use of a cryogenic hydrogen target could develop, especially in terms of multidisciplinary applications of laser-driven proton beams, we perform preliminary 2D PIC simulations using the EPOCH code at ultrahigh laser intensities [34]. Laser parameters relevant to the future 10-Hz, PW-class, 800-nm laser system available at ELI-Beamlines [35] are used; thus, the laser peak intensity is $6 \times 10^{21}$ $\mathrm{W/cm^2}$ (18-J laser energy on target, 3-$\mu$m FWHM focal spot diameter, 30-fs laser pulse duration, normal incidence irradiation angle). Fully ionized solid density H and $CH_2$ targets are considered with a thickness of 5 $\mu$m. The cell size is $20 \times 20$ $\mathrm{nm}^2$, and each cell contains 62 macroelectrons for the H foil and 400 macroelectrons for the $CH_2$ foil. A corresponding number of macroions is used in order to ensure plasma charge neutrality; moreover, all particles have the same numerical weights. The comparison between 5-$\mu$m-thick solid-H foil and 5-$\mu$m-thick plastic ($CH_2$) foil is shown in Fig. 9. The use of 5-$\mu$m-thick solid H seems to cover the entire "clinical window" for cancer therapy in terms of proton energy (60–250 MeV), thus clearly showing the potential of this low-density cryogenic target compared to standard solid foils. Furthermore, such a target seems to be ideal for future application in laser-driven proton therapy due to the high purity and the high proton beam charge per laser pulse (∼15 nC for proton energies higher than 60 MeV). The clear advantage of the proposed target, which is demonstrated experimentally in the ns regime, i.e., the energy coupling into energetic particles, is also confirmed by our numerical simulations performed in the fs regime. In fact, a very high laser-to-proton conversion efficiency of ∼25% is estimated for the H target for energies higher than 5 MeV, in comparison to ∼10% calculated for the $CH_2$ target. This result is linked to the laser absorption along the overall target thickness, which is strongly enhanced (∼70% for the H target and ∼30% for the $CH_2$ target). Moreover, electrons are heated more efficiently (∼25 MeV for the H target and ∼20 MeV for the $CH_2$ target) within the whole H-foil volume thanks to a more efficient hole-boring mechanism. In fact, for the H target, the hole-boring velocity is substantially higher due to its lower density in comparison to the $CH_2$ foil (more than a factor of 6) and to the lower ion mass in the generated plasma (only H is present in the cryogenic target, but C is also present in the plastic foil), thus leading to a different regime of laser-target interaction and to substantial enhancement of the laser absorption.

## ACKNOWLEDGMENTS

The authors acknowledge the following scientific and technical personnel who provided additional support to the different teams involved in this experimental work: M. Pfeifer, J. Skala, J.M. Mathonnet, T. Lastovicka, M. Kozlova, J. Hrebicek, J. Kovar, M. Jantac, K. Brabcova, M. De Napoli, N. Randazzo, and R. Jack. This research was mainly sponsored by the project ELI - Extreme Light Infrastructure–Phase 2 (CZ.02.1.01/0.0/0.0/15_008/0000162) through the European Regional Development Fund, by the Ministry of Education, Youth and Sports of the Czech Republic (National Program of Sustainability II Project No. LQ1606, PALS RI Projects No. LM2010014 and No. LM2015083, COST Project No. LD14089), and by the Czech Science Foundation (Projects No. 15-02964S and No. P205-11-P712). Computational resources were provided by the CESNET LM2015042 and the CERIT Scientific Cloud LM2015085, provided under the program "Projects of Large Research, Development, and Innovations Infrastructures".

[1] J. Dewar, *Sur la Solidification de l'Hydrogene*, Ann. Chim. Phys. **18**, 145 (1899).

[2] E. Wigner and H. B. Huntington, *On the Possibility of a Metallic Modification of Hydrogen*, J. Chem. Phys. **3**, 764 (1935).

[3] S. Deemyad and I. F. Silvera, *Melting Line of Hydrogen at High Pressures*, Phys. Rev. Lett. **100**, 155701 (2008).

[4] P. A.H. Saunders, P. Avivi, and W. Millar, *Laser Produced Plasmas from Solid Hydrogen Targets*, Phys. Lett. **24A**, 290 (1967).

[5] P. Mulser, R. Siger, and S. Witkowski, *Plasma Production by Laser*, Phys. Rep. **6**, 187 (1973).

[6] F. Jin, K. Gabel, M. C. Richardson, M. Kado, A. F. Vasilev, and D. Salzmann, in *Applications of Laser Plasma Radiation SPIE Proceedings* Vol. 151 (SPIE-International Society for Optical Engineering, Bellingham, WA, 2015); M. Berglund, L. Rymell, H. M. Hertz, and T. Wilhein, *Cryogenic Liquid-Jet Target for Debris-Free Laser-Plasma Soft X-Ray Generation*, Rev. Sci. Instrum. **69**, 2361 (1998); R. Lebert, G. Schriever, T. Wilhein, and B. Niemann, *Soft X-Ray Emission of Laser-Produced Plasmas Using a Low-Debris Cryogenic Nitrogen Target*, J. Appl. Phys. **84**, 3419 (1998).

[7] A. Macchi, M. Borghesi, and M. Passoni, *Ion Acceleration by Superintense Laser-Plasma Interaction*, Rev. Mod. Phys. **85**, 751 (2013).

[8] S. V. Bulanov and V. S. Khoroshkov, *Feasibility of Using Laser Ion Accelerators in Proton Therapy*, Plasma Phys. Rep. **28**, 453 (2002); S. V. Bulanov, J. J. Wilkens, T. Zh. Esirkepov, G. Korn, G. Kraft, S. D. Kraft, M. Molls, and V. S. Khoroshkov, *Laser Ion Acceleration for Hadron Therapy*, Phys. Usp. **57**, 1149 (2014).

[9] R. A. Snavely, M. H. Key, S. P. Hatchett, T. E. Cowan, M. Roth, T. W. Phillips, M. A. Stoyer, E. A. Henry, T. C. Sangster, M. S. Singh, S. C. Wilks, A. MacKinnon, A. Offenberger, D. M. Pennington, K. Yasuike, A. B. Langdon, B. F. Lasinski, J. Johnson, M. D. Perry, and E. M. Campbell, *Intense High-Energy Proton Beams from Petawatt-Laser Irradiation of Solids*, Phys. Rev. Lett. **85**, 2945 (2000); S. A. Gaillard, T. Kluge, K. A. Flippo, M. Bussmann, B. Gall, T. Lockard, M. Geissel, D. T. Offermann, M. Schollmeier, Y. Sentoku, and T. E. Cowan, *Increased Laser-Accelerated Proton Energies via Direct Laser-Light-Pressure Acceleration of Electrons in Microcone Targets*, Phys. Plasmas **18**, 056710 (2011); F. Wagner *et al.*, *Maximum Proton Energy above 85 MeV from the Relativistic Interaction of Laser Pulses with Micrometer Thick CH2 Targets*, Phys. Rev. Lett. **116**, 205002 (2016).

[10] B. M. Hegelich, B. J. Albright, J. Cobble, K. Flippo, S. Letzring, M. Paffett, H. Ruhl, J. Schreiber, R. K. Schulze, and J. C. Fernandez, *Laser Acceleration of Quasi-monoenergetic MeV Ion Beams*, Nature (London) **439**, 441 (2006); A. Henig, S. Steinke, M. Schnurer, T. Sokollik, R. Horlein, D. Kiefer, D. Jung, J. Schreiber, B. M. Hegelich, X. Q. Yan, J. Meyer-ter-Vehn, T. Tajima, P. V. Nickles, W. Sandner, and D. Habs, *Radiation-Pressure Acceleration of Ion Beams Driven by Circularly Polarized Laser Pulses*, Phys. Rev. Lett. **103**, 245003 (2009).

[11] S. Bedacht, G. Schaumann, A. Blazevic, M. Roth, D. H. H. Hoffmann *et al.*, GSI Scientific Report No. PNI-PP-25, 2012, p. 458.

[12] A. Propp, SLAC Technical Note No. SLAC-TN-15-078, 2015.

[13] S. Garcia, D. Chatain, and J. P. Perin, *Continuous Production of a Thin Ribbon of Solid Hydrogen*,Laser Part. Beams **32**, 569 (2014).

[14] K. Jungwirth *et al.*, *The Prague Asterix Laser System*, Phys. Plasmas **8**, 2495 (2001).

[15] M. De Marco *et al.*, *Measurement of Electromagnetic Pulses Generated during Interactions of High Power Lasers with Solid Targets*, J. Instrum. **11**, C06004 (2016).

[16] E. Woryna, P. Parys, J. Wołowski, and W. Mróz, *Corpuscolar Diagnostics and Processing Methods Applied in Investigations of Laser-Produced Plasma as a Source of Highly Ionized Ions*, Laser Part. Beams **14**, 293 (1996).

[17] D. Margarone *et al. Full Characterization of Laser-Accelerated Ion Beams Using Faraday Cup, Silicon Carbide, and Single-Crystal Diamond Detectors*, J. Appl. Phys. **109**, 103302 (2011); G. Bertuccio , D. Puglisi, L. Torrisi, and C. Lanzieri, Appl. Surf. Sci. **272**, 128 (2013).

[18] J. Prokupek *et al.*, *Development and First Experimental Tests of Faraday Cup Array*, Rev. Sci. Instrum. **85**, 013302 (2014).

[19] T. Pisarczyk *et al. Pre-Plasma Effect on Energy Transfer from Laser Beam to Shock Wave Generated in Solid Target*, Phys. Plasmas **21**, 012708 (2014); *Space-Time Resolved Measurements of Spontaneous Magnetic Fields in Laser-Produced Plasma*, Phys. Plasmas **22**, 102706 (2015).

[20] D. Klir, J. Kravarik, P. Kubes, K. Rezac, E. Litseva, K. Tomaszewski, L. Karpinski, M. Paduch, and M. Scholz, *Fusion Neutron Detector for Time-of-Flight Measurements in Z-Pinch and Plasma Focus Experiments*, Rev. Sci. Instrum. **82**, 033505 (2011).

[21] D. Klir *et al.*, *Efficient Neutron Production from Sub-Nanosecond Laser Pulse Accelerating Deuterons on Target Front Side*, Phys. Plasmas **22**, 093117 (2015).

[22] A. Kasperczuk and T. Pisarczyk, Optica Applicata **XXXI**, 571 (2001).

[23] J. Krasa, P. Parys, L. Velardi, A. Velyhan, L. Ryc, D. Della Side, and V. Nassisi, *Time-of-Flight Spectra for Mapping of Charge Density of Ions Produced by Lasers*, Laser Part. Beams **32**, 15 (2014).

[24] S. J. Gitometer, R. D. Jones, F. Begay, A. W. Ehler, J. F. Kephart, and R. Kristal, *Fast Ions and Hot Electrons in the Laser-Plasma Interaction*, Phys. Fluids **29**, 2679 (1986).

[25] D. Margarone *et al.*, *New Methods for High Current Fast Ion Beam Production by Laser-Driven Acceleration*, Rev. Sci. Instrum. **83**, 02B307 (2012); *Advanced Scheme for High-Yield Laser Driven Nuclear Reactions*, Plasma Phys. Controlled Fusion **57**, 014030 (2015).

[26] R. Liska *et al.*, in *ALE Method for Simulations of Laser-Produced Plasmas, Finite Volumes for Complex Applications VI: Problems and Perspectives*, edited by J. Fořt *et al.* (Springer, Berlin, 2011), Vol. 4, pp. 857–873.

[27] E. J. Caramana, D. E. Burton, M. J. Shashkov, and P. P. Whalen, *The Construction of Compatible Hydrodynamics Algorithms Utilizing Conservation of Total Energy*, J. Comput. Phys. **146**, 227 (1998).

[28] R. Loubere and M. Shashkov, *A Subcell Remapping Method on Staggered Polygonal Grids for Arbitrary-Lagrangian–Eulerian Methods*, J. Comput. Phys. **209**, 105 (2005).

[29] M. Hanfland, R. J. Hemley, and H. K. Mao, *Novel Infrared Vibron Absorption in Solid Hydrogen at Megabar Pressures*, Phys. Rev. Lett. **70**, 3760 (1993).

[30] D. Haberberger, S. Tochitsky, F. Fiuza, C. Gong, R. A. Fonseca, L. O. Silva, W. B. Mori, and C. Joshi, *Collisionless Shocks in Laser-Produced Plasma Generate Monoenergetic High-Energy Proton Beams*, Nat. Phys. **8**, 95 (2012).

[31] C. M. Brenner *et al.*, *High Energy Conversion Efficiency in Laser-Proton Acceleration by Controlling Laser-Energy Deposition onto Thin Foil Targets*, Appl. Phys. Lett. **104**, 081123 (2014).

[32] M. Roth *et al. Fast Ignition by Intense Laser-Accelerated Proton Beams*, Phys. Rev. Lett. **86**, 436 (2001).

[33] S. Atzeni, M. Temporal, and J. J. Honrubia, *A First Analysis of Fast Ignition of Precompressed ICF Fuel by Laser-Accelerated Protons*, Nucl. Fusion **42**, L1 (2002); M. Temporal, J. J. Honrubia, and S. Atzeni, *Numerical Study of Fast Ignition of Ablatively Imploded Deuterium-Tritium Fusion Capsules by Ultra-Intense Proton Beams*, Phys. Plasmas **9**, 3098 (2002).

[34] T. D. Arber *et al.*, *Contemporary Particle-in-Cell Approach to Laser-Plasma Modeling*, Plasma Phys. Controlled Fusion **57**, 113001 (2015).

[35] B. Rus *et al.*, in Diode-Pumped High Energy and High Power Lasers; ELI: Ultrarelativistic Laser-Matter Interactions and Petawatt Photonics; and HiPER: the European Pathway to Laser Energy, SPIE Proceedings Vol. **8080** (SPIE-International Society for Optical Engineering, Bellingham, WA, 2011), p. 808010.